Initiation Of Detonation By Shock Focusing

Pawel M. Buraczewski

Graduate Aeronautical Laboratories
California Institute of Technology
Pasadena, CA 91125

GALCIT Report FM 2004.004

October 20, 2004, Revised December 27, 2021

Sponsored by the Office of Naval Research (ONR Grant Number N00014-03-1-0931) and
the Polish-US Fulbright Commission

In Memoriam

Pawel Maria Buraczewski, September 9, 1970 – October 21, 2005

Pawel carried out this research and wrote this report[1] as a Fulbright scholar at Caltech in 2003-2004, working in the Explosion Dynamics Laboratory on his doctoral research project. Pawel was a cheerful and enthusiastic member of the lab group and made many friends during his brief time at Caltech. He is missed. Pawel was a PhD student of Andrzej Teodorczyk at the Warsaw Institute of Technology and had planned to defend this study as his PhD thesis upon returning to Poland. Tragically, he became ill upon returning home and was unable to complete his thesis defense. In Pawel's honor, the Polish Institute of Combustion established in 2006 an annual prize and awards for the best doctoral theses in the topic of combustion.

[1] Edited by Joe Shepherd and publicly released in 2021.

Abstract

Experiments and analysis were carried out on the initiation of detonation in selected gas mixtures by shock wave focusing. Detonation initiation thresholds and detailed wave mechanics of the initiation process were investigated for a range of conditions. The GALCIT 6-in shock tube was used to create shock waves in a combustible gas with Mach numbers between 1.25 and 3 in special secondary test section that was designed and fabricated as part of this study. The test section (75 mm internal diameter) was attached to the end of the driven section of the shock tube and separated by a thin diaphragm. Piezo-electric pressure gages and ion probes that were recorded with a high-speed data acquisition system to determine flame, shock wave, and detonation trajectories outside of the reflectors. The test section was filled with stoichiometric ethylene-oxygen, hydrogen-oxygen or propane-oxygen with nitrogen dilution between 0 and 60%. At the end of the test section, an axisymmetric reflector was used to create the reflected shock wave and focusing conditions. A flat reflector was used for reference and three paraboloidal reflectors of depth-to-height ratio of 0.5, 1.25, and 2.0 were examined. The driver and test section pressures and gases were selected to vary the shock Mach number while keeping the values of the computed post-shock pressure in the test gas between 70-100 kPa. A range of prompt or delayed combustion events were observed depending on the depth and shape of the reflector, the strength of the incident wave, and the composition of the combustible gas. The possibilities include: no reaction, flame, transition to detonation outside the reflector, transition to detonation inside the reflector. In addition to the experimental results, non-reactive (perfect gas simulating air) Euler simulations were carried out using the Amrita software package to examine the focusing region for the axisymmetric configurations corresponding to the reflectors that were investigated in the experiments. Three types of focusing configurations were identified depending on the depth of the reflector and incident shock Mach number (1.25 to 3.0).

Contents

List of Figures

List of Tables

1 Introduction

The goals of the current study were to obtain fundamental data on transition to detonation by reflection of shocks in axisymmetric reflectors. Numerical simulations of non-reactive shock waves were carried out to obtain the regimes of focusing possible for shock Mach numbers between 1.25 and 3; these are values that we could obtain experimentally. A series of experiments were carried in special modification of the GALCIT 6-in shock tube using three fuels, hydrogen, ethylene and propane in mixtures with oxygen diluted by nitrogen. At the end of the test section, an axisymmetric reflector was used to create the reflected shock wave and focusing conditions. A flat reflector was used for reference and three paraboloidal reflectors of depth-to-height ratio of 0.5, 1.25, and 2.0 were examined. Pressure and ion probe measurements were used to determine flame, shock wave, and detonation trajectories outside of the reflectors. The driver and test section pressures and gases were selected to vary the shock Mach number while keeping the values of the computed post-shock pressure in the test gas between 70-100 kPa.

Brief discussions of the mechanisms of detonation initiation and shock reflection are given in this introduction; this material benefited from and was based on the review of Wintenberger et al. (2001). The following sections of the report summarizes the results of non-reactive numerical simulations of focusing, describes the design of the experimental facility and the results of the tests. A set of appendices provides the details of the facility construction and shock tube operation, tables of conditions for simulations and experiments, plots of pressure signals and space-time diagrams of the shock and ion probe signal trajectories.

1.1 Indirect and Direct Detonation Initiation

To initiate a self-sustained detonation wave, a critical condition must be achieved in a sufficiently large volume of a combustible mixture. A successful initiation event results in a coupling between the leading shock wave and the chemical reaction zone. A failed initiation event is characterized by a decoupling of the shock and the reaction zone, which lags behind the shock front.

In general, two different ways to achieve an initiation of detonation exist: a deflagration to detonation transition (DDT) and direct initiation of detonation. The primary difference between these two processes lies in the amount of energy initially deposited in the combustible mixture. A low energy deposition creates a flame, propagating with a typical velocity of several m/s. Since deflagration products are characterized by a volumetric expansion, they can behave as a gas piston sending compression waves ahead of the flame. Every compression wave heats the mixture it passes through and, thus, increases the sound velocity of the mixture. Subsequent compression waves travel with the higher velocity. As a result of this process, a series of compression waves eventually coalesce into a shock wave. If this shock wave is sufficiently strong, the rise in temperature behind it can trigger chemical reactions. This way, a detonation wave can be initiated ahead of the flame front.

More often, a more complex DDT process occurs in which the flow created by the flame initially accelerates the subsequent propagation of the flame. This flame acceleration process is usually characterized by the generation of turbulent flow. Turbulence, in addition to the flame interaction with reflected shock or compression waves, wrinkles, stretches and distorts

the flame front. Turbulent mixing of products and reactants and the interaction of shock waves produced by the high-speed flame results in the formation of explosion centers or hot spots. Interaction of shock wave with these explosion centers results in the generation of shock waves and eventually a detonation wave. More detailed information on the flame laceration and the DDT process can be found in chapter 2 of Breitung et al. (2000).

Direct initiation of detonation arises when a sufficiently high amount of energy is deposited in an unconfined volume of combustible mixture. A decaying spherical blast wave is created. In the case of successful initiation, this blast wave decelerates to a Chapman-Jouguet velocity and becomes a self-sustained detonation wave. Otherwise, the blast wave decelerates below this velocity and the reaction zone decouples from the leading shock front.

The mechanism of the initiation of detonation by means of shock wave focusing can be classified as a type of indirect initiation. An initially created shock wave travels through a combustible medium. After reaching the end of a detonation tube the shock wave enters a reflector, which is a cavity of a specified shape. In case of a two-dimensional reflector, the shock wave focuses after reflection from the walls on a line perpendicular to the detonation tube axis. In case of a three-dimensional reflector, the focal region is limited to the small region around a point. Depending on the specific shape and depth of the reflector and the Mach number of the incident shock wave, the shock wave can focus away from (free-field focusing) or at the surface (implosion) of the reflector. A number of researchers have examined various aspects of detonation initiation by shock reflection, including Chan et al. (1990), Bartenev et al. (2000), Gelfand et al. (2000), Khomik et al. (2007). These studies primarily used two-dimensional (rectangular crosssection) reflectors and visualization of the events inside the reflector using shadow or schlieren methods. The present study adds complementary information on the axisymmetric geometry and details of the wave propagation outside of the reflector.

1.2 Mechanism of Shock Focusing

When the incident shock wave penetrates the cavity of the reflector, its central part propagates towards the reflector, while the parts which interacted with the reflector corners create diffracted shock waves. The features are shown in Fig. 1.

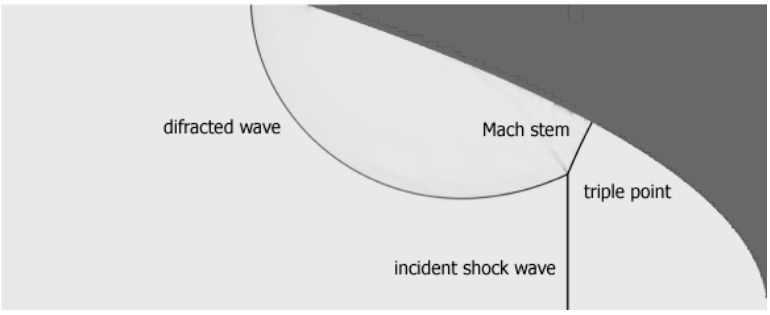

Figure 1: Features of focusing. Results from an Amrita simulation as described in Section 2.

Before the reflection of the central part of the incident shock wave is completed, a third shock front and triple points behind the diffracted waves appear and travel along the reflector

edges. This shock front is a Mach stem and is created, in most cases, independently of the incident shock wave Mach number and depth of the reflector (the Mach stem can be eliminated by use of the logarithmic spiral reflectors; in this case the shock focusing is limited to the implosion only (Milton, 1989)). The triple points move towards the reflector axis as the diffracted shock expands. The triple points merging on the axis creates a region of high pressure and temperature. This represents the shock focusing process. The point where the maximum pressure is obtained is referred to as the gasdynamic focus. This free-field focusing process was first investigated in detail by Sturtevant and Kulkarny (1976) for a variety of reflector shapes and subsequently by Izumi et al. (1994) for parabolic reflectors.

According to Izumi et al., there are three types of shock focusing for a planar parabolic reflector. Type A focusing (Fig. 3) is exhibits a distinct shock perpendicular to the axis in the central portion of the reflected shock wave. This shock increases in width as it travels away from the focus. The focal region is unbounded or open - this kind of reflection is referred to as Mach reflection. Type A reflection occurs for strong incident shock Mach numbers and shallow reflectors. Type C (Fig. 11) reflection occurs when the incident shock Mach number is weak and the reflectors are deep. The pattern of reflection has two traits: the diffracted shock waves from the corners of the reflector intersect twice before focusing and a small conical region surrounded by the reflected shock wave from the center and diffracted shock waves from the sides is formed. This region is subsequently compressed during focusing when the triple points merge. Type B reflection (Fig. 4) is transitional between two previously described ones. It is characterized by diffracted shock waves intersecting once only after focusing. Type B focusing occurs for the "intermediate" shock Mach number values and reflector depths.

The studies reported in this paper include the results of numerical simulations for paraboloidal reflectors for the incident shock Mach numbers up to 3 and reflector-depth-to-tube-radius ratios up to 2. Apart from type A, B and C focusing processes, the simulation results indicate the presence of implosion-like events for deeper reflectors due to the shift of the gasdynamic focus. The implosion process is characteristic of the axisymmetric case. Similar simulations with parabolic planar reflectors performed by Wintenberger et al. (2001) over the same range of the incident shock Mach numbers and reflectors depth do not exhibit the implosion process.

The phenomenon of shock focusing leads to the high pressure and temperature conditions at the gasdynamic focal region. If the Mach number of the incident shock wave is sufficiently high, the energy deposited during the focusing process can be large enough to trigger a detonation wave emerging from the focal region. If not, a complex pattern of reflected shock waves is created inside or outside the cavity of the reflector. Consistently, a number of "hot spots", localized regions of high temperature appear and give rise to centers of explosive ignition events. The reactive blast waves generated at the explosion centers can merge into a detonation wave inside or outside the reflector cavity.

2 Numerical Simulations

Reflection and shock focusing were investigated with the computational fluid dynamic simulations. The two-dimensional, axisymmetric Euler equations were solved with use of Amrita (Quirk, 1998) for a normal shock wave traveling in the constant diameter tube and reaching the cavity of the paraboloidal reflector. The ideal gas model with a constant specific heat ratio ($\gamma = 1.4$) was used for the equation of state. The simulations used adaptive mesh refinement and shock-capturing algorithms to obtain reasonable fidelity of the focusing events. Efforts were made to resolve the flow field away from singular regions in the solution. However, close to singular foci, the predicted peak values may not be reliable as these will depend on the resolution as well as high-temperature phenomena that are not simulated by the ideal gas model. For this reason, the simulations are primarily used to predict the qualitative features of the wave patterns that categorize the type of focusing events.

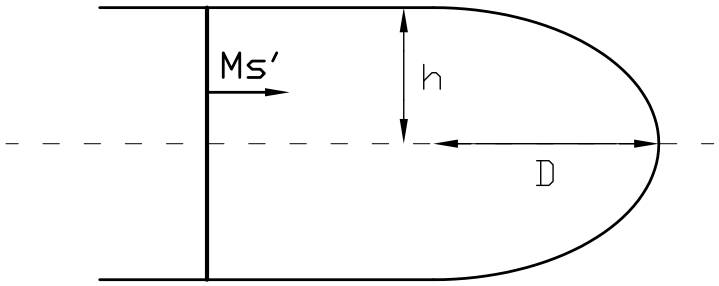

Figure 2: M_s' represents the incident shock wave.

The initial conditions were uniform pre-shock and post-shock fluid states and incident shock Mach numbers M_s ranging from 1.25 to 3. The depth of the reflectors is described as the depth-to-height ratio, D/h (Fig. 2). The depth-to-height ratio ranged from 0.5 to 2.25. Representative results of simulations covering this range of parameters are shown as simulated schlieren images in Figs. 3- 11. Considering the symmetry of the system the simulation results are shown as a function of radial *vs* axial distance, covering one-half of the physical domain.

The results of the simulations can be divided into two categories. The first category occurs when the values of the reflector's depth-to-height ratio are less then 1. In this category, the focusing of the shock waves (that is the merging of the triple points) takes place after the central part of the incident shock wave is reflected from the reflector. The regular patterns of type A (Fig. 3) was observed for every Mach number examined. The regular type B focusing (Fig. 4) occurs for low (up to 1.5) Mach numbers only. Regular type C focusing was not observed at all.

The second category occurs for values of the reflectors depth-to-height ratio larger then 1.25. In this category, the focusing of the shock waves occurs before the reflection of the central part of the incident shock wave is completed. A closed volume of the undisturbed gas is created in the vicinity of the reflector apex, surrounded by the Mach stems. Subsequently, the Mach stems squeeze this volume towards the apex of the reflector. The effect of squeezing

resembles the implosion of the shock waves to the reflector apex point. It is possible to distinguish between types B and C of focusing (Figs. 10, 11) for the examined range of the incident shock Mach number. The results suggest the existence of type A focusing for Mach numbers higher then 3. The domain of the type B focusing starts for a Mach number value of 2 and depth-to-height ratio larger then 1.25, and gradually widens with increasing parameters. Type C focusing domain occupies the region above type B domain.

The boundary between the two categories of focusing depends only on the depth-to-height ratio of the reflector. The transition zone between the two categories of focusing is marked by the shock wave implosion phenomena. For the depth-to-height ratio values of 1 to 1.25 the incident shock wave focuses to a point at the reflector apex or to a short line as a result of the Mach stem convergence. The focusing line is collinear with the reflector axis and emerges from the point where triple points impinge (gasdynamic focus) to the reflector apex. Again, the focusing patterns of type A, B and C are clearly visible (Figs. 5-9).

The numerical simulations show that the gasdynamic focus location significantly shifts with the increase of the reflector's depth-to-height ratio. For a given Mach number, the focal point moves towards the reflector apex until the depth-to-height ratio attains the value of 1-1.25, which marks the transition point from the first to the second category of focusing. Simultaneously, the free field type of focusing is replaced by the creation of implosion at the apex of the reflector. The gasdynamic focus location is then shifted away again from the reflector's apex with the further increase of the depth-to-height ratio.

According to the numerical simulations, the existence of two categories of the shock wave focusing inside the cavity of the paraboloidal reflectors is the characteristic feature only of the axisymmetric case and was not observed by Wintenberger et al. (2001) who used the same algorithm and initial conditions to simulate the shock focusing inside planar (two-dimensional Cartesian geometry) parabolic reflectors. His study only found the first category of focusing in the planar geometry. Although the three types A, B and C of focusing were clearly distinguished in both planar and axisymmetric geometries, the type B focusing domain is quite different for the axisymmetric than for planar case. Compared to the planar case, type B focusing domain for axisymmetric case extends to higher values of the reflector's depth-to-height ratio for higher Mach numbers while for lower Mach numbers the domain occurs for smaller values (Figs. 12 and 13).

The results of the simulations are summarized in the reflection classification diagrams (Figs. 12 and 13). Every letter represents the type of reflection for a given depth-to-height ratio value and Mach number of the incident shock wave. The numerical values of M_s and D/h for each type are given in Appendix B for the axisymmetric cases and in Wintenberger et al. (2001) for the planar cases.

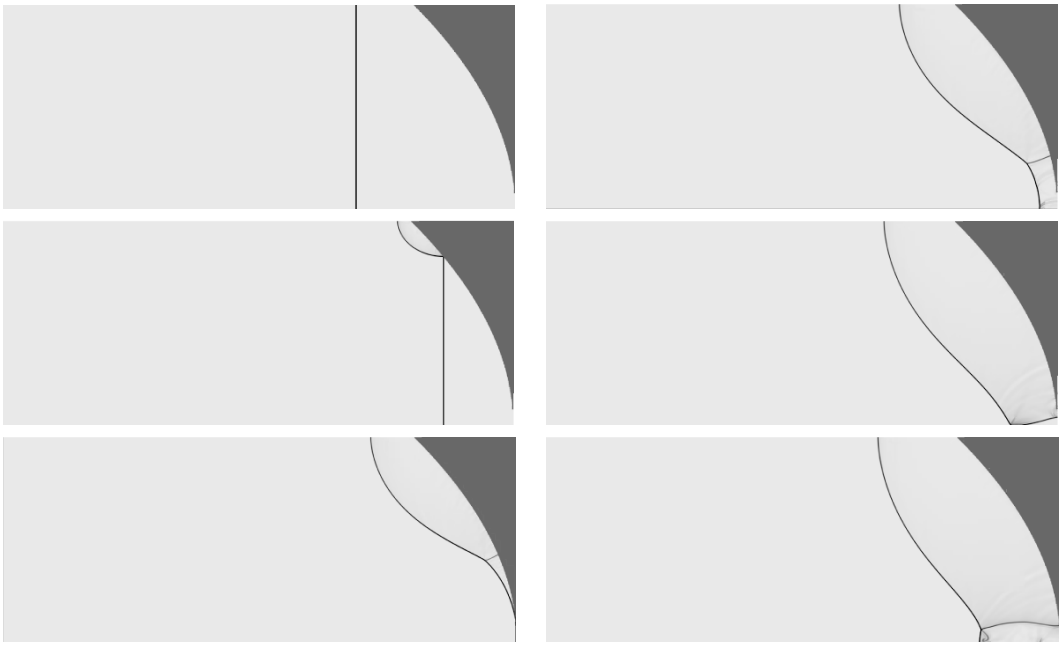

Figure 3: Numerical simulation of regular type A focusing. Gasdynamic focus is apart from the apex. $M_s = 1.5$, $D/h = 0.5$

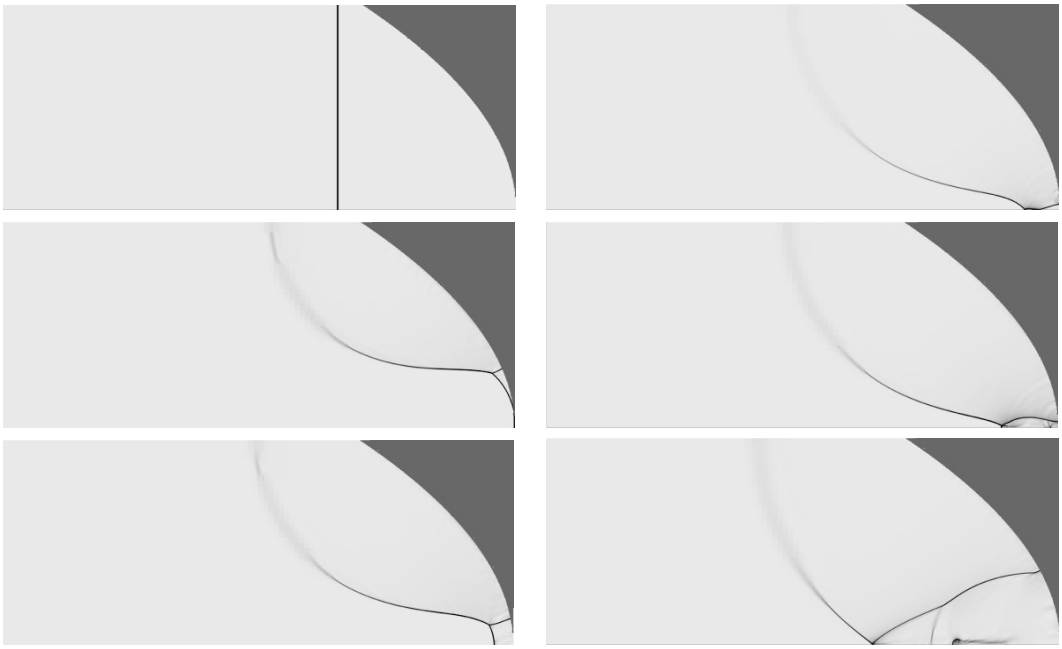

Figure 4: Numerical simulation of regular type B focusing. Gasdynamic focus is apart from the apex. $M_s = 1.25$, $D/h = 0.75$

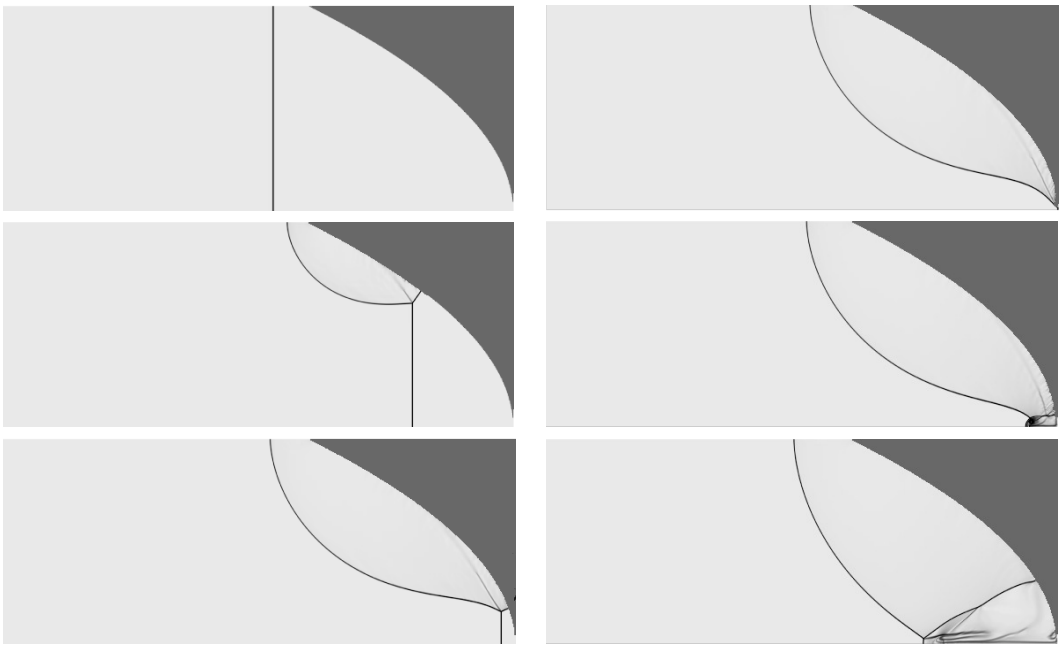

Figure 5: Numerical simulation of transitional type A focusing at apex. $M_s = 1.875$, $D/h = 1.0$

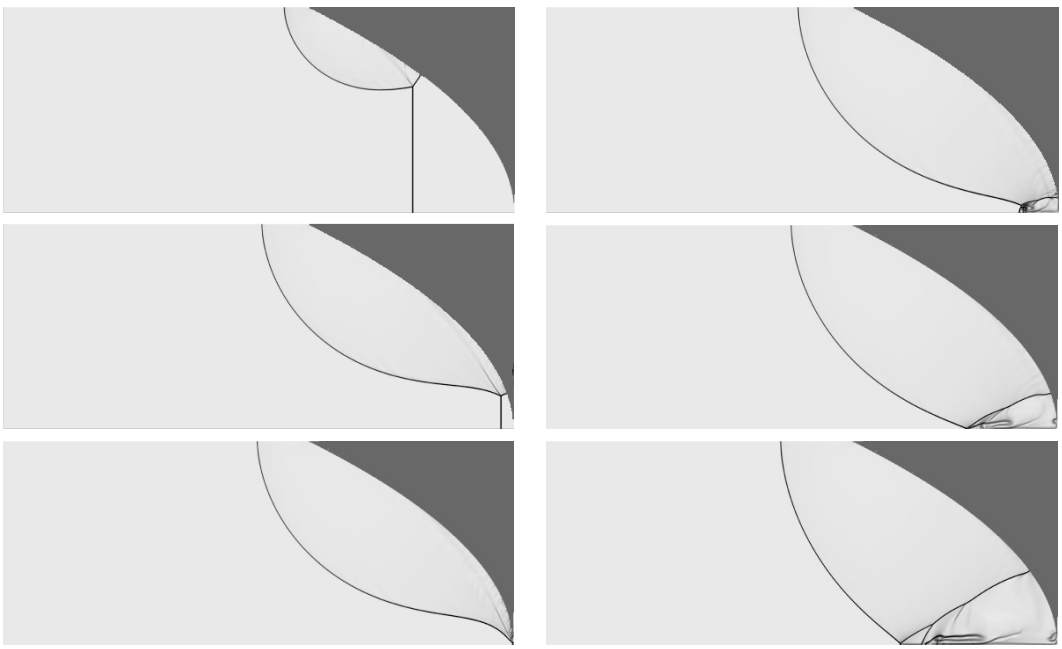

Figure 6: Numerical simulation of transitional type B focusing at apex. $M_s = 1.75$, $D/h = 1.0$

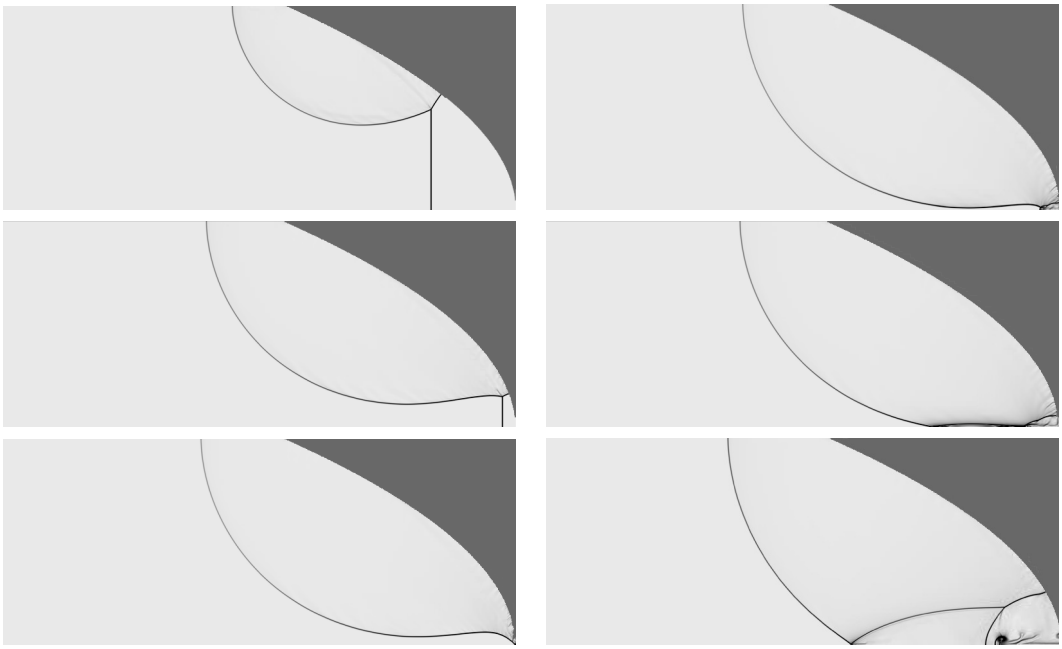

Figure 7: Numerical simulation of transitional type C focusing at apex. $M_s = 1.5$, $D/h = 1.125$

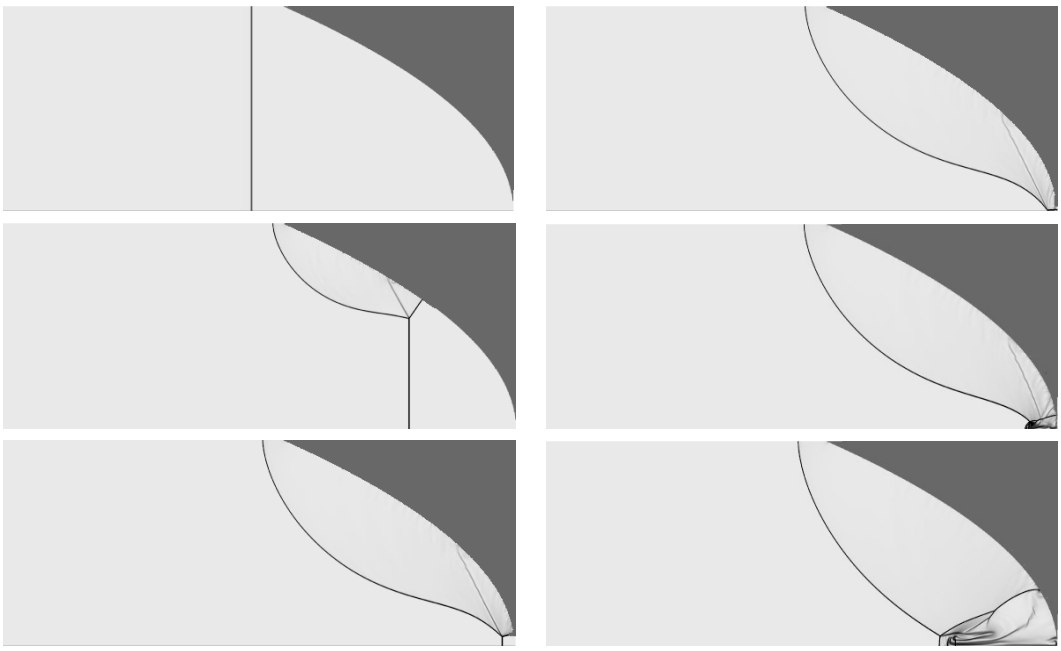

Figure 8: Numerical simulation of transitional type A focusing to a line. $M_s = 2.5$, $D/h = 1.125$

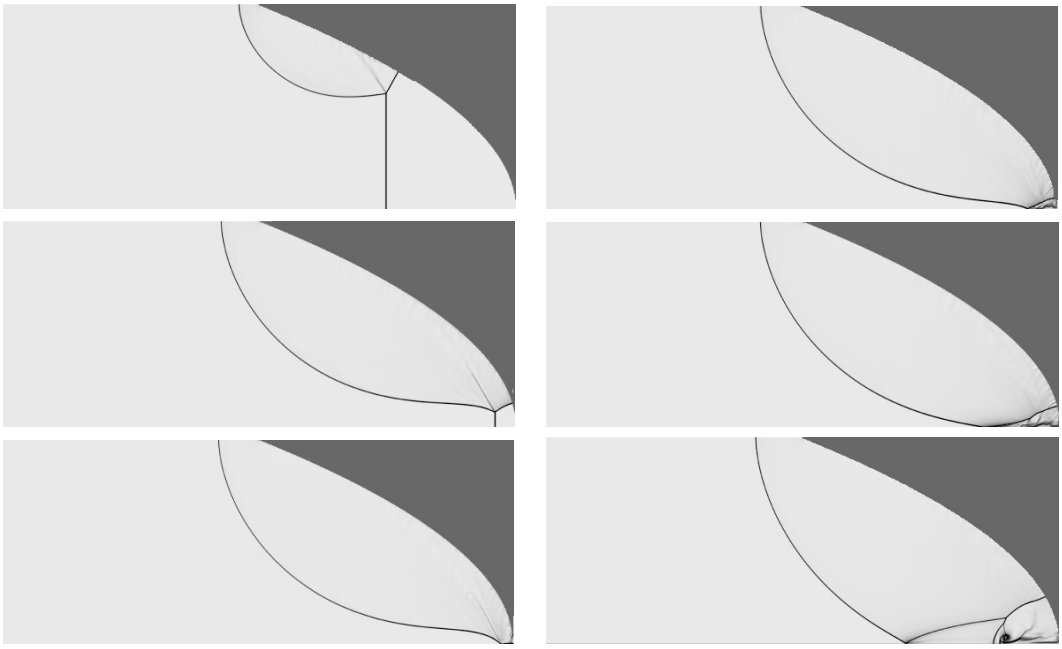

Figure 9: Numerical simulation of transitional type B focusing to a line. $M_s = 2.0$, $D/h = 1.25$

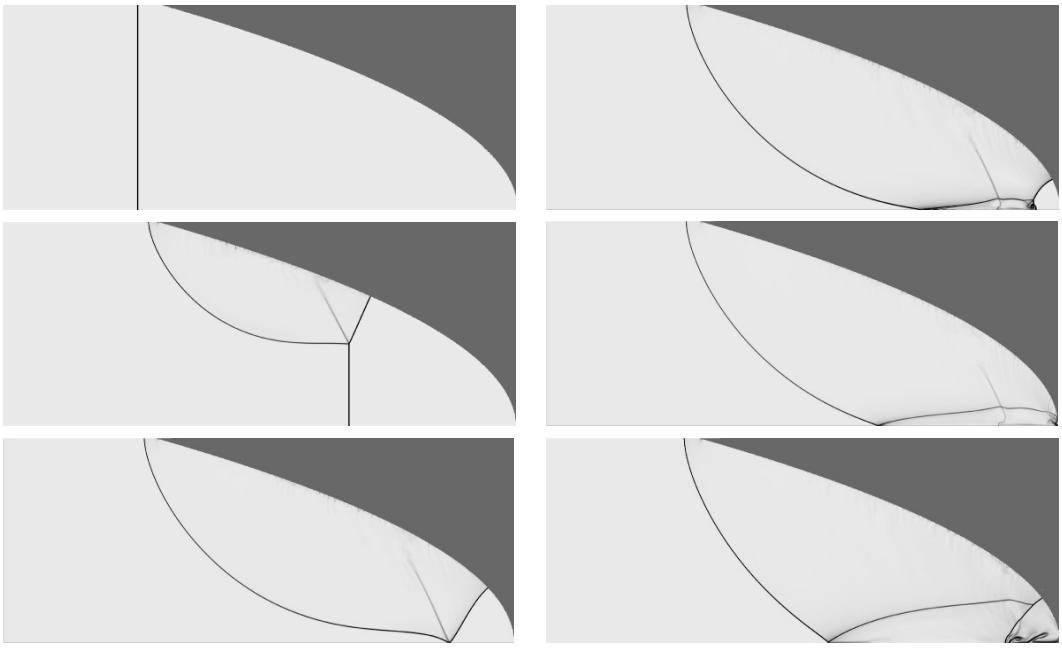

Figure 10: Numerical simulation of type B implosion. Gasdynamic focus is apart from the apex. $M_s = 2.75$, $D/h = 1.75$

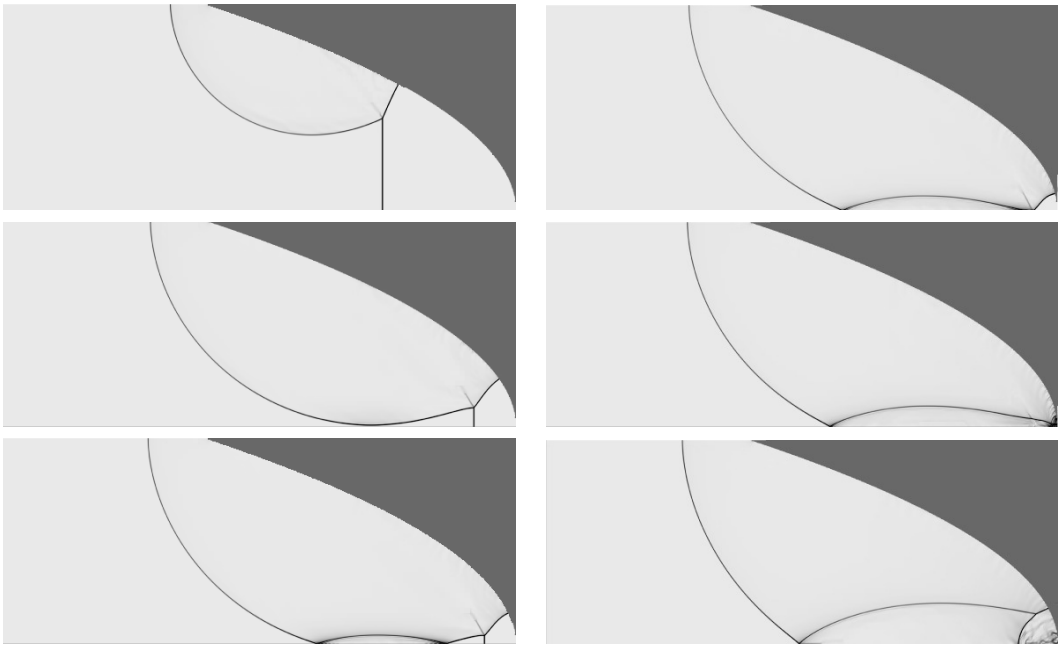

Figure 11: Numerical simulation of type C implosion. Gasdynamic focus is apart from the apex. $M_s = 1.75$, $D/h = 1.5$

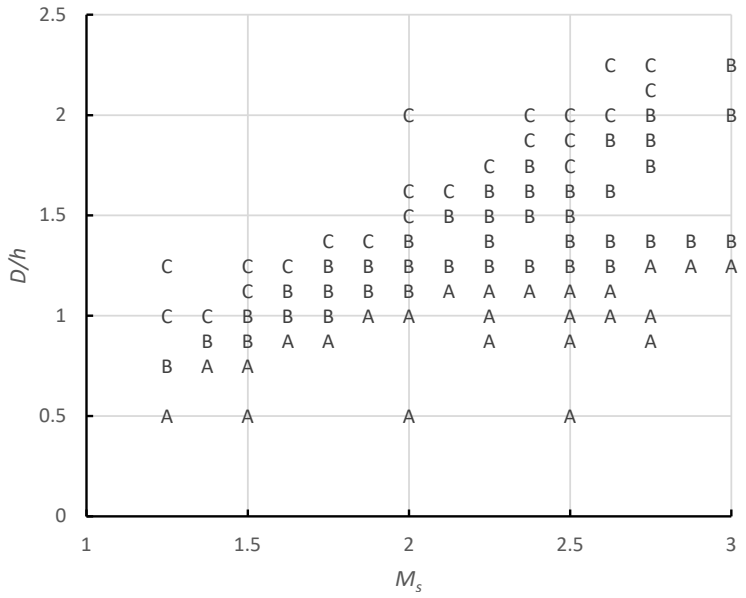

Figure 12: Reflection type for axisymmetric paraboloidal reflectors: effect of reflector depth-to height ratio (D/h) and incident shock wave Mach number M_s on the type of focusing.

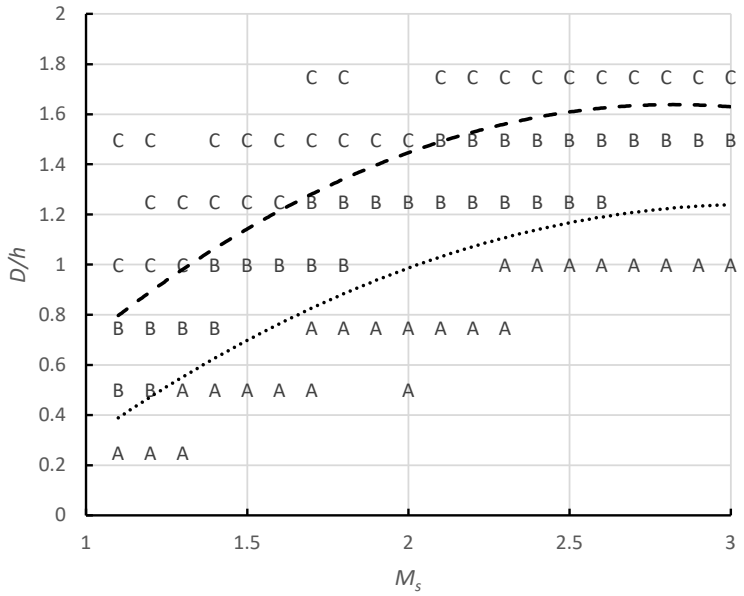

Figure 13: Reflection types for planar parabolic reflectors: effect of reflector depth-to height ratio (D/h) and incident shock wave Mach number M_s on the type of focusing (Wintenberger et al., 2001).

3 Experimental

3.1 Experimental Facility

The experimental setup was the GALCIT 6-Inch Shock Tube (Smith et al., 1967) with a "cookie-cutter" and a test section attached to the end of the original driven section. The cookie-cutter was an 80.0 in. (2.03 m) long aluminium tube of 3.0 in. (75 mm) inner diameter which protruded into the end of the shock tube. The use of the cookie-cutter precluded the incident shock wave diffraction at the transition from the shock tube to the test section due to inner diameter difference: 6.0 in. (150 mm) for the shock tube and 3.0 in. (75 mm) for the test section. The sharpened end of the cookie-cutter enabled a smooth cut-out of the central part of the incident shock wave generated in the shock tube. The length of the cookie-cutter was carefully chosen to maximize the test time - the performance calculation is included below (Section 3.4).

The test section tube was attached to the cookie-cutter by means of four latch clamps and to the shock tube by an annular clamp. The cookie-cutter and the test section are shown in Figs. 14 and 15. Fig. 16 illustrates a schematic view of the experimental setup. A detailed description of the test section and operation of the experimental facility is given in the subsequent Sections 3.2 and 3.5.

3.2 Test Section

The test section was a 96.0 in. (2.44 m) long and 3.0 in. (75 mm) inner diameter aluminium tube suspended from a sliding beam by means of two sets of rollers. During the experiment, a 0.5 mil (0.0005 in. or 127 μm) thick Mylar diaphragm separating the test section from the cookie-cutter was attached to the test tube. The test tube was then slid back and fixed in place by use of four latch clamps. The inside of the other end of the test tube was machined for one of four different reflectors to be inserted. The inner diameter of the tube was widened from 3.0 in. (75 mm) to 3.125 in. (79.4 mm) to a depth of 4.66 in. (118 mm) creating a small step inside the tube. The inserted reflector was blocked by the step from the inside and secured from the outside by an end cap fastened to the walls of the test tube by eight 1/4-20 screws (see CAD Overall Assembly Drawing in Section E).

The test section was equipped with thirteen pressure transducer ports and nine ion probe ports - see Fig. 17. Additional pressure transducer ports were drilled in the apex of every paraboloidal reflector and in the center of a flat reflector. The pressure transducer ports numbered from two to six were spaced equidistantly 0.787 in. (2 cm) apart, starting from the port number two located 5.164 in. (13.1 cm) from the end of the tube of the reflector side (or 0.5 in. from the step inside the tube, which corresponds to the rim of the reflector). The pressure transducer ports numbered from six to twelve were placed again equidistantly 1.574 in. (4 cm) apart. Port number thirteen was located approximately in the middle of the tube (44.5 in. 113 cm, from the end attached to the cookie-cutter) and port number fourteen less then 2 in. (5 cm) from that end. The ion probe mounts were drilled on the opposite side of the tube, facing the pressure transducer ports. The mounts were numbered from one to nine, the first mount being located 5.164 in. (13.1 cm) from the end tube of the reflector side, opposite the pressure transducer port number two. The ion probe mounts

from one to five were drilled equidistantly 1.574 in. (4 cm) apart, the mounts from five to nine - equidistantly 3.148 in. (8 cm) apart. Thus, seven ion probe mounts were facing the pressure transducer ports at the corresponding axial locations - for details see Fig. 18 and CAD Overall Assembly Drawing in Section E. The test section was equipped with nine pressure transducers and nine ion probes. The pressure transducers (Piezotronics PCB 113A models) were placed in ports of numbers two, four, six to eight and twelve to fourteen. A single transducer was also mounted in the apex or center of the reflector. The ion probes and electronic circuits were fabricated in-house with a design that is described in Jackson (2005); all ion probe mounting locations were used.

Signals from he pressure transducers and ion probes were recorded on two National Instruments data acquisition cards. The first four-channel data acquisition system (DAQ1) recorded data from pressure transducers placed in ports fourteen to twelve and eight. Triggered by the arrival of the incident shock wave at the outermost fourteenth transducer, the DAQ1 collected the data at 250 kHz sampling rate for 20 ms. The data from remaining five transducers and the transducer mounted at port number eight were recorded on the eight-channel second data acquisition system (DAQ2). The DAQ2, working at the 2 MHz sampling rate for 15 ms, was triggered by the arrival of the shock wave at the transducer at port number seven. Collecting the data from the transducer in port number eight on both DAQs enabled synchronizing the pressure history from all pressure transducers on one plot. The signals from the ion probes were recorded on the remaining two free channels of DAQ2 - one channel was used for ion probes placed at the odd numbered mounts (five ion probes), another one for probes located at the even numbered mounts (four ion probes).

3.3 Reflectors

Reflectors used in the experiments were 3.729 in. (9.47 cm) long aluminium cylinders of 3.122 in. (7.93 cm) diameter. One end of each cylinder was shaped into a paraboloidal depression. A narrow rim around depression was left to fit a step inside the test tube. A port for a pressure transducer was drilled in the apex of every reflector (see CAD Reflector Drawings in Section E). Based on the results of numerical simulations illustrated in Fig. 12 and the upper limit for the Mach number of 2.5 that could be readily generated by using air in the driver and driven sections of the shock tube, three paraboloidal reflectors of different depth-to-height ratio (D/h) were chosen to be tested: the shallowest, $D/h = 0.5$; intermediate, $D/h = 1.25$; and the deepest, $D/h = 2$. The profile of the reflectors is specfied as $z = Ar^2$, where z is the axial distance from the deepest point of the reflector and r is the radial distance from the axis of symmetry. In dimensional terms, the coefficient $A = D/h^2$. For shallowest reflector ($D/h = 0.5$), $A = 0.334$ in^{-1}; for the intermediate reflector ($D/h = 1.25$) $A = 0.834$ in^{-1}, and for the deepest reflector ($D/h = 2$) $A = 1.335$ in^{-1}.

According to the numerical simulation results, the shallowest reflector causes type A focusing, the intermediate reflector generates type B focusing while the deepest reflector favours type C focusing. The reflectors are shown in Figs. 19, 20 and 21.

Figure 14: The test section (right) and the cookie-cutter. A sharpened edge of the cookie-cutter to cut out a central part of an incident shock wave and four latch clamps attached to the detonation tube clamp fixture to secure the test section are displayed. At the other side of the test tube, a set of sensor ports is visible. The distance between the two black suspension mounts on the test tube is approximately 1 meter.

3.4 Performance Calculations for the Cookie-Cutter

A critical aspect of designing the experimental setup was to establish the length of the cookie-cutter for the range of operational conditions. The pattern of the shock waves within the experimental facility is shown in Figs. 22 and 23. A series of reflected and transmitted waves are produced at the contact surfaces, area changes and end of the test section. These have to be accounted for in determining the available test time and conditions in the test section.

Six different stoichiometric combustible mixtures were chosen for the calculations on the performance of the cookie-cutter: H_2-O_2, H_2- air, C_2H_4-O_2, C_2H_4- air, C_3H_8-O_2, and C_3H_8-air. The compositions of the mixtures used in the present tests can be specified in terms of the O_2/N_2 ratio β. For "combustion" air containing only O_2 and N_2, $\beta = 3.76$ and the stoichiometric compositions are given in Table 1.

The specification % N_2 used in this report is the mole fraction of N_2 in the total mixture, % $N_2 = 100\ X_{N_2}$.

The gas filling the shock tube and the cookie-cutter was air in all cases. Only the reflection from a flat end of the detonation test tube was taken into account in constructing the wave diagrams. Thus, the shock focusing phenomena after reflection from the walls of differently-shaped reflectors are not considered in these calculations.

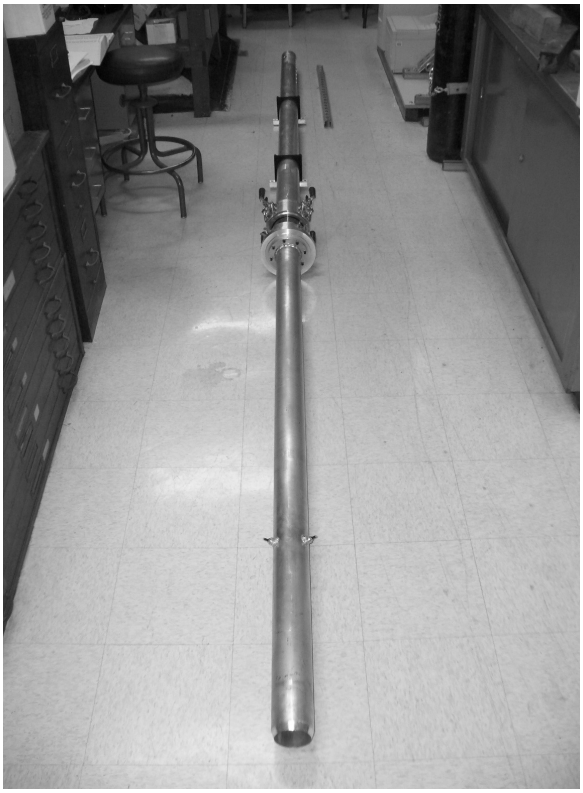

Figure 15: The cookie-cutter and the test section combined together. The total length of the facility is about 5.5 meters and the mass is about 50 kilograms.

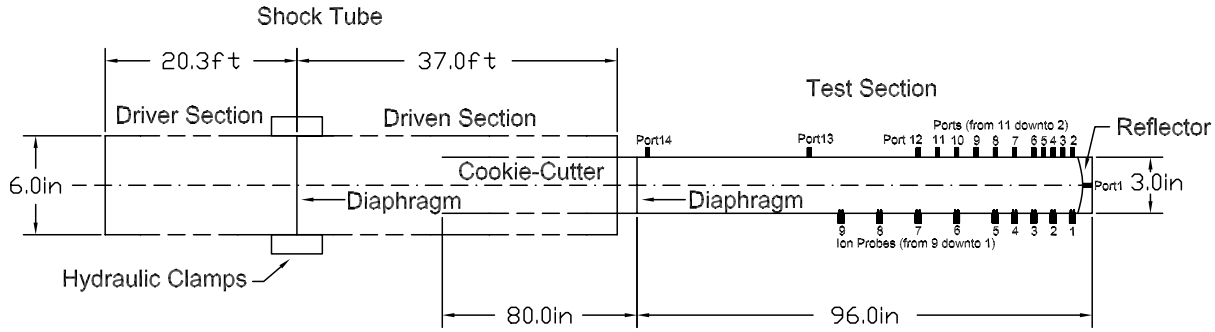

Figure 16: A schematic of the experimental facility. The drawing is not to scale.

After the diaphragm between the driver and driven sections ruptures, a shock wave with Mach number M_s propagates down the shock tube, compressing the gas from state 1 to state 2. Simultaneously, the expansion fan propagates through the air which occupies the driver section, changing it from state 4 to state 3. The boundary between the gas at state 2; shock-wave-processed driven air, and the gas at state 3; expanded air in the driver after the passage of the expansion fan, is considered as an ideal contact surface. Conditions of equal pressures P and flow velocities u of the gases on each side of the contact surface: $P_2 = P_3$ and

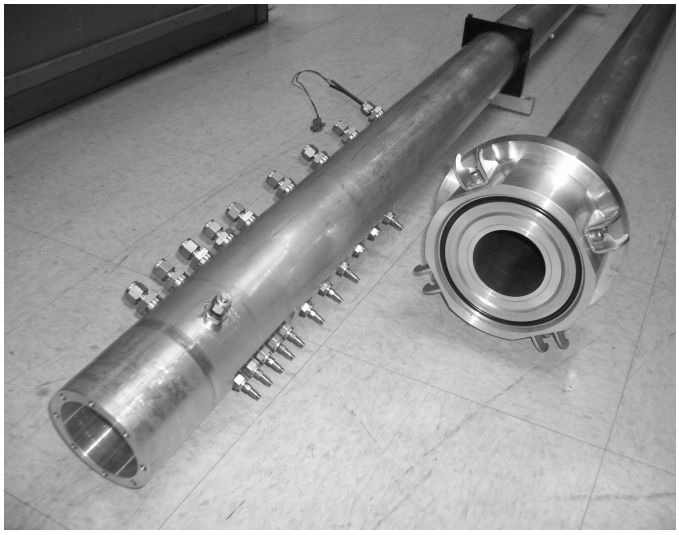

Figure 17: A closeup view of the test tube section equipped with nine pressure transducers and nine ion probes. The single port at the top of the test tube is for the attachment of a combustible mixture fill line. Eight holes in the wall of the test tube serve to attach an end cap to secure the reflector. Four catches on the flange attached to the cookie-cutter are parts of the latch clamps.

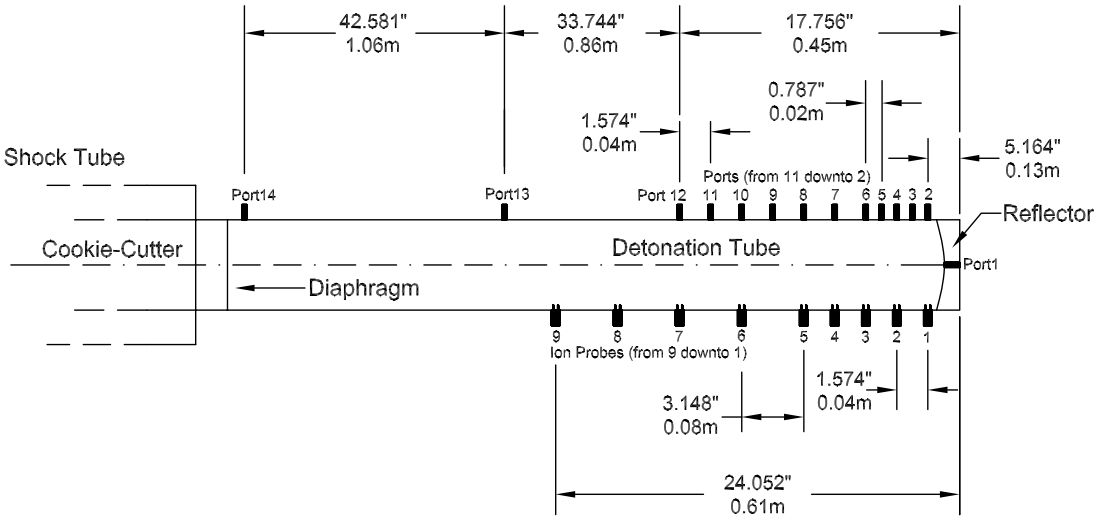

Figure 18: A schematic of the test section - not to scale.

$u_2 = u_3$ are prescribed. For the sake of calculations, the pressure ratios P_2/P_1 were chosen according to the requirements for the range of the shock Mach numbers of the incident shock

Figure 19: A view of the cavities of three paraboloidal reflectors and a flat reflector. Holes at the centers are the pressure transducer port.

Figure 20: The back side of the reflectors. The small central holes are the pressure transducer port. The two outermost holes in every reflector serve to secure them by the end cap attached to the end of the test tube. The order of the reflectors on both photos is the same.

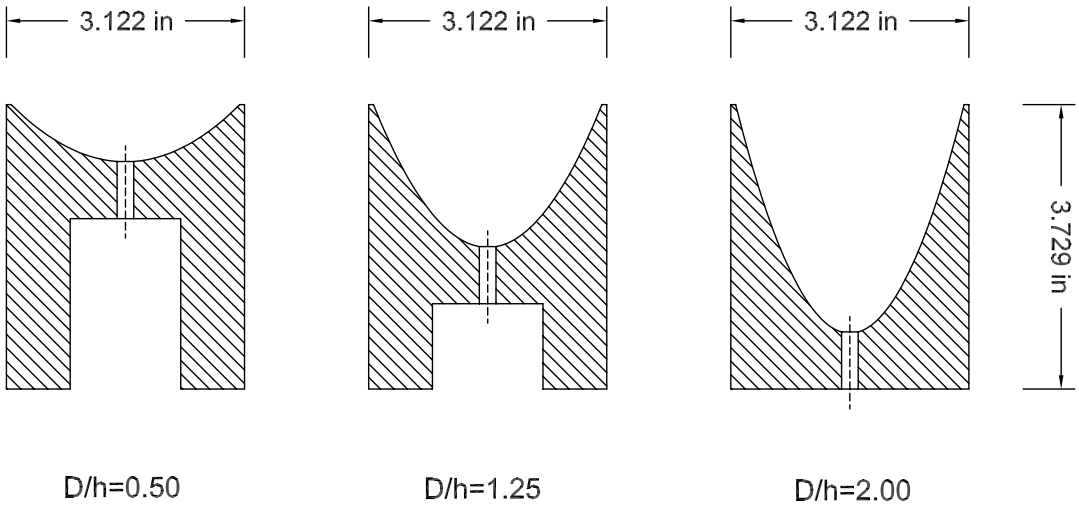

Figure 21: Cross section of the paraboloidal reflectors. The pressure transducer mounts in the apexes of the reflectors are shown.

wave. The pressure ratios P_4/P_1 were found according to the basic shock-tube equation:

$$\frac{P_4}{P_1} = \frac{P_2}{P_1}\left[1 - \frac{(\gamma_4 - 1)\frac{a_1}{a_4}\left(\frac{P_2}{P_1} - 1\right)}{\sqrt{2\gamma_1}\sqrt{2\gamma_1 + (\gamma_1 + 1)\left(\frac{P_2}{P_1} - 1\right)}}\right]^{-\frac{2\gamma_4}{\gamma_4 - 1}}. \qquad (1)$$

Table 1: Test mixture specifications

Mixture	X_{N_2}	% N_2 (air)
$2H_2 + O_2 + \beta N_2$	$\frac{\beta}{3+\beta}$	55.6
C_2H_4+3(O_2+ βN_2)	$\frac{3\beta}{4+3\beta}$	73.8
C_3H_8 + 5(O_2+ βN_2)	$\frac{5\beta}{6+5\beta}$	75.8

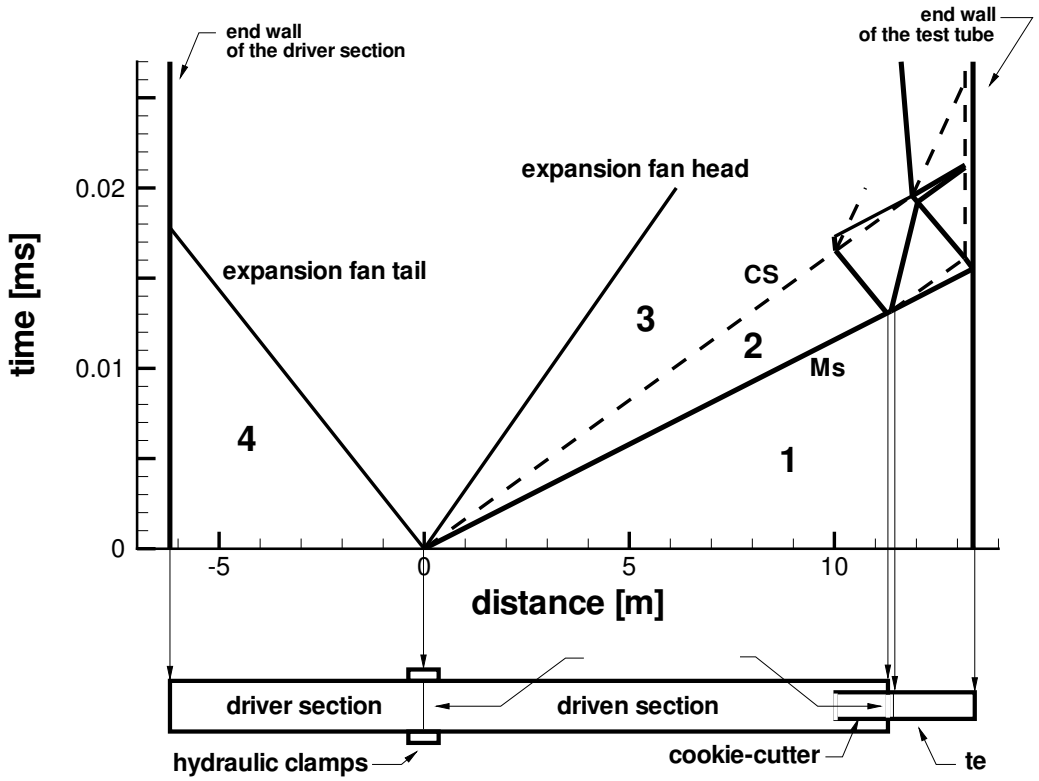

Figure 22: Space-time (x-t) diagram for the experimental facility operation. The test tube is filled with a propane-air mixture and the both driver and driven section along with cookie-cutter are filled with air. The conditions shown corresponds to case number 7 - details are presented in Table 3. The thick line emerging from the diagram represents the shock and expansion waves while dashed lines illustrate contact surfaces CS. M_s stands for an incident shock wave generated in the shock tube.

The values of the pressure ratios and the corresponding velocities of the shock wave for some representative cases are given in Table 2.

A different phenomenon occurs when the central part of the incident shock wave cut out

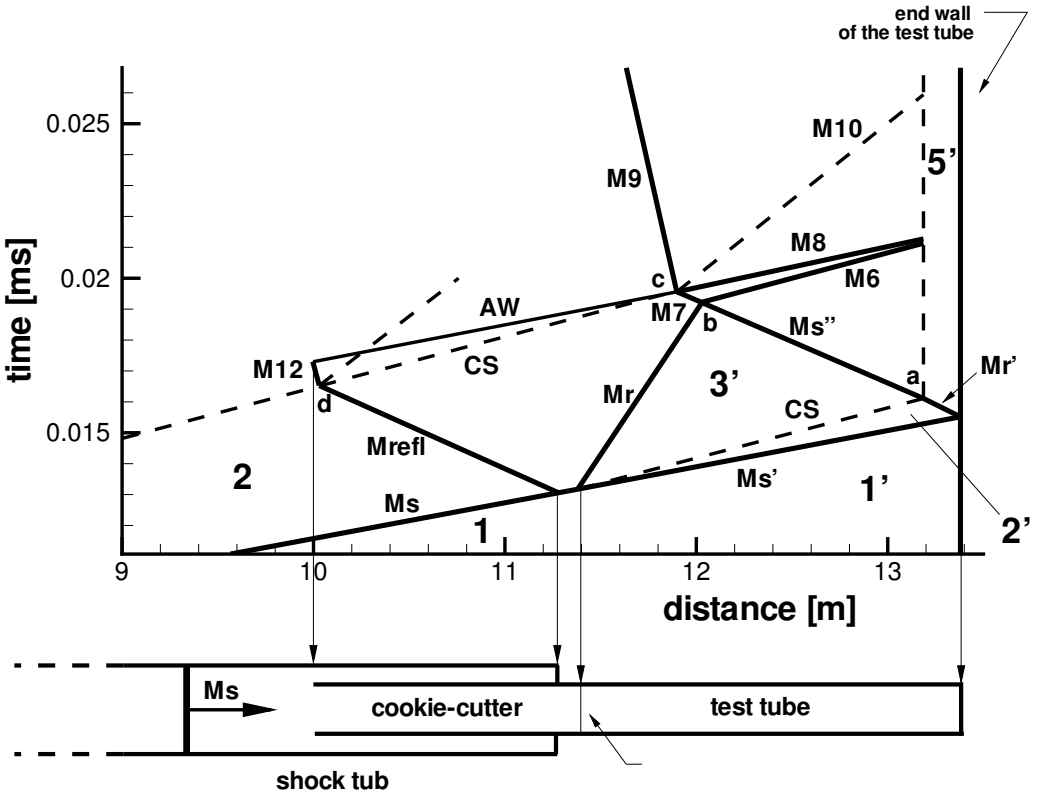

Figure 23: A close-up view of the x-t diagram from Fig. 22.

Table 2: Pressure ratios and corresponding Mach numbers M_s and velocities U_s of the shock waves after diaphragm rupture. Ideal performance computations based on (1) with air in driver and driven sections, modeled with $\gamma = 1.4$.

P_2/P_1	P_4/P_1	M_s	U_s (m·s^{-1})
3	11.4	1.65	574.7
5	46.1	2.10	731.4
7	137.3	2.48	863.8
9	355.1	2.80	975.2
11	850.5	3.09	1076.2

by the cookie-cutter breaks the diaphragm between the cookie-cutter and the detonation test tube. In all cases, a shock wave M_s' is transmitted into the combustible medium of the test tube. At the same time, a wave M_r is reflected from the interface: whether this is a shock or rarefaction depends on the physical properties - impedance of a material - of the shocked air and combustible mixture. Impedance of a material is a product of material density and sound speed. If the impedance of the combustible mixture is larger than that of the shocked air, a shock wave is reflected. If the impedance of the combustible mixture is smaller, a rarefaction is reflected. However, in the present study, the reflected shock wave M_r was a

weak or acoustic wave in all cases considered (see Table 3). The transmitted shock wave M_s' changes the combustible mixture from state $1'$ to state $2'$. The reflected wave passes through the previously shocked air changing it from state 2 into state $3'$. Similarly to the situation arising after the rupture of the first diaphragm, a contact surface between states 2 and $3'$ is created and the conditions $P_{2'} = P_{3'}$ and $u_{2'} = u_{3'}$ are prescribed. The analysis is best illustrated graphically in a P-u diagram, (Fig. 24).

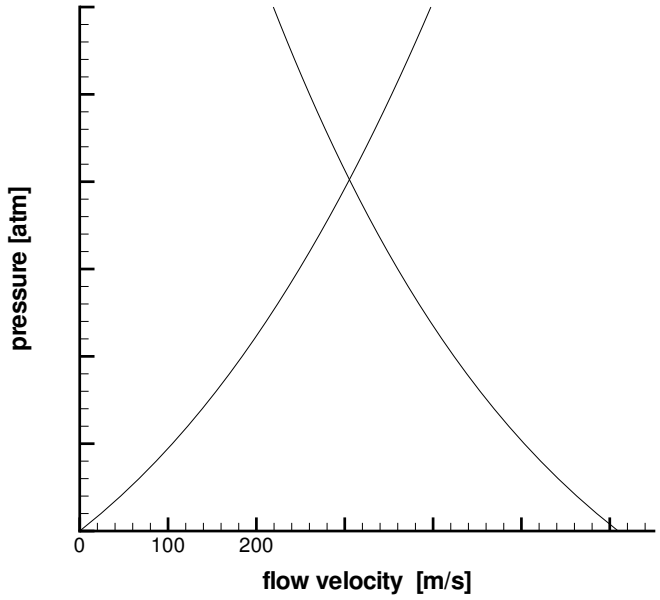

Figure 24: The P-u diagram for transmission and reflection of the incident shock wave at the cookie-cutter - test tube interface. The situation corresponds to case number 7 - see Table 3

The curve intersecting the origin represents the shock wave in the combustible mixture in the detonation test tube. In all cases the initial pressure was $P_{1'} = 1$ atm. The curve intersecting the x-axis at 600 m·s^{-1} corresponds to the wave reflected into the air. The values of pressures $P_{2'}$ and $P_{3'}$ and flow velocity $u_{2'}$ and $u_{3'}$ across the contact surface can be determined from the point of intersection of the curves. To analytically find the pressure and velocity values, a set of P-u equations was solved with use of MATHEMATICA:

For transmitted wave:

$$u_{2'} = a_{1'}(P_{2'} - P_{1'})\frac{\sqrt{2}}{\sqrt{\gamma_{1'}P_{1'}((\gamma_{1'}+1)P_{2'} + (\gamma_{1'}-1)P_{1'})}}\,,$$

and for reflected wave:

$$u_{3'} = u_2 - a_2(P_{3'} - P_2)\frac{\sqrt{2}}{\sqrt{\gamma_2 P_2((\gamma_2+1)P_{3'} + (\gamma_2-1)P_{2'})}}\,.$$

Knowing the pressures ratios $P_{2'}/P_{1'}$ and $P_{3'}/P_2$, the Mach numbers of the transmitted (M_s') and reflected (M_r) waves were calculated. The same procedure was subsequently employed four times to the points of **a**, **b**, **c** and **d** (see Fig. 23), which are:

point a: The point of interaction between a reflected shock wave M_r' from the flat end of the detonation test tube with the contact surface CS

point b: The point of interaction between the transmitted shock wave M_s'' with the oncoming reflected wave M_r

point c: Interaction between a transmitted shock wave M_7 with the contact surface CS emerged after the rupture of the first diaphragm

point d: Interaction outside the cookie-cutter between a reflected shock wave M_{refl} from the end wall of the shock tube with the contact surface created after the first diaphragm was broken.

The transmitted shock wave M_s' reflects after reaching the flat end wall of the detonation test tube. A passage of the reflected shock wave M_r' changes the previously shocked combustible mixture from state $2'$ into state $5'$ and leaves it at rest at pressure $P_{5'}$ and temperature $T_{5'}$. The values of these parameters underestimate the conditions under which the shock focusing and initiation of a detonation inside the reflector cavity can take place. The reflected shock wave impinges upon the contact surface afterwards, which is marked as point **a** in the x-t diagram (Fig. 23). A transmitted shock wave M_s'' and a reflected acoustic wave are created - this reflected wave does not cause any appreciable change in the combustible mixture. After interaction - point **a**, the contact surface remains at rest, which is represented by vertical dashed line starting from that point. From the position of the vertical line in respect to the position of the end wall of the test tube it is possible to determine the thickness x to which the combustible mixture was compressed. This was used to compute how to mount the pressure transducers and ion probes (see Fig. 18). The calculations were performed for nine cases of different combustible mixtures and pressure ratios P_4/P_1. The results are presented in Table 3.

Table 3: The results of calculations of performance of the test section for nine cases. The value x is the final thickness of the compressed test mixture.

case	P_4/P_1	combustible	M_s	$M_{s'}$	M_r	$M_{r'}$	$M_{s''}$	$P_{5'}/P_1'$	T_5' (K)	x (m)
1	46.1	C_3H_8 - air	2.10	2.12	1.0	1.73	1.81	18.5	737.3	0.27
2	137.3	H_2 - O_2	2.48	2.52	1.0	1.77	1.97	17.1	776.3	0.31
3	137.3	H_2 - air	2.48	2.34	1.0	2.20	1.98	25.2	925.2	0.24
4	137.3	C_2H_4 - O_2	2.48	2.53	1.0	1.80	2.00	33.7	828.0	0.16
5	137.3	C_2H_4 - air	2.48	2.49	1.0	1.92	1.98	30.9	940.3	0.20
6	137.3	C_3H_8 - O_2	2.48	2.58	1.0	1.71	2.02	36.8	772.4	0.14
7	137.3	C_3H_8 - air	2.48	2.51	1.0	1.89	1.98	31.7	919.8	0.19
8	850.5	C_2H_4 - air	3.09	3.11	1.0	2.11	2.19	60.4	1284.6	0.14
9	850.5	C_3H_8 - air	3.09	3.13	1.0	2.08	2.20	62.2	1251.8	0.13

At point **b** two waves, M_6 and M_7, are created after interaction between the transmitted shock wave M_s'' and the reflected acoustic wave M_r. This interaction does not cause significant changes in both impinging waves: the wave M_6 originating from the wave M_r is an acoustic wave traveling towards the reflector and the wave M_7 is, in fact, the slightly strengthened transmitted shock wave M_s''. Almost immediately after interaction at point **b** the shock wave M_7 meets at point **c** the oncoming contact surface which arose after the first diaphragm ruptured. The transmitted shock wave M_9 travels away from the detonation test tube. The reflected shock wave M_8 ultimately converges with the acoustic wave M_6 at the contact surface originating from the rupture of the second diaphragm.

At some point, the portion of the shock wave M_s on the outside of the cookie-cutter undergoes a reflection from the end wall of the shock tube. A reflected shock wave, denoted M_{refl} in Fig. 23, interacts with the contact surface originating from bursting of the first diaphragm - point **d** in the x-t diagram. After this interaction the transmitted shock wave M_{12} is reduced to an acoustic wave AW when it reaches the inlet of the cookie-cutter.

The interaction of the reflected shock wave M_{refl} and the contact surface takes place outside the cookie-cutter, in the space between the cookie-cutter and the shock tube. This allows the contact surface to enter the cookie-cutter before an acoustic wave is created. Thus, the acoustic wave AW originating from the shock wave M_{12} travels down the cookie-cutter following the contact surface. However, due to the pressure ratio P_4/P_1 used in this example (see Table 2), the temperature behind the contact surface is lowered by a factor of 3.2 for the lowest P_4/P_1 ratio and up to 8.4 for the highest P_4/P_1 ratio. Consequently, the values of the sound speed are decreased by the factor of 1.8 to 2.9, respectively. This enables us to minimize the length of the cookie-cutter. The length of the cookie-cutter is determined by the point of convergence of the contact surface and the acoustic wave - point **c** in the x-t diagram. As both the position of this point and the slope of the line representing the acoustic wave are known, the position of the inlet of the cookie-cutter is established from the point of intersection of the acoustic wave and the reflected shock wave M_{12}. The maximum time of measurement can be established from the time coordinates of the points **a** and **c**. The detailed calculation results are presented in Table 4.

Table 4: The maximum time of measurement and the calculated length of the cookie-cutter for the nine mixture cases considered.

case	P_4/P_1	combustible	t_m (s)	y (m)
1	46.1	C_3H_8 - air	7.6	1.77
2	137.3	H_2 - O_2	5.2	1.38
3	137.3	H_2 - air	5.0	1.38
4	137.3	C_2H_4 -O_2	5.1	1.38
5	137.3	C_2H_4 - air	5.0	1.38
6	137.3	C_3H_8 - O_2	5.3	1.38
7	137.3	C_3H_8 - air	5.0	1.38
8	850.5	C_2H_4 - air	3.1	1.10
9	850.5	C_3H_8 - air	3.1	1.10

3.5 Operation of the Experimental Facility

Several different diaphragms were used to generate the incident shock wave in the shock tube. Diaphragms were made of dead-soft aluminium. Two alloys of different thickness were used: Al1100-0 (3 mil., 6 mil., 12 mil., 20 mil and 40 mil. thick, 1 mil = 0.001 in.) and Al2024 (40 mil. thick). Each alloy combined with one of two cutters yielded a different burst pressure and, consequently, shock wave Mach numbers varying from 1.1 to 2.4. The burst pressure data versus diaphragm thickness for both aluminium alloys used in the experiments are shown in Fig. 25. All tests were carried out with air in both the driver and driven section.

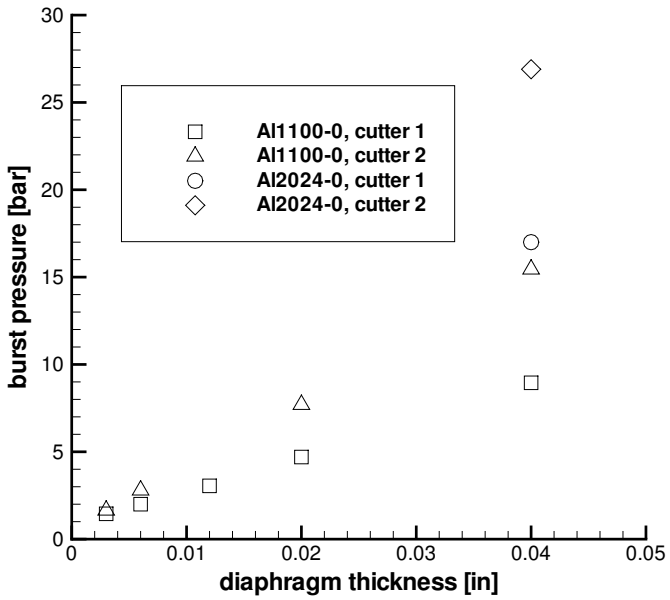

Figure 25: Burst pressure data for two different aluminium alloy diaphragms for GALCIT 6 Inch Shock Tube. Burst pressure is given as the difference between driver section pressure P_4 and driven section pressure P_1 at the moment of diaphragm rupture.

Small cutting blades were originally intended to help rupture the 0.0005 in. thick Mylar diaphragm separating combustible mixture filling test section from inert gas inside the shock tube and the cookie-cutter. However, preliminary testing on ethylene-oxygen and ethylene-oxygen with 20% dilution with nitrogen revealed that the cutting blades could trigger unwanted deflagration or detonation due to diffraction of the incident shock wave on the blades. The phenomena was observed for an incident shock Mach number as low as 1.3. As a result, the blades were not used in the experiments.

Prior to each test, the diaphragms were placed in the shock tube hydraulic clamp and between the test tube and the cookie cutter. After the test tube was secured by the four latch clamps, the entire facility was evacuated and then filled with required gases - the driven section with nitrogen, the driver section with air and the test section with premixed combustible test mixture. Test section gases were prepared by method of partial pressures in the 9.25 liter mixture preparation vessel and premixed for at least one hour with a brushless

fan mounted inside the vessel. In most cases, the test mixture was left overnight to premix.

Both sections of the shock tube were filled simultaneously with required gases, the pressure in the driver section being kept slightly higher (about 10 kPa) than in the driven section to assure diaphragm bulging in one direction only. Once the desired pressure in the driven section was obtained, the test section was filled with test mixture to the same pressure as in the driven section. The driver section was then filled from a compressed air source until the shock tube diaphragm ruptured. This way, a shock wave of the required Mach number in the driven section was created. The incident shock wave reached the cookie-cutter which protruded into the end of the driven section and was filled with the same gas as the driven section. The central part of the shock wave was smoothly cut out and subsequently ruptured the second diaphragm separating the cookie-cutter from the test tube. The shock wave traveled down the detonation test tube and compressed the combustible mixture filling the test tube. Finally, the shock wave focused inside the reflector. The outer part of the incident shock wave formed the ring which traveled outside the cookie-cutter until it reached the end-wall of the shock tube, reflected from it and traveled back. That way, the reflected incident shock wave, after reaching a second time the inlet of the cookie-cutter, met an abrupt area expansion (by a factor of four) and was suppressed, forming a weak acoustic wave. This wave, after diffraction at the edge of the cookie-cutter, propagated in shock tube as well as within the cookie-cutter.

The pressure transducers were used to record the shock arrival times in order to calculate the incident shock wave Mach number. The data from every neighbouring two pressure transducers allowed estimation of the accuracy of the Mach number which fell within 4% to 8% along the test tube. The incident shock wave changed the test mixture from state 1' to state 2'. The initial pressure, $P_{1'}$, of the test mixture was chosen to fulfill the condition of the pressure $P_{2'}$ to be 100 kPa. To calculate actual pressure $P_{2'}$ behind the shock wave, the data from the two last pressure transducers before the reflectors was used. The results of the data reduction are tabulated in Appendix C.

4 Test Results

4.1 Classification of Data

Four main categories of combustion mode were observed during experiments: prompt detonation inside the reflector, deflagration-to-detonation transition (DDT), deflagration outside the reflector and no combustion. Moreover, two additional modes were observed in cases of low nitrogen dilution: direct initiation of detonation and direct deflagration caused by the incident shock wave before it focused inside the reflector cavity. Results illustrating these combustion modes are presented in this section as combined pressure-time and space-time diagrams Figs. 26 to 33. A complete set of diagrams for all tests performed are given in Appendix D and the test conditions are tabulated in Appendix C.

4.1.1 Detonation Inside Reflector

An example of a prompt detonation inside the reflector is shown in Fig. 26. The pressure transducers mounted in the ports from 14 to 2 recorded propagation of the incident shock wave of Mach number 1.89 in the test section. After approximately 2.5 ms, the shock wave focused inside the reflector. This is indicated by the significant rise in pressure recorded by the pressure transducer at the apex of the reflector (port 1). The reflected shock immediately transited to a detonation traveling back into the test tube wave was registered by the pressure transducers along the tube and the arrival of the reaction zone was detected by ion probes (filled squares in the diagram). The coupling between the shock wave and reaction zone is evident. The dashed line connecting ion probes signals indicates the detonation wave velocity, which lies within 10% of Chapman-Jouguet velocity. The detonation wave was fully developed at the edge of the reflector (port 2). The combustible mixture inside the test section was compressed by the incident shock wave, although it is difficult to determine to what thickness since all ion probes indicated the arrival of flame. However, it appears that transducers at ports 13 and 14 recorded only a reflected shock wave.

4.1.2 Deflagration-to-Detonation Transition Outside the Reflector

The mode of deflagration-to-detonation transition is shown in Fig. 27. We can observe the incident shock wave ($M_s = 1.68$) and reflection. Unlike the previous case, the detonation was not immediately initiated but the shock wave was followed by the accelerating deflagration, indicated by the gently curved dashed line which connects the ion probe signals. After less than 3 ms, at port 12 or slightly nearer, the coupling between the shock wave and the reaction zone took place. A strong retonation (backward propagating detonation) wave, recorded by transducers at ports 8 to 1, traveled towards the reflector while the flame propagated further up the test tube at constant velocity (indicated by the straight fragment of the dashed line connecting three subsequent ion probes signals in the diagram). A signal was detected by last three ion probes but pressure signals are not available in that region. Since the ion signal propagation speed was characteristic of a Chapman-Rouget detonation velocity, this suggests the creation of the detonation wave. Due to compression of the test mixture by the incident shock wave, pressure transducers at port 13 and 14 recorded only a strong shock wave.

4.1.3 Deflagration Outside Reflector

As in the DDT mode, the deflagration-outside-reflector mode is characterized by deflagration that lags behind the reflected shock wave. However, the compressed test mixture is burnt before the deflagration can accelerate enough to trigger the DDT phenomena. Three subcases, shown in Figs. 28, 29 and 30 can be distinguished depending on the incident shock wave Mach number, test mixture, and type of reflector. The subcase of the Mach 1.21 incident shock wave propagating in hydrogen-oxygen mixture with 20% nitrogen dilution towards the $D/h = 1.25$ reflector (Fig. 28) is the closest one to the DDT mode. After 4 ms the transducer at port 13 recorded a shock-wave-like pressure build-up due to deflagration. The shock wave traveling further on the test section was detected by transducer at port 14. The shock wave, propagating towards the reflector and recorded by remaining transducers, overlapped the smooth pressure build-up caused by deflagration. Fig. 29 represents the subcase of Mach 1.48 shock wave and an ethylene-oxygen-40% nitrogen test mixture. The reflector used had $D/h = 1.25$. The duration of deflagration detected by the ion probes was almost twice as long as in the previous subcase. The shock wave generated by deflagration and propagating outside the test tube was recorded by the transducer at port 13 after 5 ms and then by the transducer at port 14. A smooth pressure build-up caused by deflagration was detected by the remaining transducers resulted in the visible bump at 5 ms which occurred simultaneously within the last 0.5 m of the test tube. The last case shown in Fig. 30 ($M_s = 1.87$, ethylene-oxygen-60% nitrogen mixture and $D/h = 0.5$ reflector), indicates only deflagration trailing behind the reflected shock wave. A smooth pressure rise was also detected by the transducers mounted at ports 1 to 8.

4.1.4 No Combustion

In some cases, no ionization was detected by the ion probes. An example of a no combustion mode is presented in Fig. 31. The pressure transducers recorded the incident shock wave of $M_s = 1.45$, focusing phenomena, and then a reflected wave traveling back through the test tube.

4.1.5 Initiation of Detonation and Deflagration by Incident Shock

The initiation of detonation behind the incident wave was sometimes observed before the incident shock wave reached the reflector. In Fig. 32, the shock wave propagating down the test tube in ethylene-oxygen mixture with 20% nitrogen dilution caused combustion shortly after passing by a transducer mounted in port 13. According to the type of diaphragm used between the driven and the driver section of the shock tube and based on the burst pressure data, the expected incident shock wave Mach number should have been approximately 1.41. The signals from the ion probes numbered from 7 to 1, combined with the pressure transducer traces from ports 12 to 2 indicate a fully-developed detonation of Mach number 7.29, traveling towards reflector. The wave subsequently focused inside the cavity of the reflector and traveled back into the test tube as a shock wave. Similarly, the incident shock wave with an expected value $M_s = 1.85$ in a hydrogen-oxygen mixture with 20% nitrogen dilution generated combustion, shown in Fig. 33 as open squares. A detonation was not immediately initiated, but combustion caused an acceleration of the incident shock wave to $M_s = 2.28$.

A Mach number of 2.28 is sufficient to initiate a detonation by focusing inside the reflector cavity. The detonation wave coming back into the test tube was indicated by pressure transducers traces and four ion probes signals.

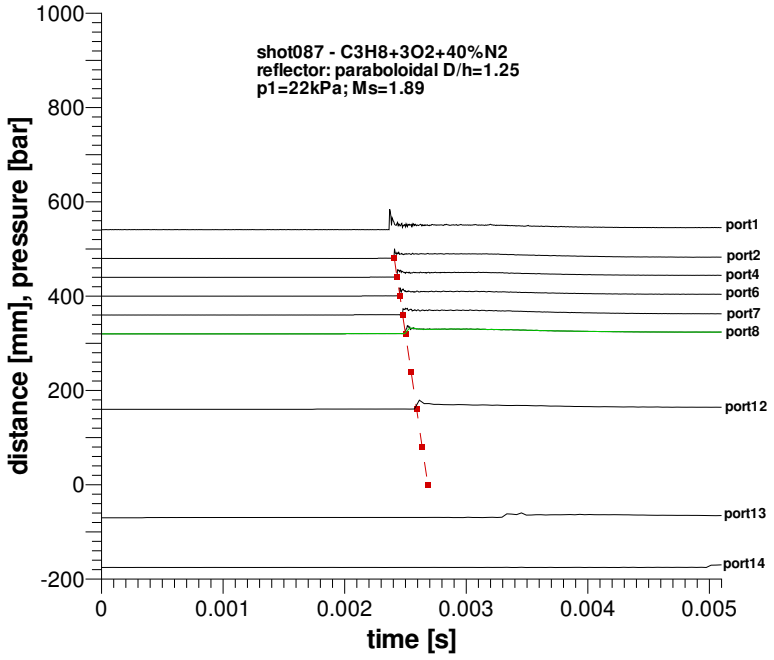

Figure 26: Detonation inside reflector (shot 087); test mixture: C_3H_8+5O_2+40%N_2; incident shock Mach number: $M_s = 1.89$.

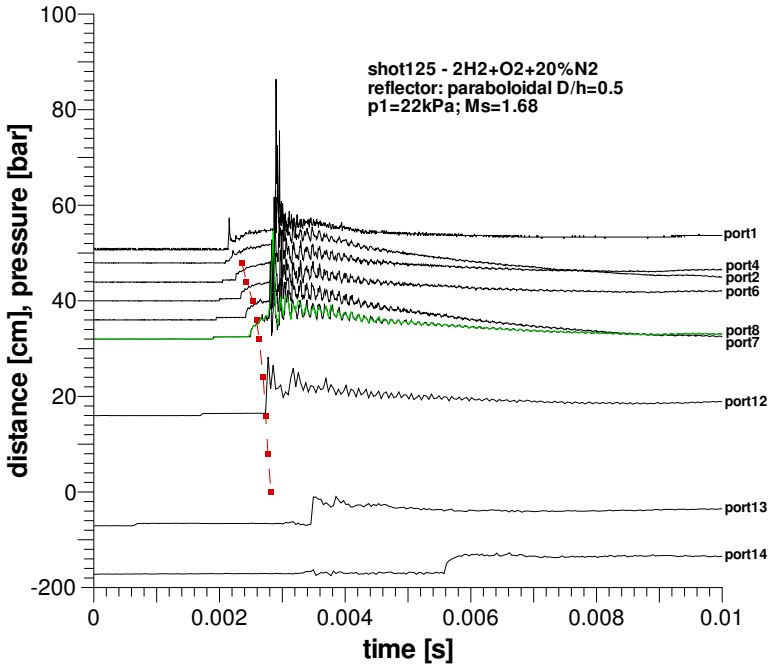

Figure 27: Deflagration-to-detonation transition (shot 125); test mixture: $2H_2+O_2+20\%N_2$; incident shock wave Mach number: $M_s = 1.68$.

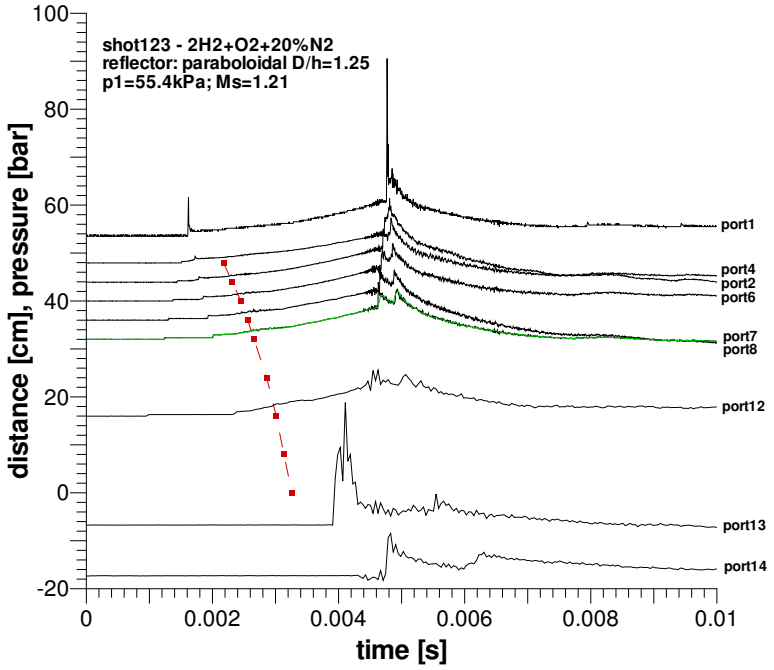

Figure 28: Deflagration outside reflector (shot 123); test mixture: $2H_2+O_2+40\%N_2$; incident shock Mach number: $M_s = 1.21$.

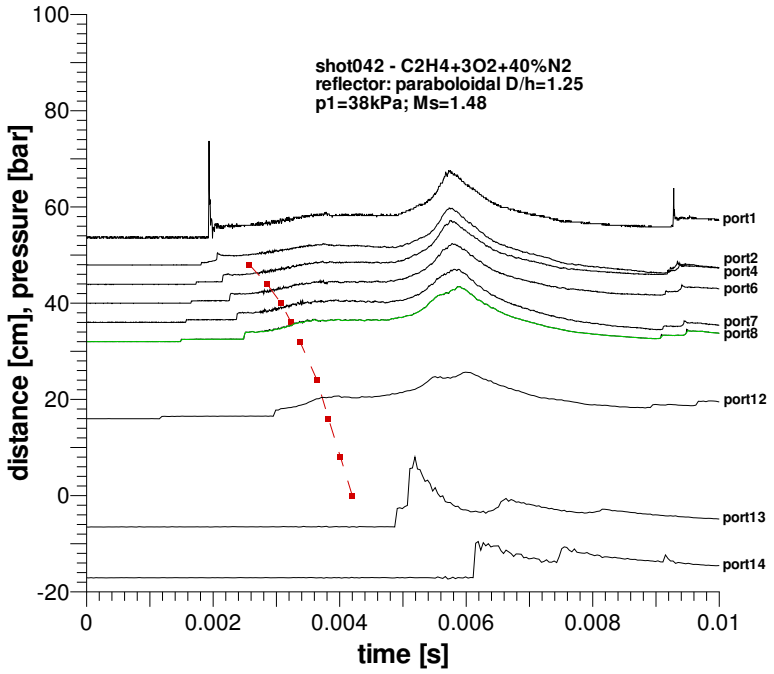

Figure 29: Deflagration outside reflector (shot 042); test mixture: C_2H_4+3O_2+40%N_2; incident shock Mach number: $M_s = 1.48$.

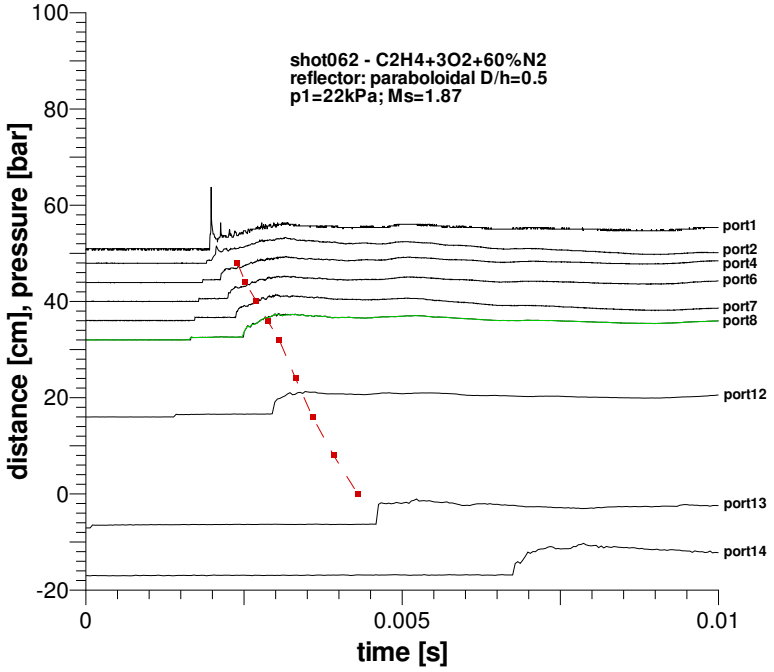

Figure 30: Deflagration outside reflector (shot 062); test mixture: C_2H_4+3O_2+60%N_2; incident shock Mach number: $M_s = 1.87$.

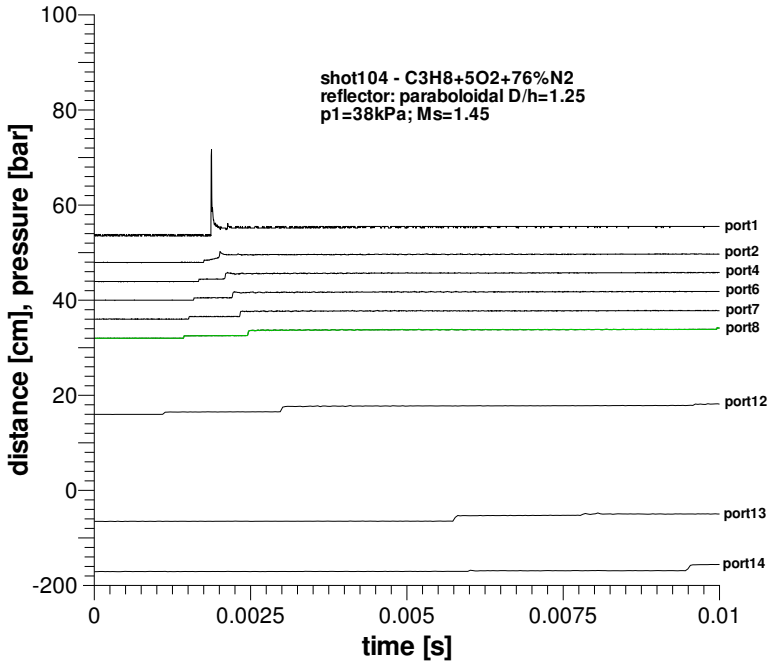

Figure 31: No combustion (shot 104); test mixture: C_3H_8+$5O_2$+$76\%N_2$; incident shock Mach number: $M_s = 1.45$.

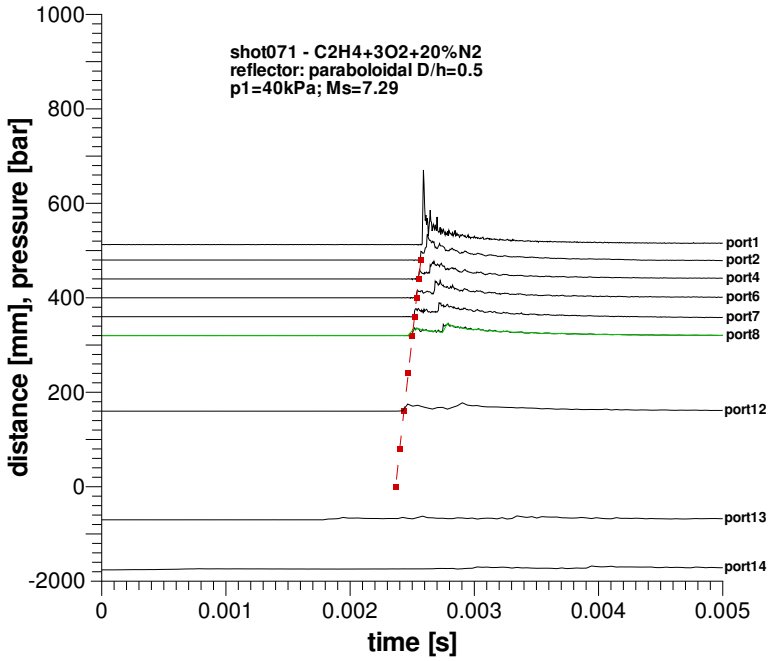

Figure 32: Initiation of detonation (shot 071) behind the incident wave; test mixture: C_2H_4+$3O_2$+$20\%N_2$; incident shock Mach number: $M_s = 1.41$.

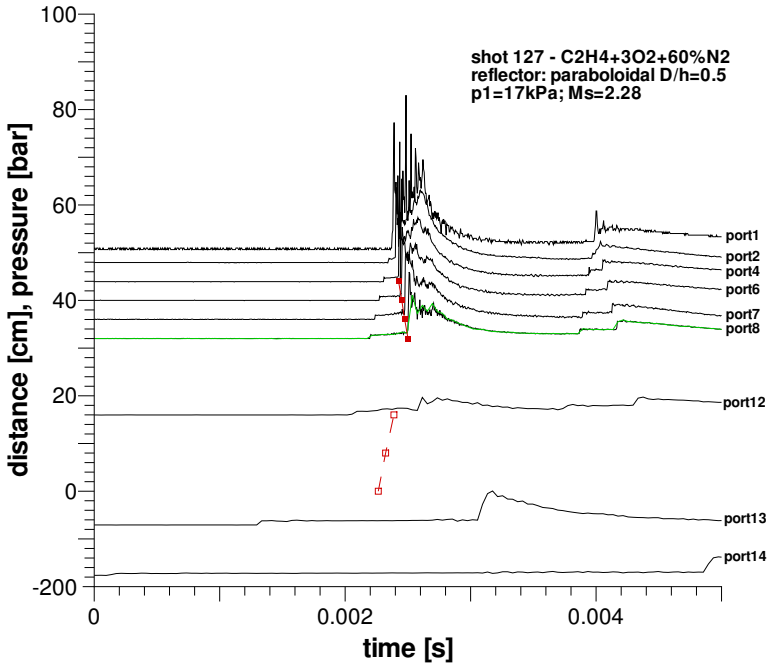

Figure 33: Initiation of deflagration (shot 127) behind the incident wave; test mixture: $2H_2+O_2+20\%N_2$; incident shock Mach number: $M_s = 1.85$.

5 Discussion and Conclusions

Direct initiation of detonation due to shock focusing could only be obtained for mixtures with the smallest amount of dilution and in two deepest reflectors. The results of the testing are summarized in Figs. 34 to 41. The graphs in these figures show the mode of combustion for three stoichiometric mixtures of ethylene-oxygen, propane-oxygen and hydrogen-oxygen with varying nitrogen dilution, combined with three paraboloidal reflectors of depth-to-height ratio $D/h = 0.5; 1.25; 2.0$ and a flat reflector. The numbers next to the symbols are shot order number and, inside the parentheses, Mach number of the incident shock wave, and initial pressure of the test mixture. In order to obtain a range of Mach numbers, the the pressure of the test mixture P_1 was varied from 73 kPa for the lowest Mach number of the incident shock wave to 13 kPa for the strongest one. The post-shock pressure $P_{2'}$ was approximately held constant (see Table C) but the post-shock temperature $T_{2'}$ varied with the incident shock Mach number. This has to be kept in mind when interpreting the data.

The results presented in Figs. 34 to 37 show that, for ethylene, the conditions under which a given mode of combustion occurs are very similar for two separate pairs of reflectors: the two deepest reflectors (Figs. 36 and 37) and the flat and the shallowest ones (Figs. 34 and 35). Hence, only the shallowest reflector ($D/h = 0.5$) and the deeper reflector ($D/h = 1.25$) were used to test propane and hydrogen fuels. The results indicate that for a given diluent concentration, sufficiently strong incident shock wave is required to promptly initiate a detonation inside the reflector cavity. As the dilution increased in the mixture, the Mach number had to be increased to obtain initiation of combustion. The highest Mach number achieved during experiments was $M_s = 2.40$. At this value, prompt initiation was obtained for two deepest reflectors for every mixture tested except the case of propane-air (76% nitrogen dilution) mixture. For the shallowest and flat reflectors prompt initiation was obtained for hydrogen cases only.

With decreasing Mach number of the incident shock wave, the deflagration outside the reflector was observed until no combustion mode occurred for low enough Mach numbers. At higher Mach numbers, DDT occurred, although mostly for shallowest or flat reflector.

Additionally, two cases of direct initiation of detonation and direct deflagration before the incident shock wave reached reflector were observed: for 20% nitrogen dilution in ethylene-oxygen mixture (Fig. 34) - direct detonation, and for 20% nitrogen dilution in hydrogen-oxygen mixture (Fig. 40) - direct deflagration.

As expected, the two deepest reflectors are much more effective for prompt initiation of detonation and deflagration after focusing than the shallowest and flat reflectors. The results obtained for ethylene-oxygen with varying nitrogen dilution indicate no difference between the performance of $D/h = 1.25$ and $D/h = 2$ reflectors when the incident shock waves of higher Mach numbers were used and prompt detonation was achieved. Deflagration outside the cavity of the reflector was observed for 10% to 15% lower Mach numbers in case of the $D/h = 1.25$ reflector. It was also easier to achieve the deflagration outside the reflector for $D/h = 0.5$ reflector than for the flat wall. Since no prompt detonation was observed for the shallowest and flat reflector nothing is said about the effectiveness of these reflectors for the prompt initiation of detonation. The results for all fuels and two reflectors, $D/h = 1.25$ and $D/h = 0.5$, show that the lower Mach numbers were used to cause any combustion mode in the stoichiometric hydrogen-oxygen-nitrogen mixtures than stoichiometric ethylene-oxygen-

nitrogen and propane-oxygen-nitrogen mixtures. The prompt detonation was observed for hydrogen-oxygen-nitrogen and both of the reflectors. For hydrocarbon fuels, this mode of combustion was achieved for the deeper reflector only. The significantly higher Mach numbers were necessary to cause combustion in propane-oxygen-nitrogen than in two other fuel mixtures. During the experiments the 2.41 Mach number was the higher achieved in the test tube. This value proved not to be adequately high to cause the initiation of detonation inside the cavity of $D/h = 1.25$ reflector and propane-air mixture. The trends in the Mach number increase with the increase of nitrogen diluent for prompt initiation of detonation for ethylene-oxygen-nitrogen and the rough approximation for the propane-air case and $D/h = 1.25$ reflector suggest that to achieve the prompt initiation of detonation the Mach number about 3.5 would be required.

There are a number possible directions for future work. One possibility is to determine how the initial pressure of the test mixture influences the effectiveness of the initiation of detonation in the paraboloidal reflectors. The use of different reflector shaped could also be examined. Preliminary numerical studies on the $D/h = 1.25$ and $D/h = 0.5$ of axisymmetric ellipsoidal reflectors were undertaken. Ellipsoidal reflectors have a wider cross-section than the paraboloidal reflectors. As a consequence, the pattern of the reflected and focusing shock waves is more complex than for the paraboloidal reflectors examined in the present study. The results of the present study could be compared to those obtained from the experiments on the initiation of detonation via imploding shock waves (Jackson and Shepherd, 2004, Jackson, 2005). Photo-imaging of the focusing and initiation of detonation processes inside the cavity of the reflector could also be explored.

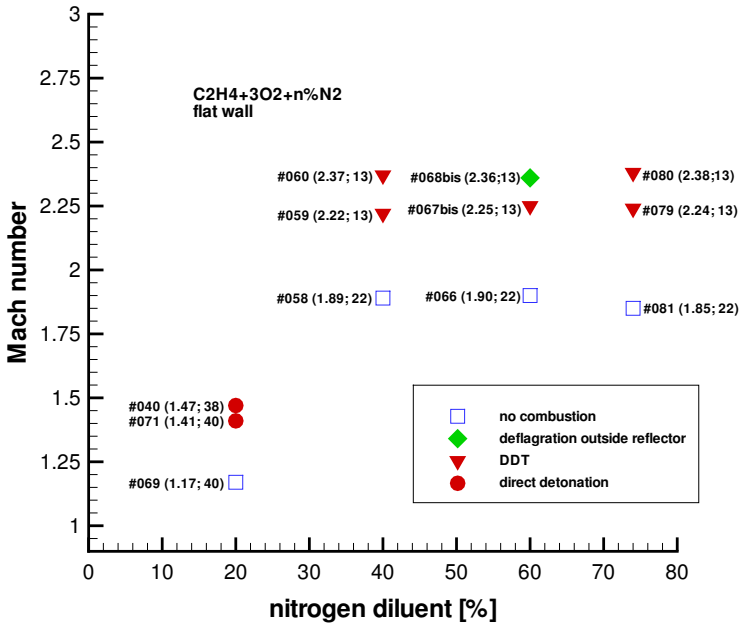

Figure 34: Influence of incident shock Mach number on mode of combustion in stoichiometric ethylene-oxygen mixture with varying nitrogen dilution for flat reflector.

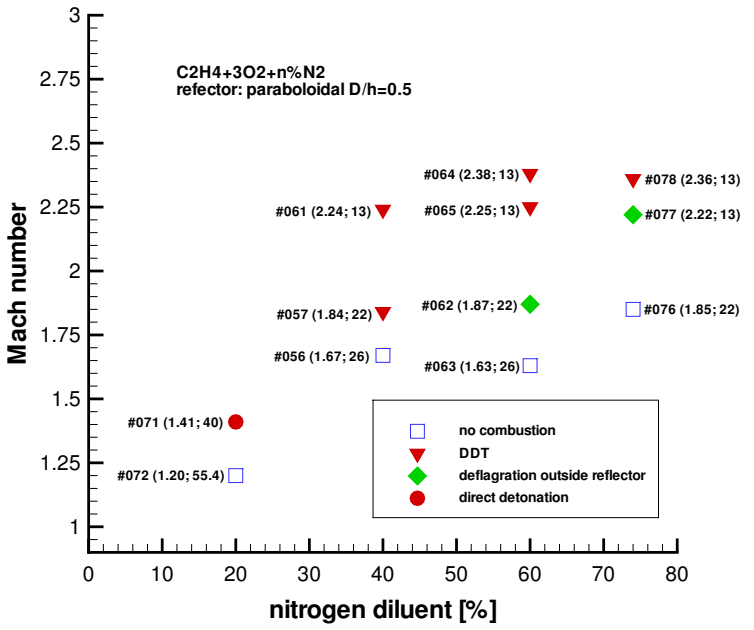

Figure 35: Influence of incident shock Mach number on mode of combustion in stoichiometric ethylene-oxygen mixture with varying nitrogen dilution for paraboloidal reflector of $D/h = 0.5$.

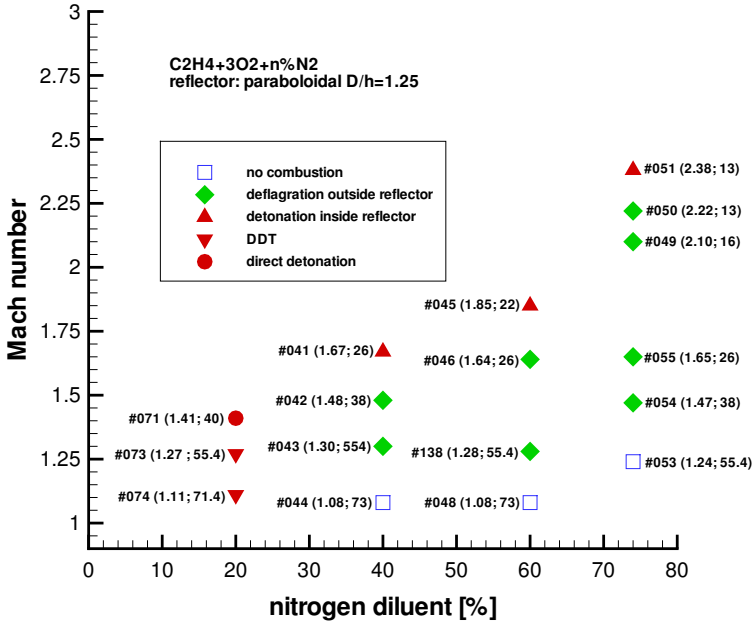

Figure 36: Influence of incident shock Mach number on mode of combustion in stoichiometric ethylene-oxygen mixture with varying nitrogen dilution for paraboloidal reflector of $D/h = 1.25$.

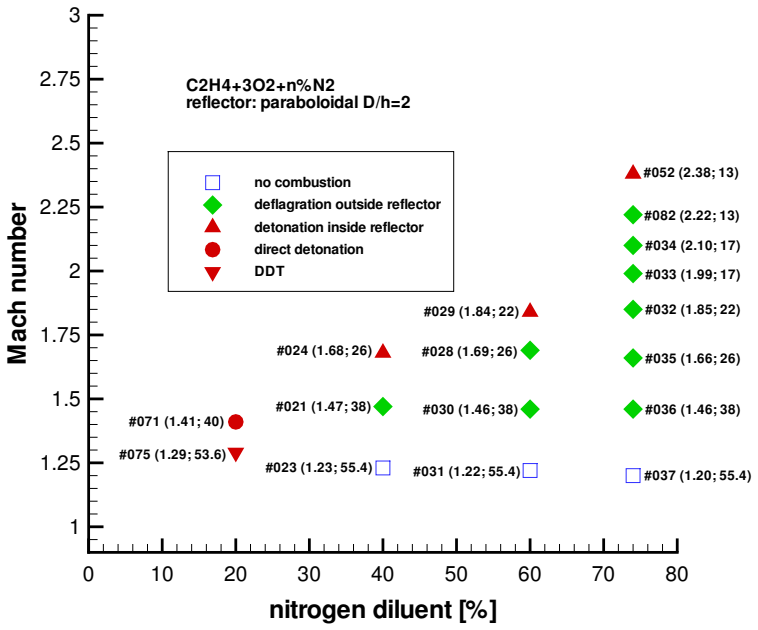

Figure 37: Influence of incident shock Mach number on mode of combustion in stoichiometric ethylene-oxygen mixture with varying nitrogen dilution for paraboloidal reflector of $D/h = 2.0$.

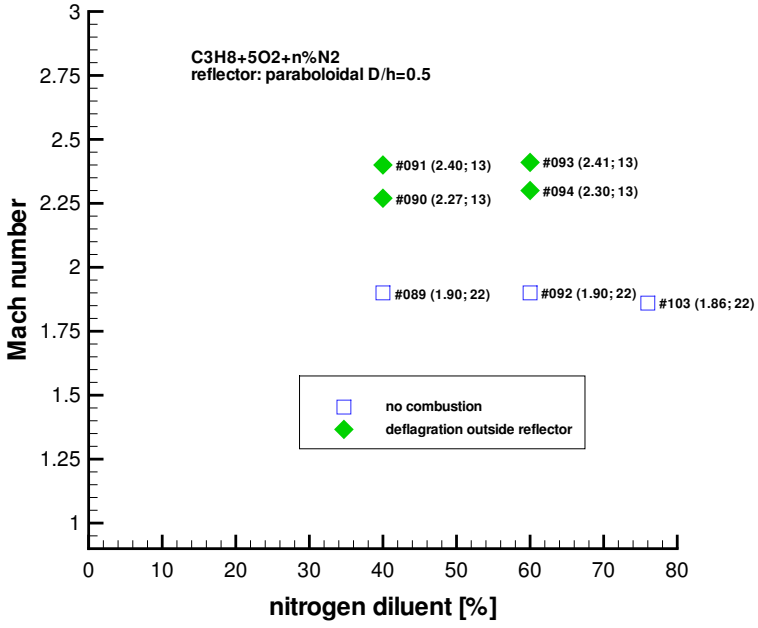

Figure 38: Influence of incident shock Mach number on mode of combustion in stoichiometric propane-oxygen mixture with varying nitrogen dilution for paraboloidal reflector of $D/h = 0.5$.

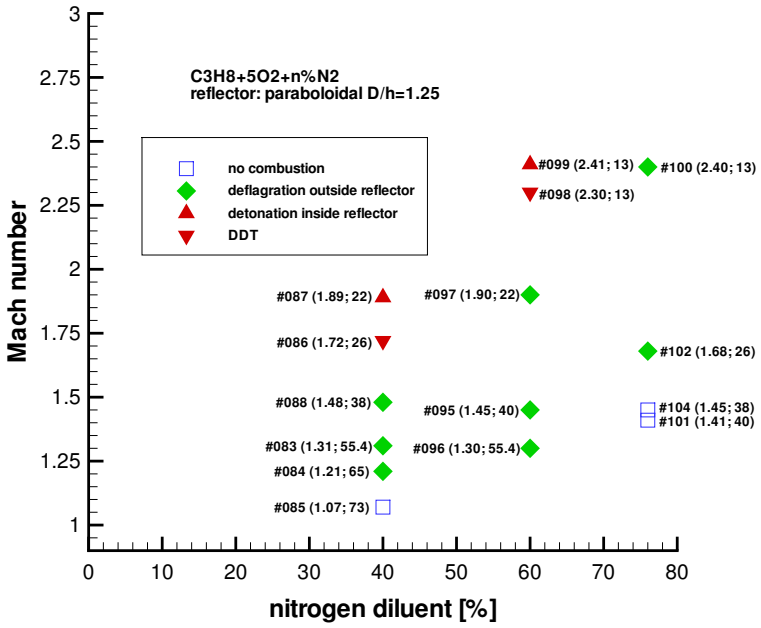

Figure 39: Influence of incident shock Mach number on mode of combustion in stoichiometric propane-oxygen mixture with varying nitrogen dilution for paraboloidal reflector of $D/h = 1.25$.

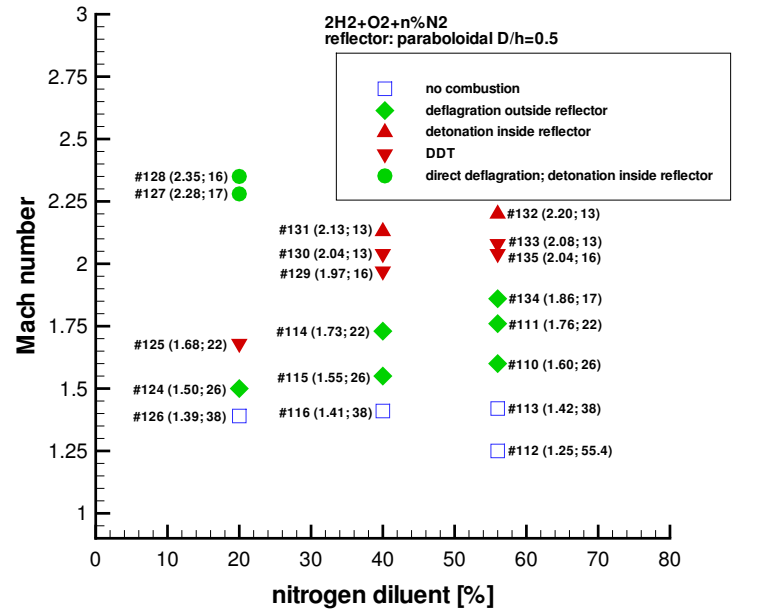

Figure 40: Influence of incident shock Mach number on mode of combustion in stoichiometric hydrogen-oxygen mixture with varying nitrogen dilution for paraboloidal reflector of $D/h = 0.5$.

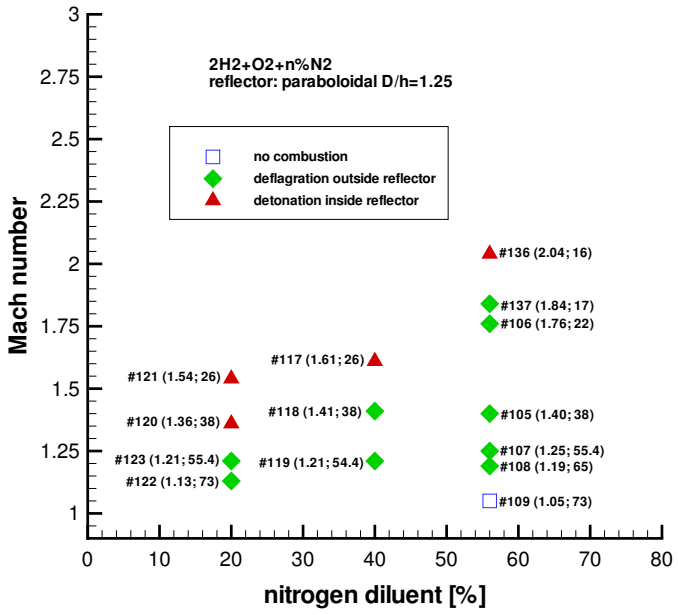

Figure 41: Influence of incident shock Mach number on mode of combustion in stoichiometric hydrogen-oxygen mixture with varying nitrogen dilution for paraboloidal reflector of $D/h = 1.25$.

6 Acknowledgement

The author thanks Scott Jackson for his indispensable work on the design, construction and testing of the experimental facility. He gratefully acknowledges professor Hans Hornung for his invaluable involvement in the numerical study presented in this work and Eric Wintenberger for his contribution to actual creating of the numerical simulations. Dan Lieberman and Florian Pintgen have proven to deliver unparallel assistance in any problems concerning editing and data presentation. He is also grateful to J. Haggerty and B. St. John for their patience and expertise during the construction process of the reflectors.

This work was supported by the Office of Naval Research Grant (ONR Grant Number N00014-03-1-0931) and the Polish-US Fulbright Comission through the 2003-2004 Fulbright Junior Research Grant (Program I.D. 15032017).

References

A.M. Bartenev, S.V. Khomik, B.E. Gelfand, H. Grönig, and H. Olivier. Effect of reflection type on detonation initiation at shock-wave focusing. *Shock Waves*, 10(3):205–215, July 2000. 2

W. Breitung, C. Chan, S. Dorofeev, A. Eder, B.E. Gelfand, M. Heitsch, H. Klein, A. Malliakos, J.E. Shepherd, E. Studer, and P. Thibault. Flame acceleration and deflagration to detonation transition in nuclear safety. state-of-the-art report by a group of experts. Technical Report NEA/CSNI/R(2000)7, OECD Nuclear Energy Agency, 2000. 2

C. K. Chan, D. Lau, P. A. Thibault, and J. D. Penrose. Ignition and detonation initiation by shock focussing. In *AIP Conference Proceedings*, volume 208, pages 161–166. AIP, 1990. 2

B.E. Gelfand, S.V. Khomik, A.M. Bartenev, S.P. Medvedev, H. Grönig, and H. Olivier. Detonation and deflagration initiation at the focusing of shock waves in combustible gaseous mixture. *Shock Waves*, 10(3):197–204, July 2000. 2

K. Izumi, S. Aso, and M. Nishida. Experimental and computational studies focusing processes of shock waves reflected from parabolic reflectors. *Shock Waves*, 3(3):213–222, September 1994. 3

S. I. Jackson and J. E. Shepherd. Detonation Initiation via Imploding Shock Waves. In *40th AIAA/ASME/SAE/ASEE Joint Propulsion Conference andExhibit*, Ft. Lauderdale, FL, July 2004. AIAA. 33

Scott Jackson. *Detonation Initiation via Wave Implosion.* PhD thesis, California Institute of Technology, Pasadena, California, May 2005. 13, 33

S. V. Khomik, S. P. Medvedev, A. N. Polenov, and B. E. Gelfand. Conditions of detonation initiation by focusing shock waves in a combustible gas mixture. *Combust Explos Shock Waves*, 43(6):697–702, November 2007. 2

H W Liepmann, A. Roshko, D. Coles, and B. Sturtevant. A 17-Inch Diameter Shock Tube for Studies in Rarefied Gasdynamics. *Review of Scientific Instruments*, 33:625–631, June 1962. 41

B E Milton. The focusing of shock waves in two-dimensional and axi-symmetric ducts. In *Proceeding of the International Workshop on Shock Waves Focusing*, pages 155–191, Sendai, Japan, 1989. 3

J. J. Quirk. AMRITA: A computational facility (for CFD modelling). *Lecture series - von Karman Institute for Fluid Dynamics*, 3:D1–D72, 1998. 4

J. A. Smith, D. Coles, A Roshko, and A J Prasad. A description of the GALCIT 6-in shock tube. Technical Report FM-67-1, Graduate Aeronautical Laboratories, California Institute of Technology, June 1967. 12, 41

B. Sturtevant and V. A. Kulkarny. The focusing of weak shock waves. *J. Fluid Mech.*, 73 (4):651–671, February 1976. 3

E. Wintenberger, H. Hornung, and J.E. Shepherd. Detonation initiation by shock focusing. Technical Report FM2001.00X, Graduate Aeronautical Laboratories, California Institute of Technology, 2001. This report was drafted in 2000-2001 and revised in 2021. iv, 1, 3, 5, 11

A 6-in Shock Tube

This appendix was authored by Eric Wintenberger and Joe Shepherd; it was published internally at GALCIT as a separate document in July 2002. This material is included as part of the present report to provide background on the 6-in shock tube.

The GALCIT 6-inch shock tube was designed and fabricated in the 1960s (Smith et al., 1967) to complement the performance of the GALCIT 17-inch shock tube (Liepmann et al., 1962). It was originally intended for investigations of reaction rate phenomena and radiation processes in highly ionized gases. The 6-inch shock tube retains the simplicity and repeatability of a cold gas driver, but, with the addition of hydrogen to the possible driver gases used, much higher shock Mach numbers may be achieved. Shock Mach numbers up to 20 were obtained in this facility, using a hydrogen driver and xenon as a test gas. The following sections describe the basic dimensions, vacuum characteristics and controls for the 6-in shock tube. The hydraulic clamping mechanism is also described in detail. The basic operation of the shock tube is explained.[2] A listing of the various shock tube components with their characteristics is included in appendix, as well as useful drawings of some of the most important pieces of the tube and a list of typical test conditions.

A.1 Driver and Driven Section

The GALCIT 6-inch shock tube consists of a conventional cold-gas driver section, a diaphragm transition section, and a driven section. The entire assembly is suspended from a central H-beam supported by a series of five inverted U-frames of welded I-beam bolted to the floor. The centerline of the shock tube is approximately 2.0 m above the floor. The tube is suspended at intervals from the main H-beam with a commercially available pipe clevis assembly.

The basic driver tube is 20 ft and 4 in long (6.2 m) and consists of three sections of 6.52 in (16.6 cm) internal diameter, type 321 stainless steel, seamless tubing with a wall thickness of 0.5 in (1.27 cm), clamped together. The driver as built by Smith et al. was originally only 2 m long and was subsequently extended in 1996 in order to increase the test time. The driver is connected to a 25.4 cm long transition section described subsequently. The driver section assembly has been hydraulically tested to a pressure of 150 atm without failure of seals or joints. The driver tube is suspended from the central H-beam on movable trolleys so that it can be rolled back when changing diaphragm. The driver vacuum pump line, the pressure gauge line used to monitor the driver pressure, and the driver gas fill line are connected to the driver end plate by means of flexible metal tubing. The driver may be vented to the atmosphere by a line running from the pressure gauge line through the roof of the building. When doing superatmospheric shots with toxic or flammable gases, the shock tube is vented first to the atmosphere through this vent line, then, when the pressure drops to one atmosphere, through a mechanical vacuum pump which also exhausts through the roof.

[2]This explanation is based on the discussion in Smith et al. (1967) and notes by E. Wintenberger, who reconstructed the control system in 2000.

The driven section is 37 ft long (11.28 m) and consists of a transition section and three 3.67 m lengths of type 321 stainless steel, seamless tubing with a nominal wall thickness of 0.5 in (1.27 cm), clamped together. The internal surface of these sections was honed to a surface finish of 10 to 20 microinch. The internal diameter of the tube is 6.021±0.002 in (15.293±0.005 cm) with a maximum step height at any joint less than 0.002 in (0.005 cm). The method of connecting one tube section to another uses beveled flange rings and a band clamp. A cross-sectional view of a typical joint is shown in Fig. 42. The driver end plate and the test section end plate are attached to the tube in a similar fashion. The beveled rings were machined from stainless steel forgings. The split-ring clamps were made from annealed 1040 carbon steel forgings, cut in half and nickel plated to minimize corrosion. A stainless steel "Marman" band clamp provides the force required to compress the O-ring in order to seal the joint.

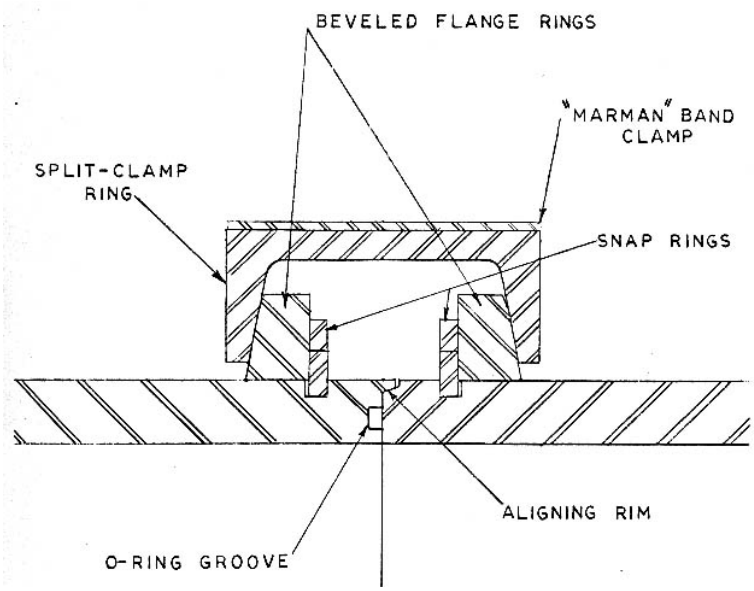

Figure 42: Sectional view of typical joint betweem two sections of the shock tube.

The driven section is equipped with several instrument ports. The instrument ports were designed to give a maximum aperture within the allowable wall thickness required by strength of materials. Each port consists of a 2.38 cm diameter access hole through the wall and a 5.4 cm diameter flat milled into the shock tube outer surface. The milled flat provides a surface for an O-ring seal. Four blind tapped holes located on the periphery of the flat are used to bolt the instrumentation plugs to the shock tube. Two such ports are located 20 cm and 70 cm from the downstream end of two tube sections. In the third section, at the end of the driven section, there are six instrumentation ports, three pairs diametrically opposed, as shown in Fig. 43. The distances from the end wall to the centerlines of the three pairs are 10.0 cm, 20.0 cm and 70.0 cm. The pair located at the 10 cm position has its axis rotated 90° from the other two pairs. The 50 cm distance between the ports on the upstream tube sections and between two of the three pairs in the downstream section permits measurement of shock speeds with less than 1% error.

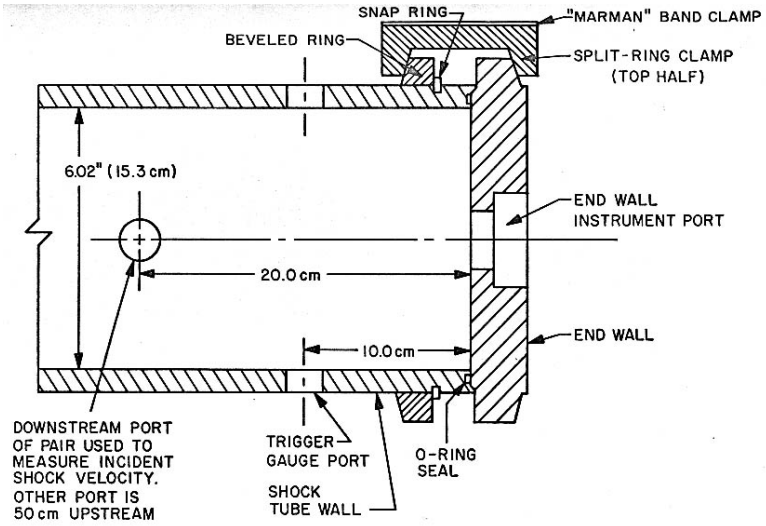

Figure 43: Cross-sectional view of end plate and test section.

A.2 Diaphragm transition section

The diaphragm transition section consists of the driver transition section, the driven transition section, the clamp and the hydraulic pressure ring, as depicted in Fig. 44. The clamping of the diaphragm is accomplished by inserting pressurized fluid between the driver transition section and the hydraulic pressure ring. The hydraulic pressure ring is clamped with the driven transition section using a U-shaped cross-section clamp. The force generated by the hydraulic fluid is counteracted by the clamp. Therefore the driver transition section is pressed against the driven transition section, clamping the diaphragm and making the seal. A spring return mechanism pushes the driver transition section back in place when the hydraulic pressure is removed, allowing space to place the diaphragm. The clamp consists of a ring cut in half, hinged at the top and latched at the bottom. It is suspended from above on a counter balance arrangement so that it may be swung up and out of the way effortlessly. The hydraulic fluid is pressurized using a hand-operated single-speed air hydraulic pump SPX Powerteam, model PA50. The pump relief valve was specially adjusted so that the maximum hydraulic pressure produced by the pump is 2500 psi (170 bar). It is located on the wall below the clamp. The hydraulic pump has three positions: pressurize, hold, and release. The pump should always be in the release position (pedal down) before attempting to remove or place a diaphragm, otherwise the spring return mechanism cannot leave enough space to place a new diaphragm.

Air pressure of 6 atm produces a pressure of 350 atm in the hydraulic fluid which provides an axial clamping force of 125 tons. A clamping force of 60 tons has been found sufficient to plastically deform the originally planar diaphragm between the two crimping rings, and to retain and seal it at burst pressures up to 70 atm. The crimping rings are separate stainless steel inserts so that in the event of damage, they can be removed from their respective transition section. The relative importance of the double crimp in retaining the diaphragm has not been assessed. With this system, it takes less than a minute to release the hydraulic clamping force, remove the broken diaphragm, insert a new diaphragm, and

begin the experiment.

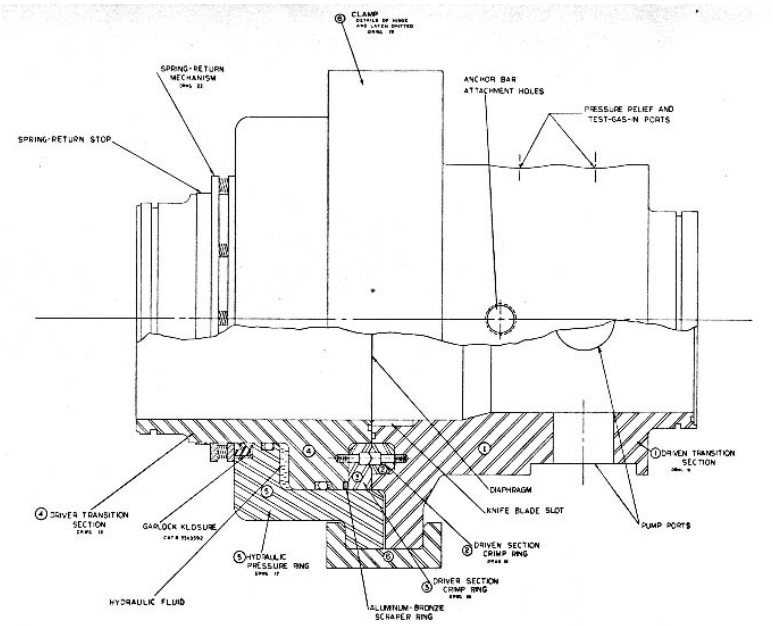

Figure 44: Diaphragm transition section.

The diaphragms need not be cut to perfectly circular shape, have holes drilled in them or be precrimped prior to their use in the shock tube. It is sufficient to cut them into roughly circular shape (27 to 28 cm diameter). Also, it is not necessary to scribe the diaphragms. A set of knife blades is mounted in the driven transition section and cuts the diaphragm as it bulges under pressure. There are two sets of knife blades. One set of blades is flat and provides a burst pressure that is roughly 50% of the free burst pressure for a given diaphragm. The other set is curved, providing a burst pressure that is roughly 80% of the free burst pressure. The burst pressures for the various diaphragm materials and thicknesses are repeatable to within 0.2 atm or less, providing very good shock Mach number repeatability. Squaring plates are also included in the driven transition section. They make the diaphragm section approximately square on the downstream side. The squaring plates eliminate loss of petals after burst and protect the walls of the driven transition section from damage by impact of the petals. No petal loss usually occurs, but occasionally small particles from the diaphragm are found at the end of the test section. These are produced by either the impact of the petals on the squaring plates or by the petals flopping back and forth past the knife blades in response to shock reflections.

A.3 Plumbing system

The 6-inch shock tube is equipped with two vacuum pumps, one for the driver section and one for the driven section. The two pumps are Welch Duo-Seal Model 1397 vacuum pumps. The driven section pump is newer than the driver section pump. The pumps are located near the wall below the diaphragm transition section. The control switch for the driver section pump is labeled *Forepump* because it can be used as a forepump for a liquid nitrogen

trapped, six-inch, oil diffusion pump. The plumbing line valves can be turned to use the forepump and the diffusion pump to evacuate the driven section to very low pressures. The driven section pump port was placed as close to the diaphragm as possible to minimize flow disturbance. The stainless steel wall material and the honed internal surface enhance the vacuum capabilities of the tube. There are no welds or bolt holes exposed to vacuum in the entire assembly. Neoprene O-rings are used for seals in all the tube joints, instrumentation ports, and ball valves used in the plumbing system.

The valves controlling the various lines are all electropneumatic valves remotely controlled by switches from the control panel. The driver section vacuum valve setup consists of a 1 in (2.54 cm) Whitey ball valve, a double acting pneumatic actuator and a MAC solenoid valve model 912B-PM-111CA. The MAC solenoid valve controls the compressed air flow into the pneumatic actuator, which in turns controls the ball valve. The driven section vacuum valve setup uses the old 1.5 in (3.81 cm) ball valve with the same components. The driven section valve setup located on the fill line is identical to the driver section vacuum valve setup. A 1/4 in (0.63 cm) plumbing line is connected to the driven section in order to measure the pressure inside the tube. The line connects to a pressure port about 10' (3 m) downstream of the diaphragm. A 1/4 in (0.63 cm) ball valve, controlled by a solenoid valve and a single-acting actuator with spring return controls the connection with the shock tube. All the solenoid valves controlling the air actuators are the same MAC model. A solenoid valve controls the driver section fill line. A schematic of the shock tube plumbing system is displayed in Fig. 45.

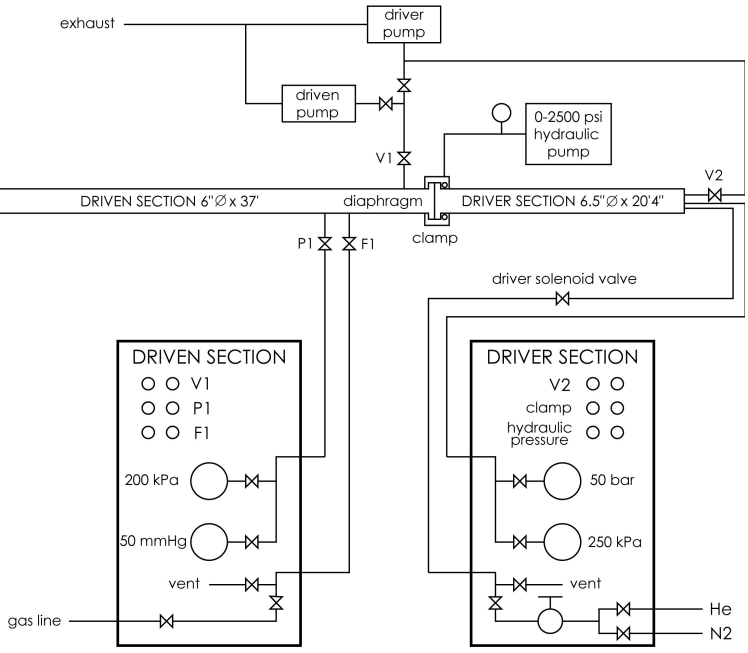

Figure 45: The 6" shock tube plumbing system

A.4 Control panel

The 6-inch shock tube control panel features control switches and feedback lights for the various valves of the tube, as well as pressure gauges connected to the driver and driven sections. Each section of the tube is connected to its corresponding control panel by two lines, one used for filling, and the other used for measuring pressure. The driver section fill line is equipped with a solenoid valve and is connected to the driver end plate. The driven section fill line connects to the tube via an electropneumatic valve labeled F1. The driven section pressure gauge line is equipped with an electropneumatic valve labeled P1. The driver section control panel has two mechanical pressure gauges: an Ashcroft Duragauge type 1377 0-250 kPa absolute pressure gauge (accuracy ±0.5%) used for preliminary filling of the tube, and a Heise model CM7992 0-50 bar high precision dial absolute pressure gauge (accuracy 0.1%). The driven section control panel is equipped with a Wallace and Tiernan model 61C1D0050 0-50 mm Hg vacuum gauge (accuracy 0.33%) and a Heise model CC130193 0-200 kPa high precision dial absolute pressure gauge. The standard connection of the gas bottles to the driver section control panel is a Matheson 9-580 400 psi regulator.

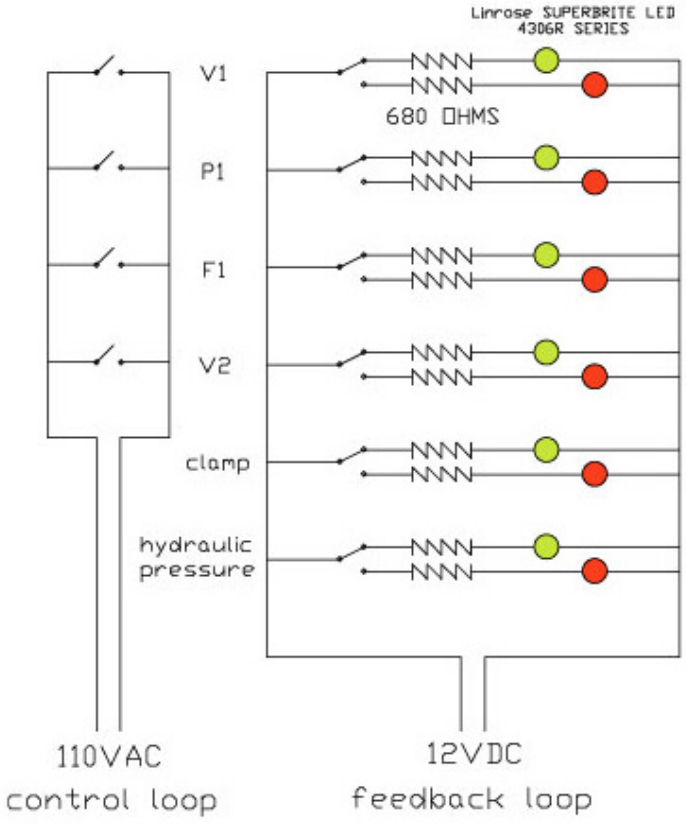

Figure 46: The 6" shock tube electrical system

The 6-inch shock tube electrical system is mounted on the back of the control panel. A schematic of the control panel electrical system is given in Fig. 46. The electropneumatic valves are powered off 110VAC using mechanical switches. The control lights for the valves are connected to mechanical switches located on the valves. The panel lights are LEDs

(Linrose 4306R series) powered with 12V using 680 ohm resistors. There are two control lights for each valve, one green corresponding to the closed or safe position, and one red corresponding to the open or unsafe position. The clamp feedback light is controlled by a mechanical switch mounted on the lower side of the clamp. The hydraulic pressure control light is powered by a pressure switch located at the outlet of the hydraulic pump. The pressure switch is a United Electric Controls model 10-B14 with a setpoint range of 180-3000 psi (1.2-20.7 MPa). Its setpoint is adjusted to a standard value of 1800 psi, so if the hydraulic pressure is higher than 1800 psi, the green feedback light will be on.

A.5 Safety interlocks

Two interlock systems are installed on the 6-in shock tube. The first safety interlock prevents the user from manually opening the clamp if the clamp is closed and the driver is pressurized. The device consists of a solenoid actuator rod that slides below the clamp handle. The solenoid is powered by a Barksdale model 96211-BB1-T1 pressure switch located on the driver end plate. The setpoint of the pressure switch is adjusted to 120 kPa. Hence when the pressure in the driver exceeds the limiting value of 120 kPa, the solenoid rod automatically slides below the clamp handle, mechanically preventing the user from opening the clamp. A flashing light located below the clamp is automatically turned on when the clamp is closed.

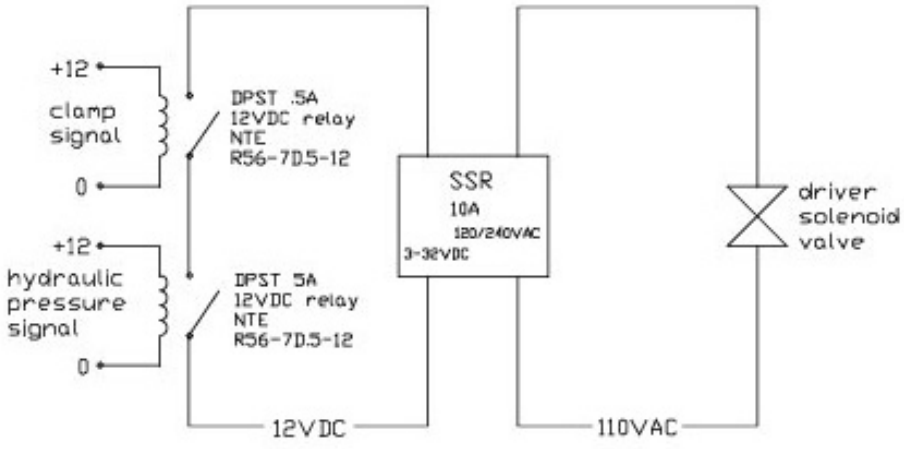

Figure 47: Driver solenoid valve interlock system

The second safety interlock controls the driver solenoid valve. Its role is to prevent the filling of the tube if it is not properly closed, i.e. the clamp is closed and pressurized. The interlock consists of an Omega solid state relay connected on one side to the driver solenoid valve and on the other to the clamp and hydraulic pressure feedback signals. The solid state relay has 3-32 VDC input and 120/240 VAC output with a nominal load current of 10 A. The clamp and hydraulic pressure signals trigger two DPST 12 VDC mechanical relays (NTE model R56-7D.5-12) that close the circuit for the solid state relay input. A schematic of the driver solenoid valve safety interlock is shown in Fig. 47.

A.6 Data acquisition

The standard data acquisition of the 6-inch shock tube consists of pressure transducers connected to a data acquisition board coupled to a PC. The pressure transducers typically used are PCB 113A21 piezoelectric transducers. The shock velocity is measured by monitoring the pressure jumps at the various pressure transducer locations. The PCB transducers are connected to a National Instruments BNC-2090 16-channel acquisition board. The acquisition board output goes into a computer equipped with a PCI-MIO-16E-1 data acquisition card. The maximum sampling rate is 1 MHz. Data acquisition is usually managed through a LabView interface on the computer. The acquisition is usually triggered by the pressure jump at the first pressure transducer downstream of the diaphragm.

A.7 Operation of the shock tube

The operation of the shock tube is fairly straightforward. Once the appropriate diaphragm is chosen, it is put in place between the driver and driven sections after opening and sliding the clamp. The driver section is then slid back against the driven section and the clamp is closed. The hydraulic pump is activated and pressurizes the clamp. The vent valves on the driver and driven section are closed while the driven and driver section pressure gauge isolation valves, the driven section fill line valve F1, and the driven section pressure gauge line P1 are opened. The vacuum pumps should already be running and vacuum is done in both sections by opening the valves V1 and V2 simultaneously in order to prevent the diaphragm from rupturing prematurely. The level of vacuum is checked on the driven section vacuum gauge. Once adequate vacuum is obtained, the Heise precision gauges should be reset to zero before closing the vacuum valves V1 and V2. After putting earphones on, the next step is to fill both sections with the desired gases, always keeping the pressure in the driver section slightly higher (10-20 kPa) than in the driven section so that the diaphragm is always bent in the same direction. This is accomplished by operating the toggle valves on the control panel, and checking simultaneously the pressure in the driven and driver sections. Once the desired pressure in the driven section is obtained, all the valves should be closed, including the driven section pressure gauge isolation valves, the driven section pressure gauge line valve P1, the driven section fill line valve F1, and the driver section 0-250 kPa pressure gauge isolation valve if the expected burst pressure is higher than the pressure gauge maximum range. All the green control lights should be on. The data acquisition is then armed on the computer. The driver section is slowly filled up until the diaphragm is pressed against the transition section blades and bursts. When the diaphragm bursts, a shock wave propagates in the driven section and triggers the acquisition. The diaphragm burst pressure should be recorded. The final step is to vent the shock tube by opening the control panel vent valves and the driven section fill line F1 if the gases used are non-toxic. A more elaborate venting system is required if toxic gases are used. The tube should always be vented before attempting to open the clamp.

B Simulation Initial Conditions and Results

Table 5: Types of focusing observed in the computational study.

Ms	D/h	Type of focusing	Comments
1.25	0.5	A	regular
	0.75	B	regular
	1.0	C	regular
	1.25	C	implosion
1.375	0.75	A	regular
	0.875	B	regular
	1.0	C	regular
1.5	0.5	A	regular
	0.75	A	regular
	0.875	B	regular
	1.0	B	regular
	1.125	C	transitional - focusing at apex
	1.25	C	transitional - focusing at apex
1.625	0.875	A	regular
	1.0	B	transitional - focusing at apex
	1.125	B	transitional - focusing at apex
	1.25	C	transitional - focusing to a line
1.75	0.875	A	regular
	1.0	B	transitional - focusing at apex
	1.125	B	transitional - focusing to a line
	1.25	B	transitional - focusing to a line
	1.375	C	transitional - focusing to a line
	1.5	C	implosion
1.875	1.0	A	transitional - focusing at apex
	1.125	B	transitional - focusing to a line
	1.25	B	transitional - focusing to a line
	1.375	C	implosion
2.0	0.5	A	regular
	1.0	A	transitional - focusing at apex
	1.125	B	transitional - focusing to a line
	1.25	B	transitional - focusing to a line
	1.375	B	implosion
	1.5	C	implosion
	1.625	C	implosion
	2.0	C	implosion

Table 6: Types of focusing observed in the computational study.

Ms	D/h	Type of focusing	Comments
2.125	1.125	A	transitional - focusing to a line
	1.25	B	transitional - focusing to a line
	1.5	B	implosion
	1.625	C	implosion
2.25	0.875	A	regular
	1.0	A	transitional - focusing at apex
	1.125	A	transitional - focusing to a line
	1.25	B	implosion
	1.375	B	implosion
	1.5	B	implosion
	1.625	B	implosion
	1.75	C	implosion
2.375	1.125	A	transitional - focusing to a line
	1.25	B	implosion
	1.5	B	implosion
	1.625	B	implosion
	1.75	B	implosion
	1.875	C	implosion
	2.0	C	implosion
2.5	0.5	A	regular
	0.875	A	regular
	1.0	A	transitional - focusing to a line
	1.125	A	transitional - focusing to a line
	1.25	B	implosion
	1.375	B	implosion
	1.5	B	implosion
	1.625	B	implosion
	1.75	C	implosion
	1.875	C	implosion
	2.0	C	implosion
2.625	1.0	A	transitional - focusing to a line
	1.125	A	transitional - focusing to a line
	1.25	B	transitional - focusing to a line
	1.375	B	implosion
	1.625	B	implosion
	1.875	B	implosion
	2.0	C	implosion
	2.25	C	implosion

Table 7: Types of focusing observed in the computational study.

Ms	D/h	Type of focusing	Comments
2.75	0.875	A	regular
	1.0	A	transitional - focusing to a line
	1.25	A	implosion
	1.375	B	implosion
	1.75	B	implosion
	1.875	B	implosion
	2.0	B	implosion
	2.125	C	implosion
	2.25	C	implosion
2.875	1.25	A	transitional - focusing to a line
	1.375	B	implosion
3.0	1.25	A	transitional - focusing to a line
	1.375	B	implosion
	2.0	B	implosion
	2.25	B	implosion

C Test Initial Conditions and Results

Table 8: Experimental results - ethylene

fuel	shot#	p_4 [bar]	p_1 [kPa]	$p_{2'}$ [kPa]	Ms	D/h	event
C_2H_4+3O_2+20%N2	069	2.0	55.4	79.4	1.17	flat	no combustion
	071	2.75	40.0	-	-	flat	direct detonation
	040	3.15	38.0	-	-	flat	direct detonation
	072	2.0	55.4	83.8	1.20	0.50	no combustion
	074	1.45	71.4	91.1	1.11	0.50	DDT
	073	2.0	55.4	93.8	1.27	1.25	DDT
	075	2.0	53.6	95.0	1.29	2.00	DDT
C_2H_4+3O_2+40%N2	058	7.6	22.0	85.0	1.89	flat	no combustion
	059	16.6	13.0	71.4	2.22	flat	DDT
	060	27.1	13.0	82.2	2.37	flat	DDT
	056	4.8	26.0	79.5	1.67	0.50	no combustion
	057	7.7	22.0	82.3	1.84	0.50	DDT
	061	16.55	13.0	72.9	2.24	0.50	DDT
	044	1.45	73.0	86.5	1.08	1.25	no combustion
	043	2.1	55.4	98.7	1.30	1.25	deflagration outside reflector
	042	3.2	38.0	90.3	1.48	1.25	deflagration outside reflector
	041	4.1	26.0	79.5	1.67	1.25	detonation inside reflector
	023	2.1	55.4	87.9	1.23	2.00	no combustion
	021	3.15	38.0	89.1	1.47	2.00	deflagration outside reflector
	024	4.5	26.0	80.7	1.68	2.00	detonation inside reflector
C_2H_4+3O_2+60%N2	066	7.7	22.0	88.2	1.90	flat	no combustion
	067bis	17.4	13.0	73.7	2.25	flat	DDT
	068bis	26.8	13.0	81.6	2.36	flat	deflagration outside reflector
	063	4.75	26.0	76.1	1.63	0.50	no combustion
	062	7.75	22.0	85.3	1.87	0.50	deflagration outside reflector
	065	17.1	13.0	73.7	2.25	0.50	DDT
	064	26.8	13.0	83.3	2.38	0.50	DDT
	048	1.5	73.0	87.2	1.08	1.25	no combustion
	138	2.0	55.4	96.8	1.28	1.25	deflagration outside reflector
	046	4.7	26.0	77.2	1.64	1.25	deflagration outside reflector
	045	7.7	22.0	83.9	1.85	1.25	detonation inside reflector
	031	2.05	55.4	86.1	1.22	2.00	no combustion
	030	3.15	38.0	87.6	1.46	2.00	deflagration outside reflector
	028	4.65	26.0	82.0	1.69	2.00	deflagration outside reflector
	029	7.7	22.0	82.6	1.84	2.00	detonation inside reflector

Table 9: Experimental results - ethylene

fuel	shot#	p_4 [bar]	p_1 [kPa]	$p_{2'}$ [kPa]	Ms	D/h	event
C_2H_4+3O_2+74%N2	081	7.7	22.0	83.7	1.85	flat	no combustion
	079	17.7	13.0	73.8	2.24	flat	DDT
	080	27.0	13.0	83.5	2.38	flat	DDT
	076	7.65	22.0	83.7	1.85	0.50	no combustion
	077	17.3	13.0	72.4	2.22	0.50	deflagration outside reflector
	078	27.15	13.0	81.7	2.36	0.50	DDT
	053	1.95	55.4	89.3	1.24	1.25	no combustion
	054	3.15	38.0	89.4	1.47	1.25	deflagration outside reflector
	055	4.75	26.0	78.0	1.65	1.25	deflagration outside reflector
	049	14.85	16.0	79.3	2.10	1.25	deflagration outside reflector
	050	17.0	13.0	72.4	2.22	1.25	deflagration outside reflector
	051	26.9	13.0	83.5	2.38	1.25	detonation inside reflector
	037	2.0	55.4	84.2	1.20	2.00	no combustion
	036	3.1	38.0	88.2	1.46	2.00	deflagration outside reflector
	035	4.7	26.0	79.2	1.66	2.00	deflagration outside reflector
	032	7.65	22.0	83.7	1.85	2.00	deflagration outside reflector
	033	9.4	17.0	75.5	1.99	2.00	deflagration outside reflector
	034	14.65	17.0	84.3	2.10	2.00	deflagration outside reflector
	082	17.45	13.0	72.4	2.22	2.00	deflagration outside reflector
	052	27.1	13.0	83.5	2.38	2.00	detonation inside reflector

Table 10: Experimental results - propane

fuel	shot#	p_4 [bar]	p_1 [kPa]	$p_{2'}$ [kPa]	Ms	D/h	event
C_3H_8+5O_2+40%N2	089	7.65	22.0	87.7	1.90	0.50	no combustion
	090	16.0	13.0	74.5	2.27	0.50	deflagration outside reflector
	091	26.6	13.0	83.6	2.40	0.50	deflagration outside reflector
	085	1.45	73.0	84.2	1.07	1.25	no combustion
	084	1.65	65.0	99.7	1.21	1.25	deflagration outside reflector
	083	1.95	55.4	100.3	1.31	1.25	deflagration outside reflector
	088	2.95	38.0	89.6	1.48	1.25	deflagration outside reflector
	086	4.6	26.0	83.7	1.72	1.25	DDT
	087	7.6	22.0	86.3	1.89	1.25	detonation inside reflector
C_3H_8+5O_2+60%N2	092	7.7	22.0	88.4	1.90	0.50	no combustion
	094	16.65	13.0	77.1	2.30	0.50	deflagration outside reflector
	093	26.8	13.0	85.1	2.41	0.50	deflagration outside reflector
	096	1.95	55.4	98.8	1.30	1.25	deflagration outside reflector
	095	2.8	40.0	90.8	1.45	1.25	deflagration outside reflector
	097	7.75	22.0	88.4	1.90	1.25	deflagration outside reflector
	098	17.3	13.0	77.1	2.30	1.25	DDT
	099	26.8	13.0	85.1	2.41	1.25	detonation inside reflector
C_3H_8+5O_2+76%N2	103	7.65	22.0	85.0	1.86	0.50	no combustion
	101	2.8	40.0	85.3	1.41	1.25	no combustion
	104	3.1	38.0	86.5	1.45	1.25	no combustion
	102	4.8	26.0	80.6	1.68	1.25	deflagration outside reflector
	100	27.1	13.0	84.4	2.40	1.25	deflagration outside reflector

Table 11: Experimental results - hydrogen

fuel	shot#	p_4 [bar]	p_1 [kPa]	$p_{2'}$ [kPa]	Ms	D/h	event
$2H_2+O_2$+20%N2	126	3.0	38.0	79.3	1.39	0.50	no combustion
	124	4.75	26.0	64.1	1.50	0.50	deflagration outside reflector
	125	7.7	22.0	69.2	1.68	0.50	DDT
	127	8.5	17.0	100.7	2.28	0.50	direct defl.; det. inside reflector
	128	15.7	16.0	100.4	2.35	0.50	direct defl.; det. inside reflector
	122	1.45	73.0	95.9	1.13	1.25	deflagration outside reflector
	123	1.95	55.4	85.1	1.21	1.25	deflagration outside reflector
	120	2.95	38.0	75.2	1.36	1.25	detonation inside reflector
	121	4.75	26.0	68.0	1.54	1.25	detonation inside reflector
$2H_2+O_2$+40%N2	116	3.0	38.0	82.0	1.41	0.50	no combustion
	115	4.45	26.0	69.0	1.55	0.50	deflagration outside reflector
	114	7.7	22.0	73.2	1.73	0.50	DDT
	129	15.9	16.0	70.0	1.97	0.50	DDT
	130	16.5	13.0	60.9	2.04	0.50	DDT
	131	26.8	13.0	66.9	2.13	0.50	detonation inside reflector
	119	1.65	55.4	84.9	1.21	1.25	deflagration outside reflector
	118	3.15	38.0	82.0	1.41	1.25	deflagration outside reflector
	117	4.7	26.0	74.2	1.61	1.25	detonation inside reflector
$2H_2+O_2$+56%N2	112	1.95	55.4	92.3	1.25	0.50	no combustion
	113	2.9	38.0	82.7	1.42	0.50	no combustion
	110	4.7	26.0	73.6	1.60	0.50	deflagration outside reflector
	111	7.65	22.0	76.0	1.76	0.50	deflagration outside reflector
	134	9.0	17.0	66.0	1.86	0.50	deflagration outside reflector
	135	15.9	16.0	74.8	2.04	0.50	DDT
	133	16.1	13.0	63.5	2.08	0.50	DDT
	132	26.7	13.0	71.1	2.20	0.50	detonation inside reflector
	109	1.45	73.0	81.9	1.05	1.25	no combustion
	108	1.7	65.0	96.9	1.19	1.25	deflagration outside reflector
	107	1.95	55.4	92.3	1.25	1.25	deflagration outside reflector
	105	3.05	38.0	80.1	1.40	1.25	deflagration outside reflector
	106	7.65	22.0	76.0	1.76	1.25	deflagration outside reflector
	137	8.9	17.0	64.7	1.84	1.25	deflagration outside reflector
	136	15.7	16.0	74.8	2.04	1.25	detonation inside reflector

D Pressure-Time and Space-Time Diagrams

This section provides pressure-time (P–t) graphs and space-time (x–t) diagrams for each test (shot). These plots were constructed by analyzing the piezo-electric pressure transducer and ion-probe signals. Important points to note are:

1 The scale of negative values of y-axis is ten times bigger then that of the positive values in every diagram - it is not shown on some diagrams.

2 In some diagrams the signals from ion probes are not shown due to poor data, although combustion was observed.

3 The filled squares representing the signals from ion probes in the diagrams indicate very accurate data; The open squares represents data of poorer quality.

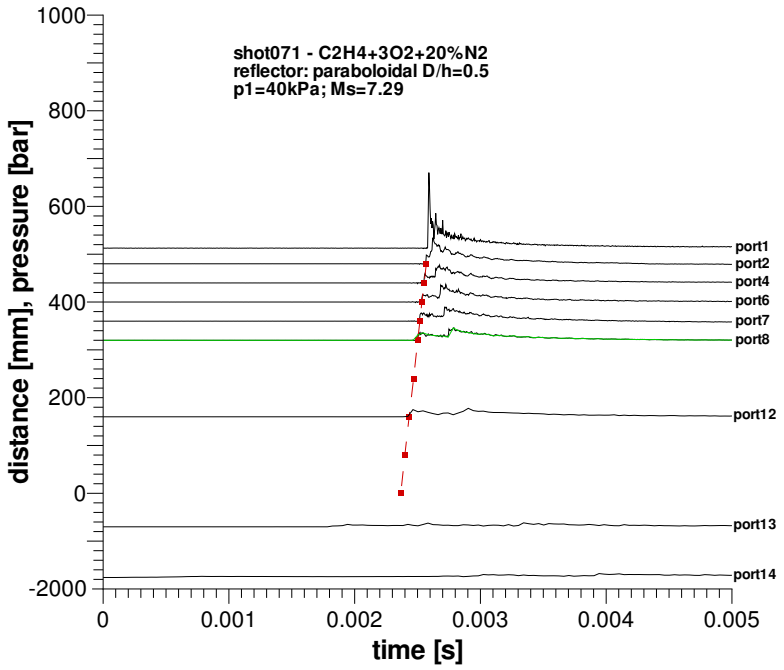

Figure 48: Direct initiation of detonation (shot 071); test mixture: C_2H_4+$3O_2$+20%N_2; incident shock wave Mach number: $M_s = 1.41$;

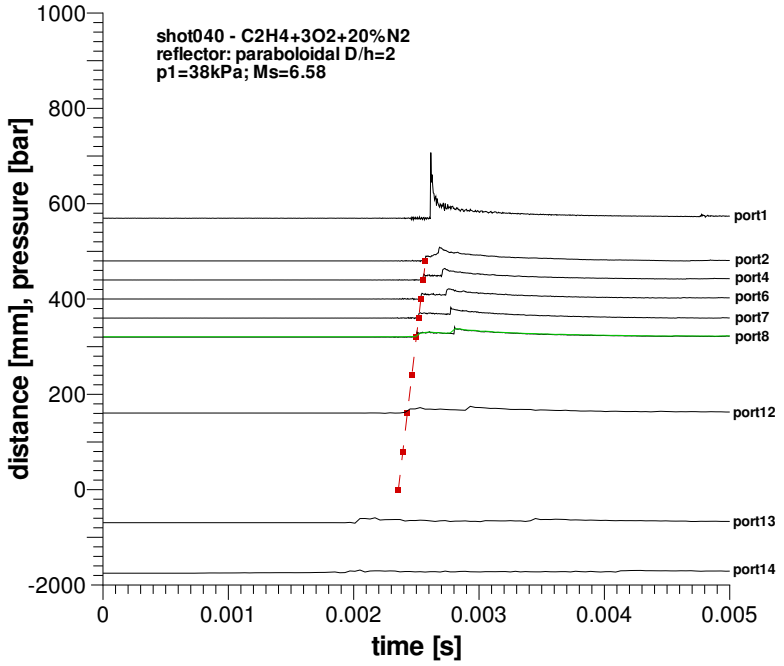

Figure 49: Direct initiation of detonation (shot 040); test mixture: C_2H_4+$3O_2$+20%N_2; incident shock wave Mach number: $M_s = 1.47$.

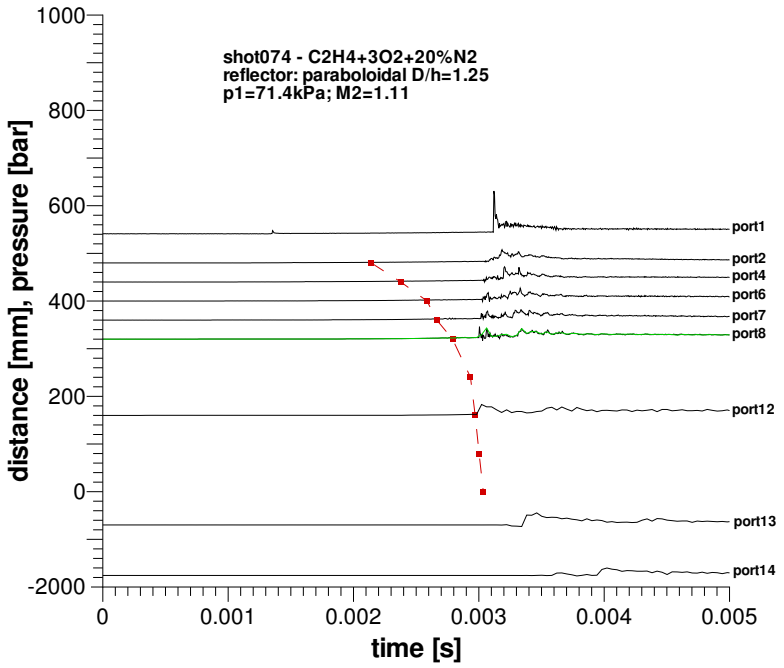

Figure 50: Deflagration-to-detonation transition DDT (shot 074); test mixture: C_2H_4+3O_2+20%N_2; incident shock wave Mach number: $M_s = 1.11$; reflector: $D/h = 1.25$.

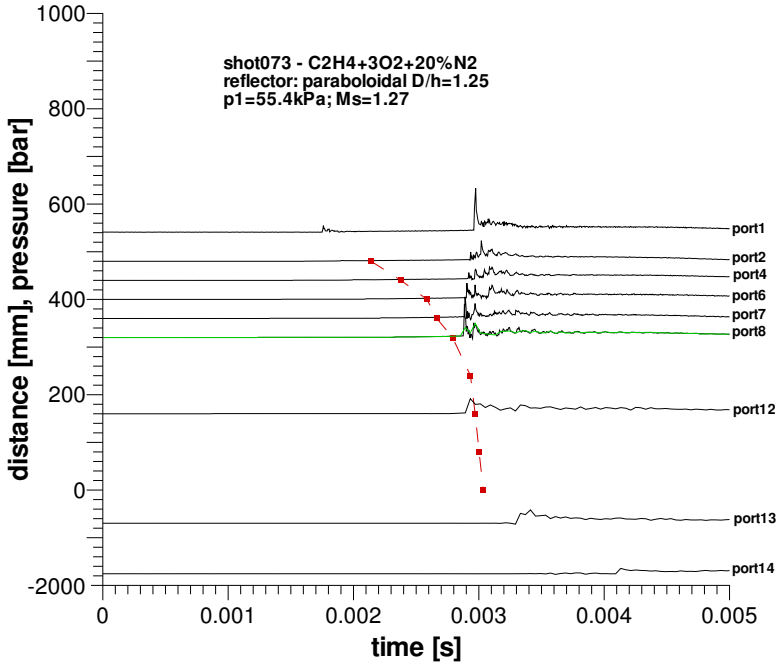

Figure 51: Deflagration-to-detonation transition DDT (shot 073); test mixture: C_2H_4+3O_2+20%N_2; incident shock wave Mach number: $M_s = 1.27$.

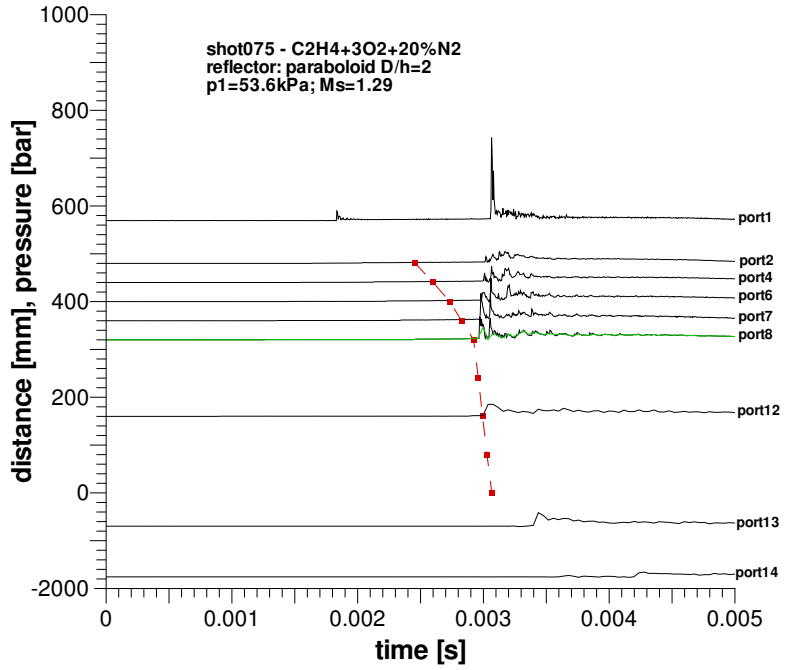

Figure 52: Deflagration-to-detonation transition DDT (shot 075); test mixture: C_2H_4+3O_2+20%N_2; incident shock wave Mach number: $M_s = 1.29$.

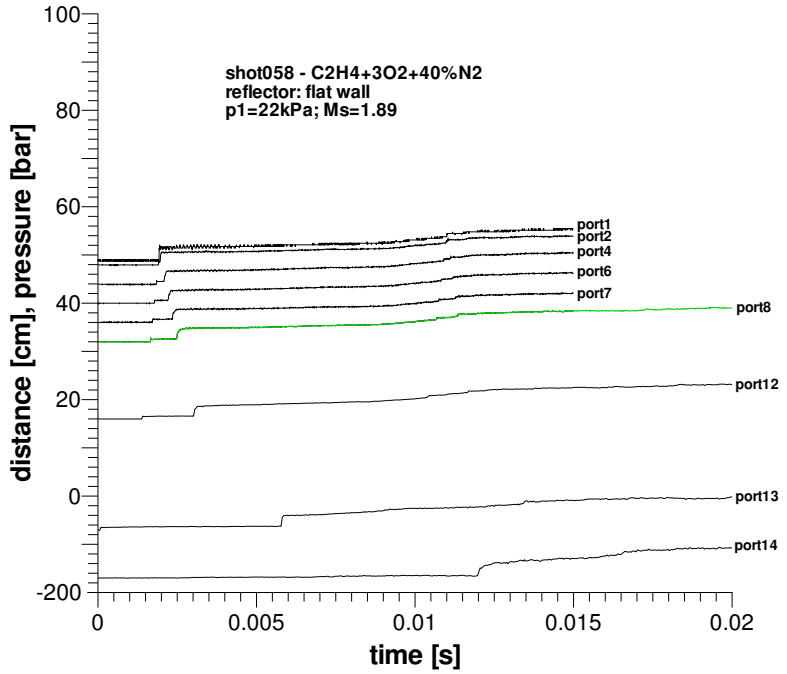

Figure 53: No combustion (shot 058); test mixture: C_2H_4+3O_2+40%N_2; incident shock Mach number: $M_s = 1.89$.

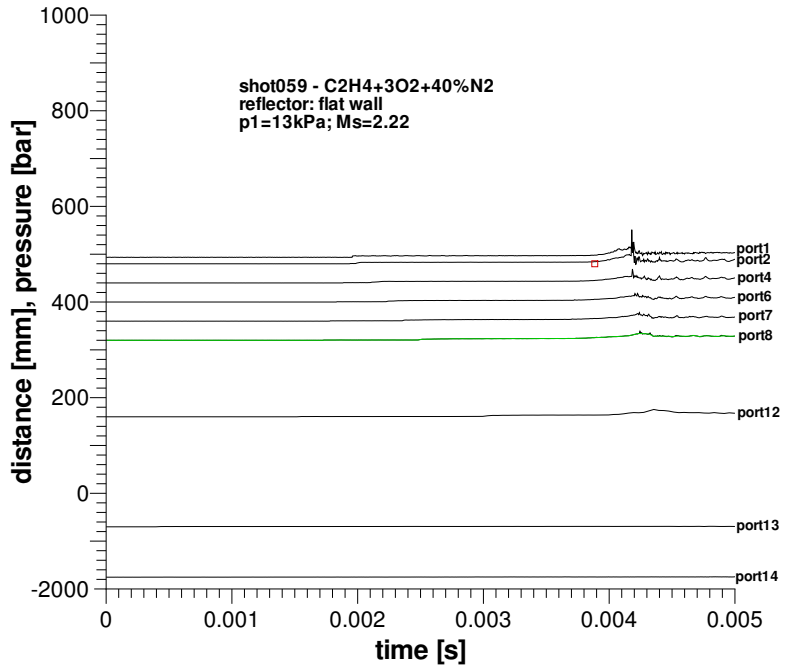

Figure 54: Deflagration-to-detonation transition DDT (shot 059); test mixture: C_2H_4+3O_2+40%N_2; incident shock wave Mach number: $M_s = 2.22$.

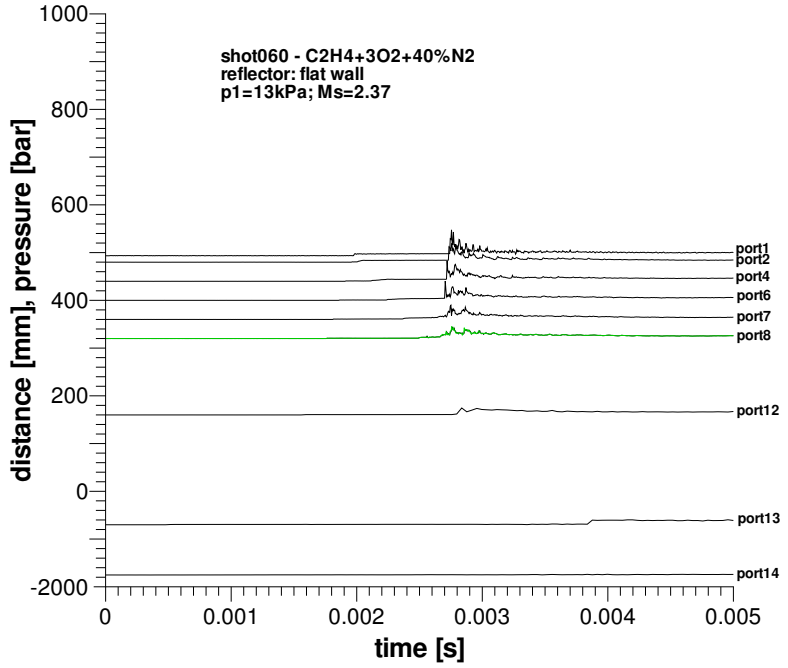

Figure 55: Deflagration-to-detonation transition DDT (shot 060); test mixture: C_2H_4+3O_2+40%N_2; incident shock wave Mach number: $M_s = 2.37$.

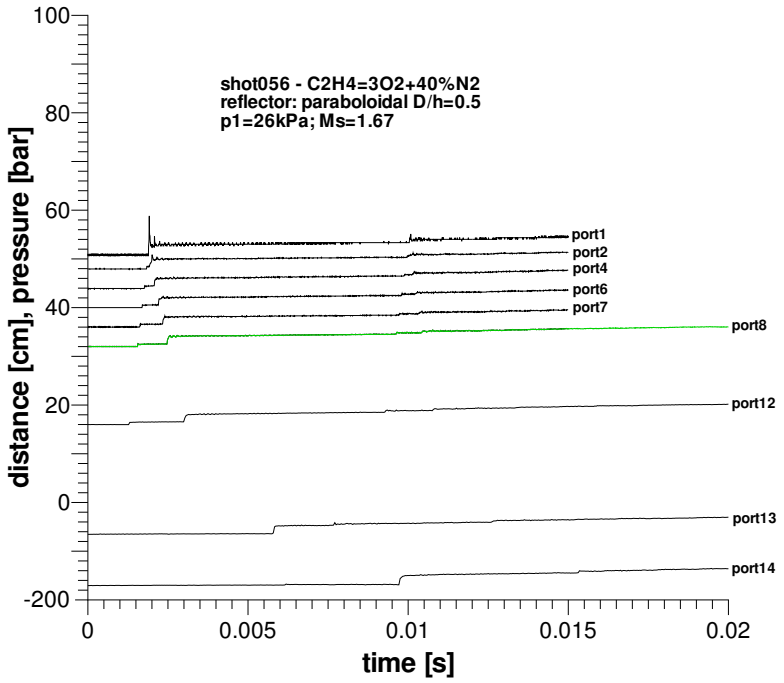

Figure 56: No combustion (shot 056); test mixture: C_2H_4+3O_2+40%N_2; incident shock Mach number: $M_s = 1.67$.

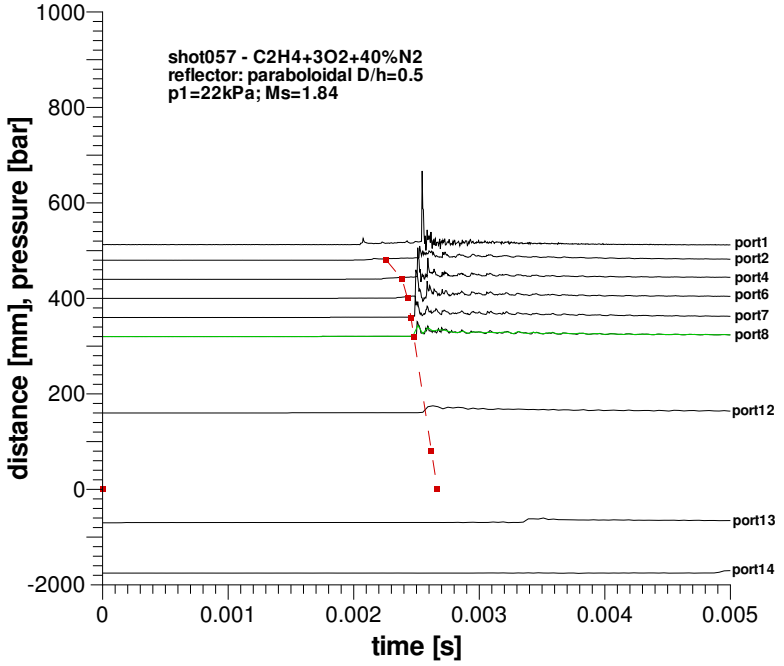

Figure 57: Deflagration-to-detonation transition DDT (shot 057); test mixture: C_2H_4+3O_2+40%N_2; incident shock wave Mach number: $M_s = 1.84$.

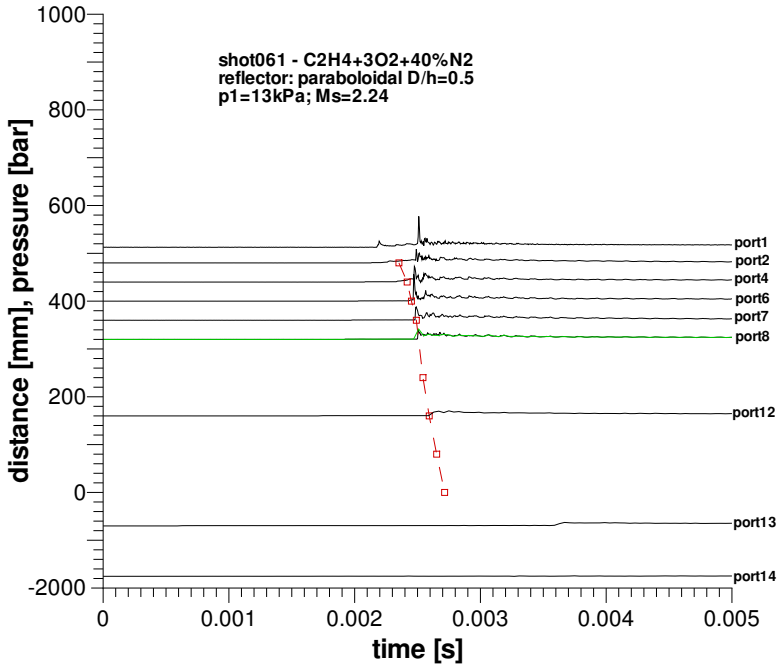

Figure 58: Deflagration-to-detonation transition DDT (shot 061); test mixture: C_2H_4+3O_2+40%N_2; incident shock wave Mach number: $M_s = 2.24$.

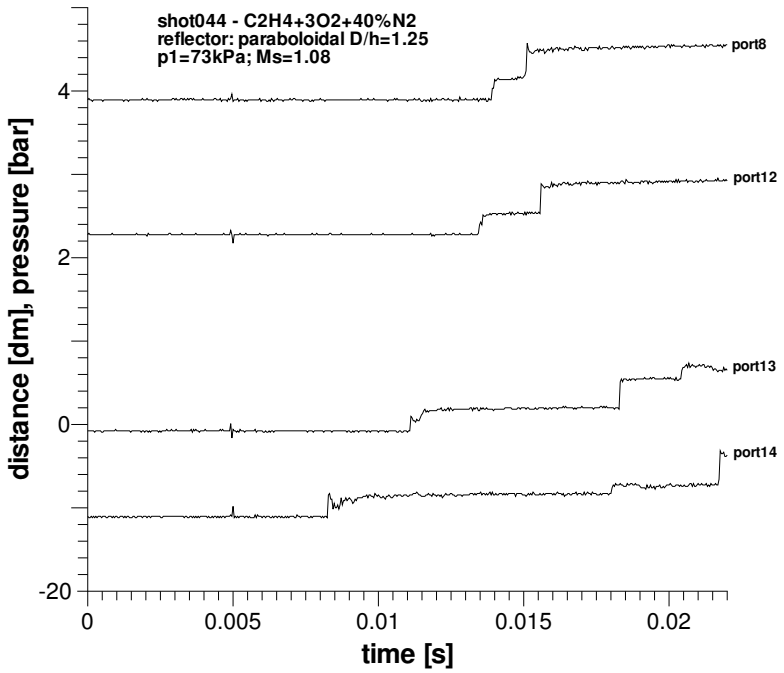

Figure 59: No combustion (shot 044); test mixture: C_2H_4+3O_2+40%N_2; incident shock Mach number: $M_s = 1.08$.

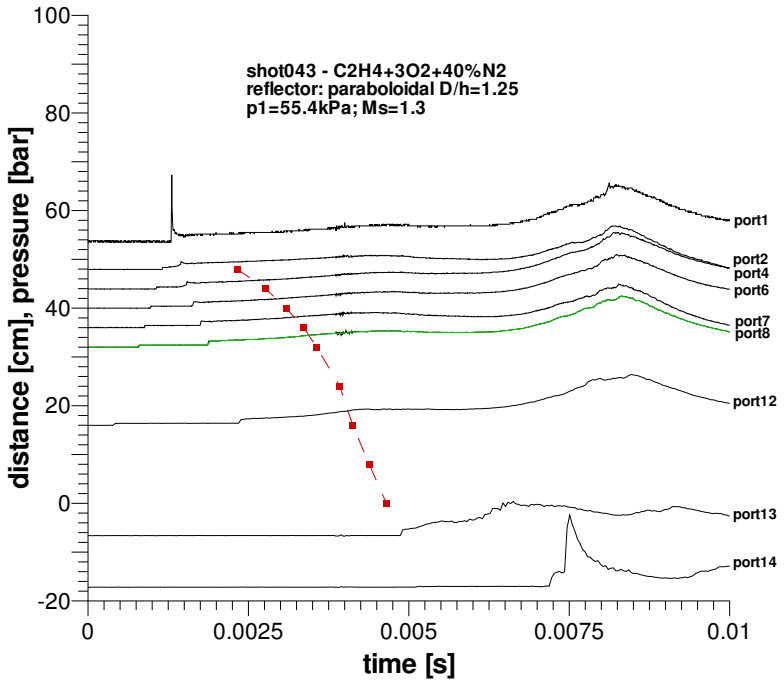

Figure 60: Deflagration outside reflector (shot 043); test mixture: C_2H_4+3O_2+40%N_2; incident shock Mach number: $M_s = 1.30$.

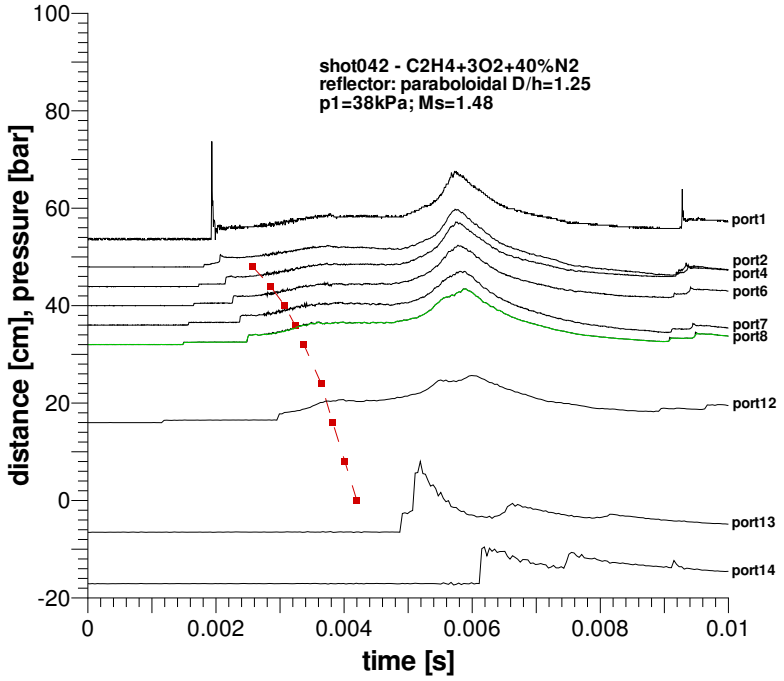

Figure 61: Deflagration outside reflector (shot 042); test mixture: C_2H_4+3O_2+40%N_2; incident shock Mach number: $M_s = 1.48$.

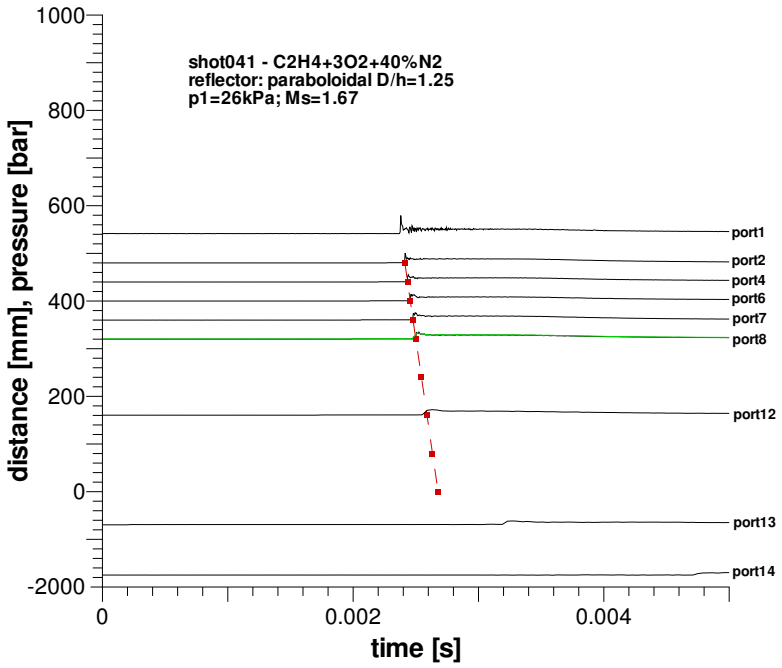

Figure 62: Detonation inside reflector (shot 041); test mixture: C_2H_4+3O_2+40%N_2; incident shock Mach number: $M_s = 1.67$.

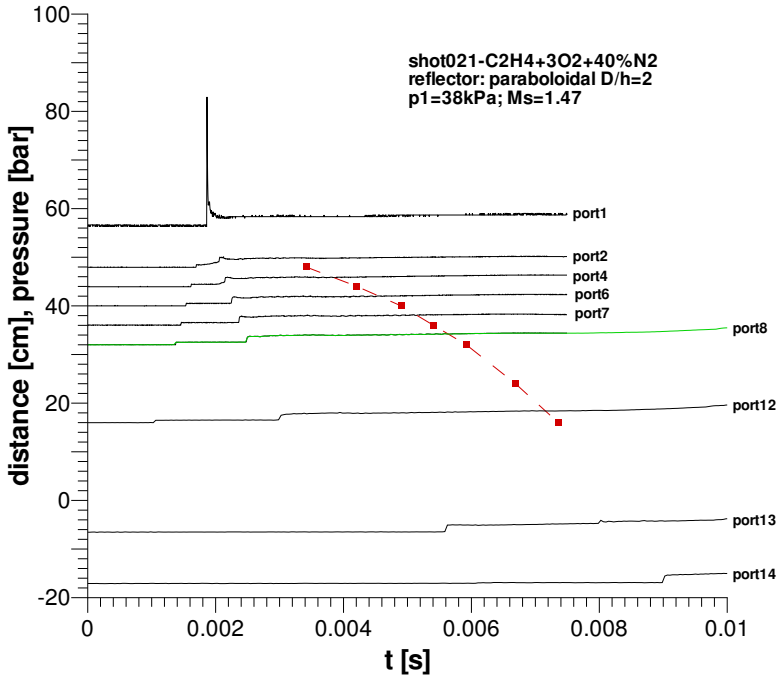

Figure 63: Deflagration outside reflector (shot 021); test mixture: C_2H_4+3O_2+40%N_2; incident shock Mach number: $M_s = 1.47$.

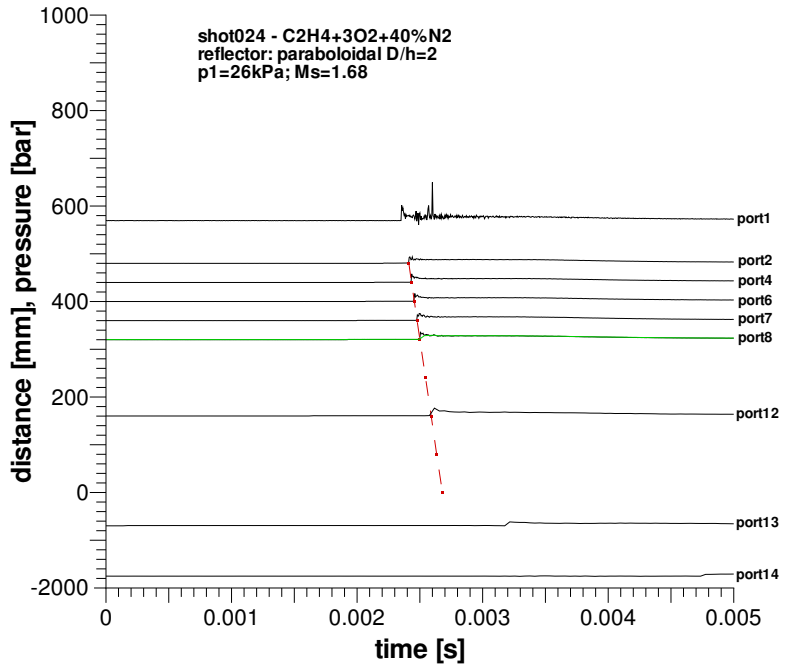

Figure 64: Detonation inside reflector (shot 024); test mixture: C_2H_4+$3O_2$+40%N_2; incident shock Mach number: $M_s = 1.1.68$.

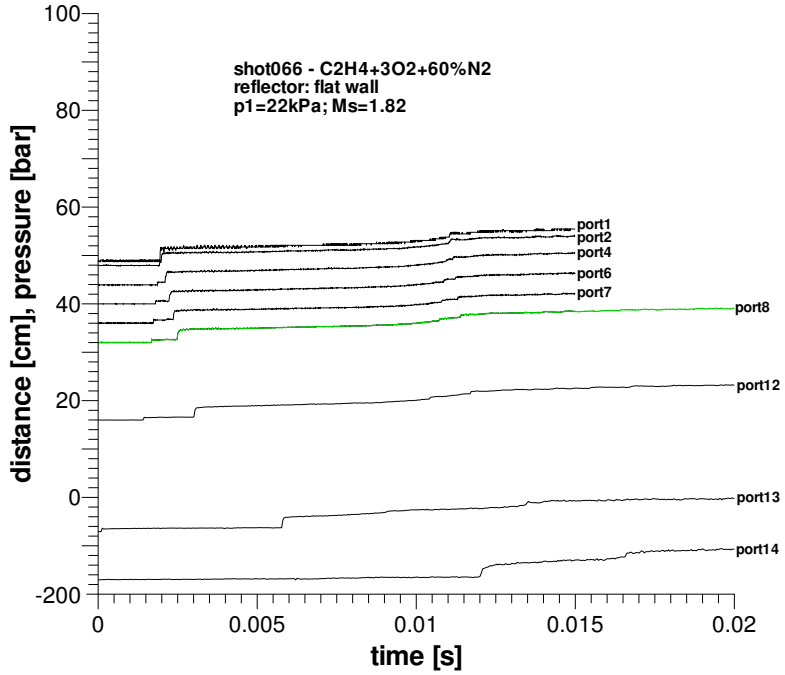

Figure 65: No combustion (shot 066); test mixture: C_2H_4+$3O_2$+60%N_2; incident shock Mach number: $M_s = 1.90$.

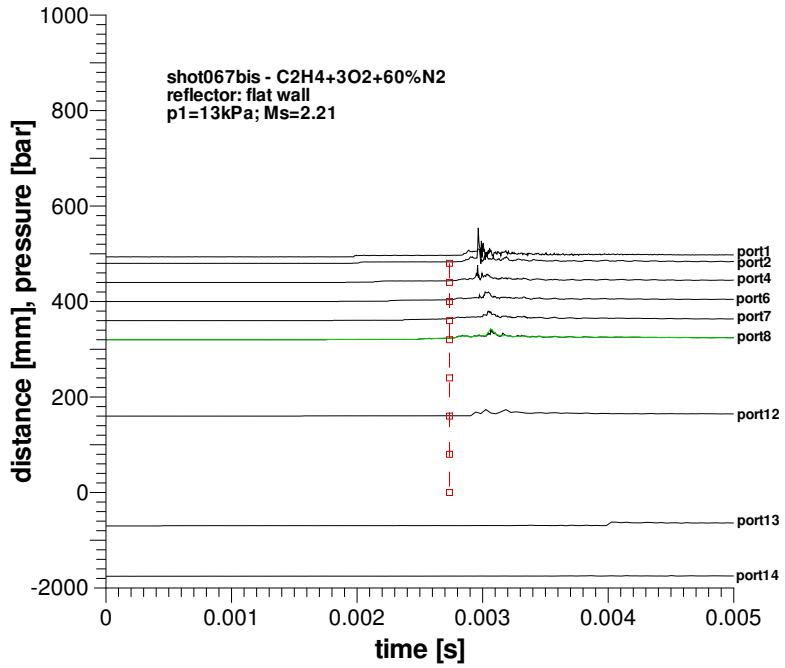

Figure 66: Deflagration-to-detonation transition DDT (shot 067bis); test mixture: C_2H_4+$3O_2$+60%N_2; incident shock wave Mach number: $M_s = 2.25$.

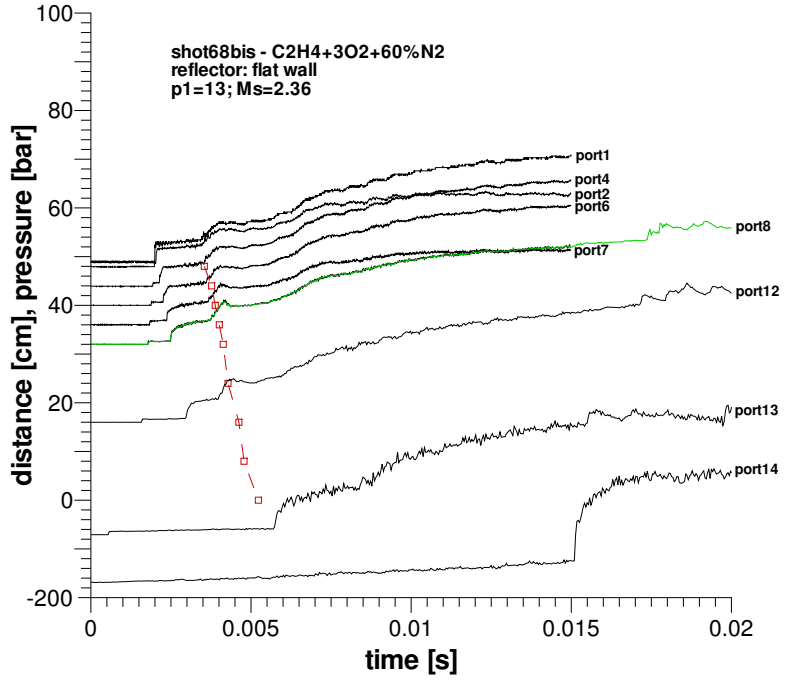

Figure 67: Deflagration outside reflector (shot 068bis); test mixture: C_2H_4+$3O_2$+60%N_2; incident shock Mach number: $M_s = 2.36$.

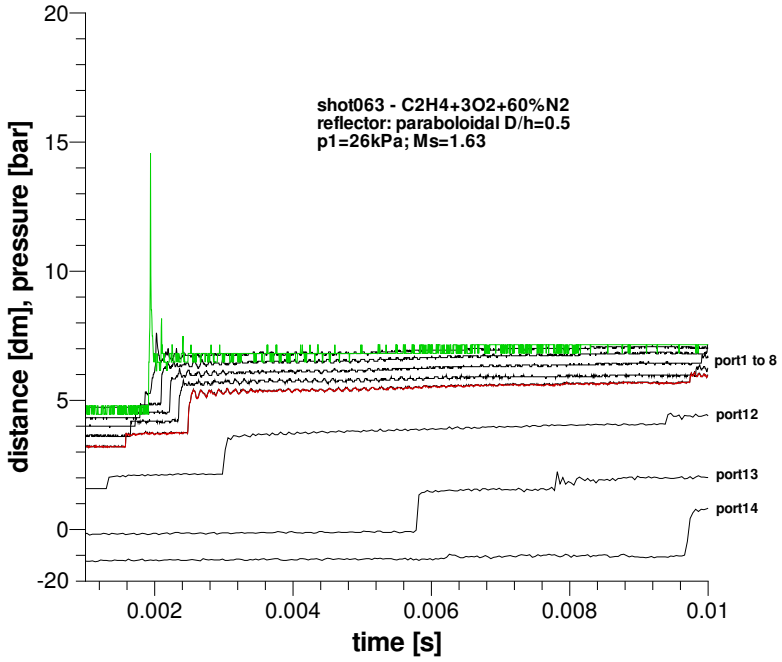

Figure 68: No combustion (shot 063); test mixture: C_2H_4+3O_2+60%N_2; incident shock Mach number: $M_s = 1.63$.

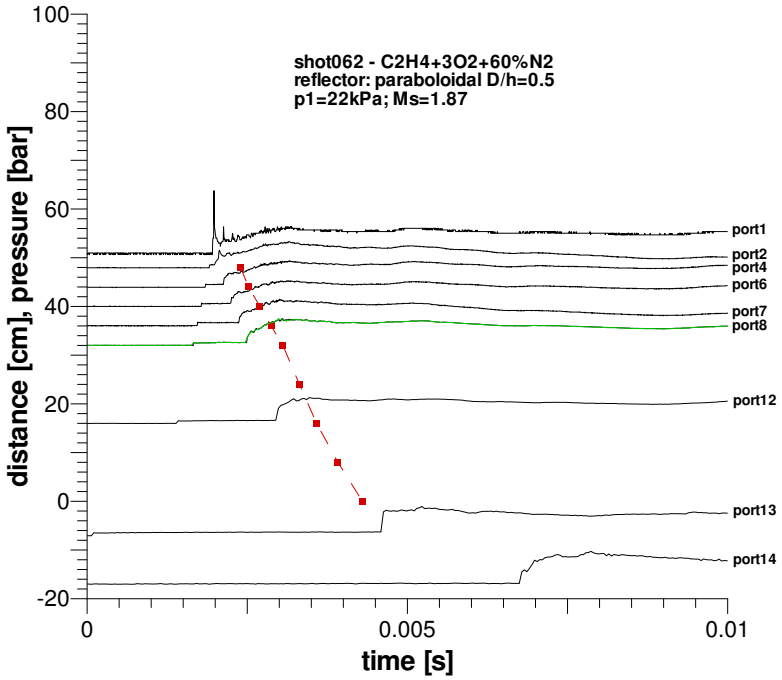

Figure 69: Deflagration outside reflector (shot 062); test mixture: C_2H_4+3O_2+60%N_2; incident shock Mach number: $M_s = 1.87$.

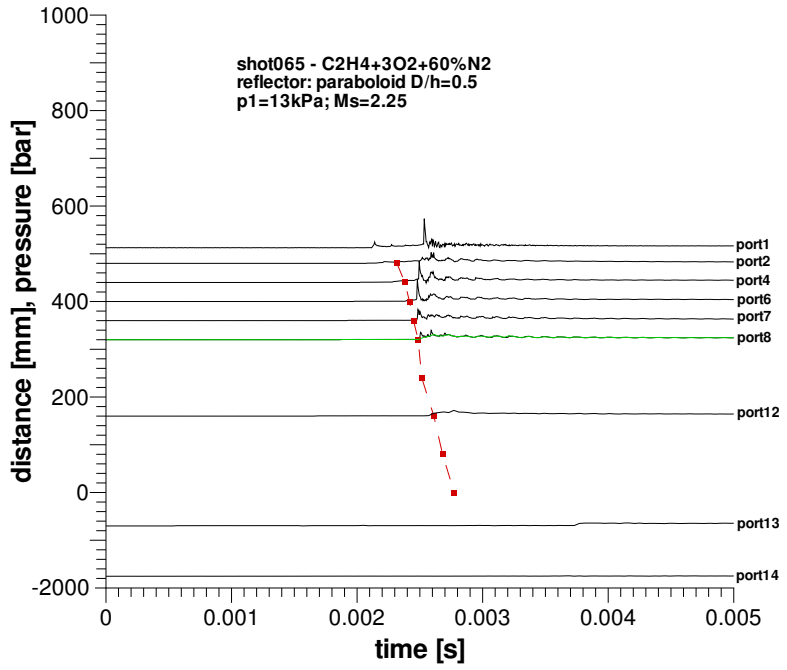

Figure 70: Deflagration-to-detonation transition DDT (shot 065); test mixture: C_2H_4+3O_2+60%N_2; incident shock wave Mach number: $M_s = 2.25$.

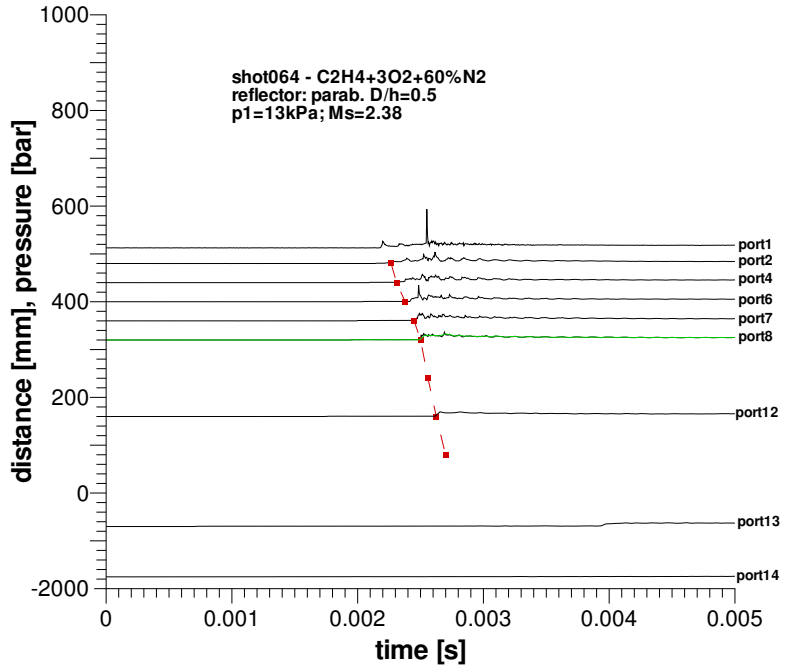

Figure 71: Deflagration-to-detonation transition DDT (shot 064); test mixture: C_2H_4+3O_2+60%N_2; incident shock wave Mach number: $M_s = 2.38$.

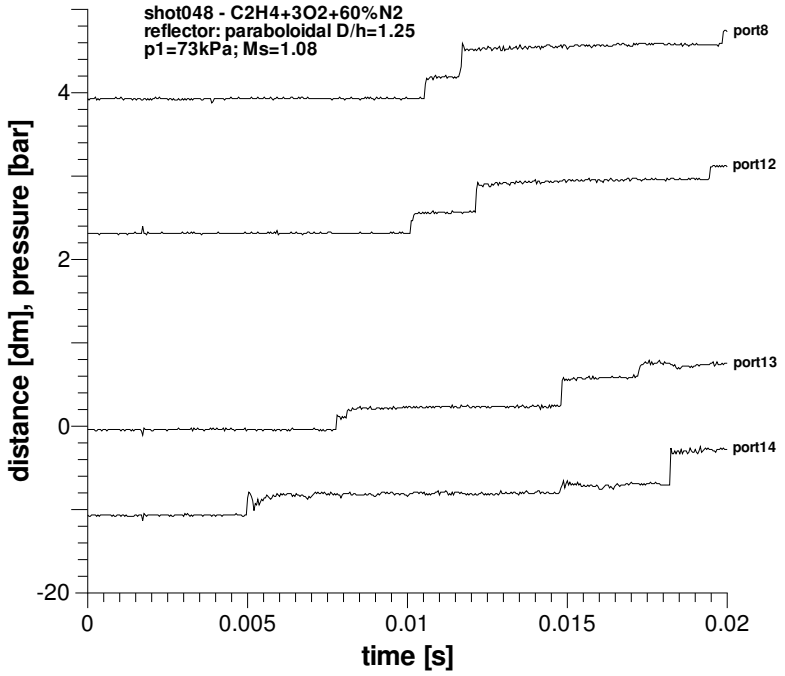

Figure 72: No combustion (shot 048); test mixture: C_2H_4+$3O_2$+60%N_2; incident shock Mach number: $M_s = 1.08$.

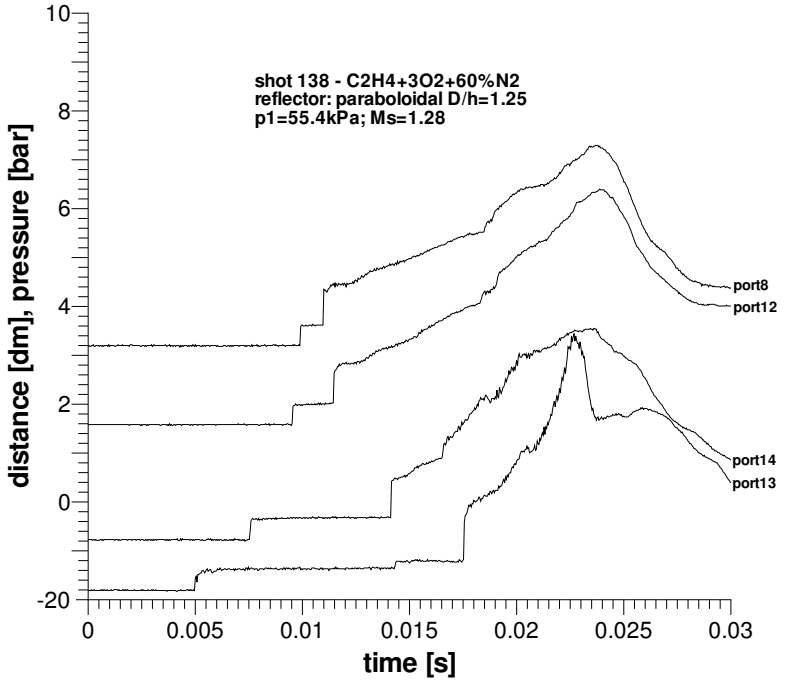

Figure 73: Deflagration outside reflector (shot 138); test mixture: C_2H_4+$3O_2$+60%N_2; incident shock Mach number: $M_s = 1.28$.

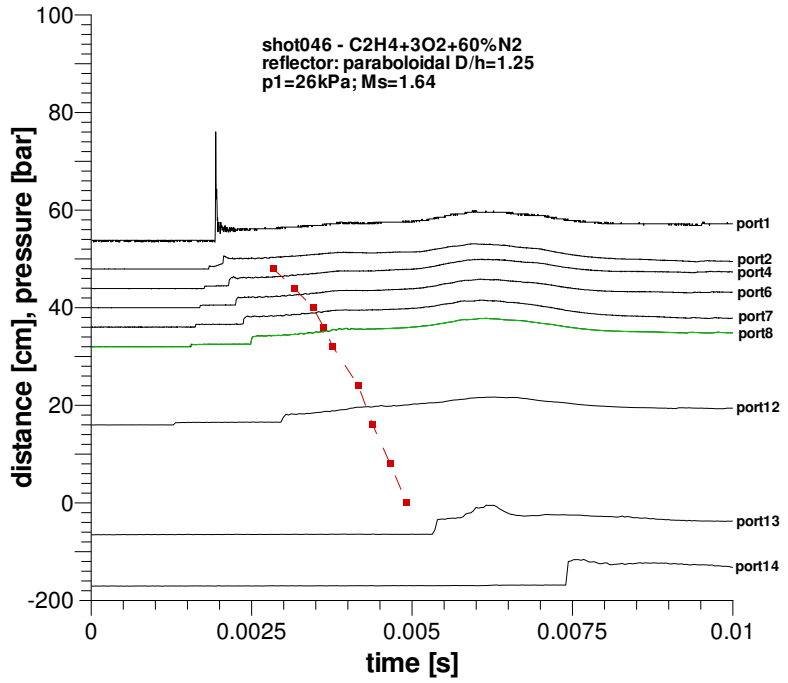

Figure 74: Deflagration outside reflector (shot 046); test mixture: C_2H_4+3O_2+60%N_2; incident shock Mach number: $M_s = 1.64$.

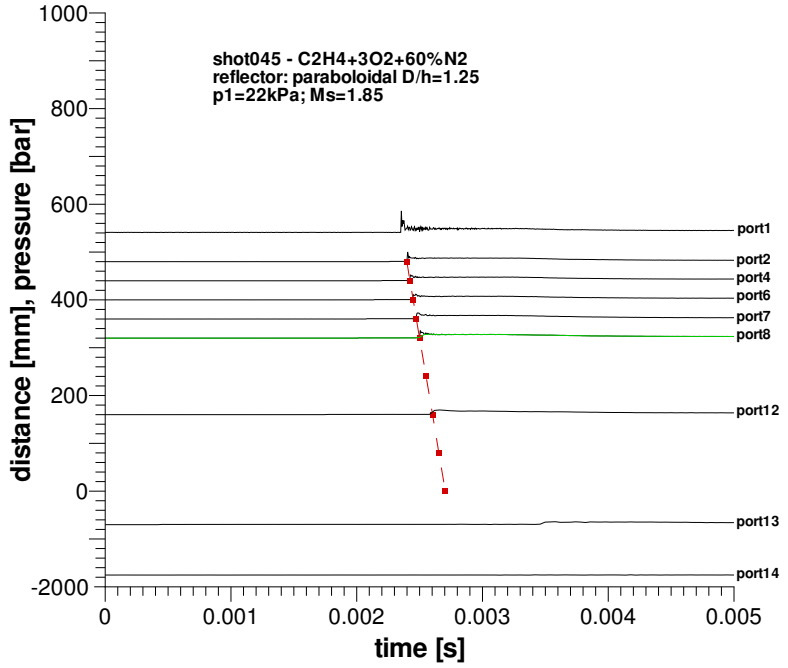

Figure 75: Detonation inside reflector (shot 045); test mixture: C_2H_4+3O_2+60%N_2; incident shock Mach number: $M_s = 1.85$.

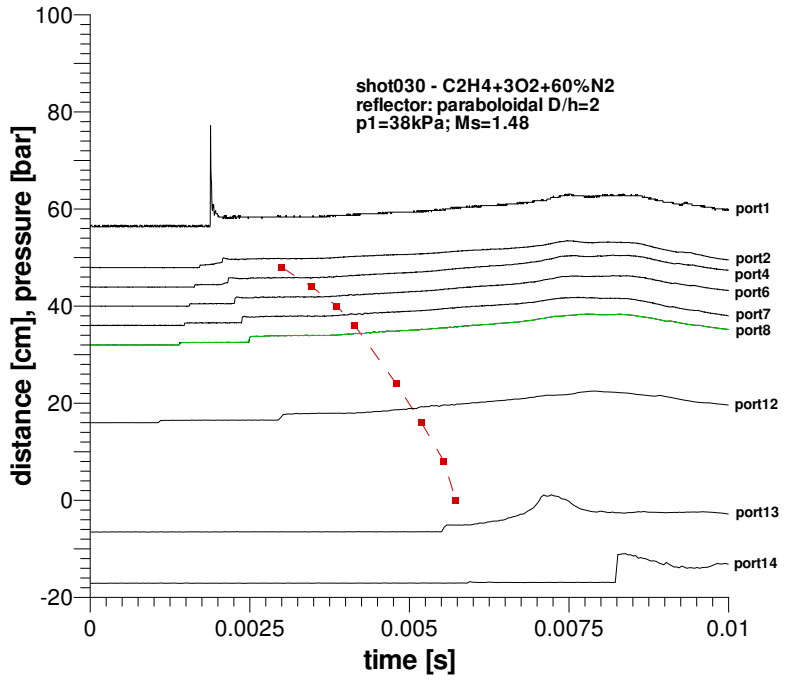

Figure 76: Deflagration outside reflector (shot 030); test mixture: C_2H_4+3O_2+60%N_2; incident shock Mach number: $M_s = 1.46$.

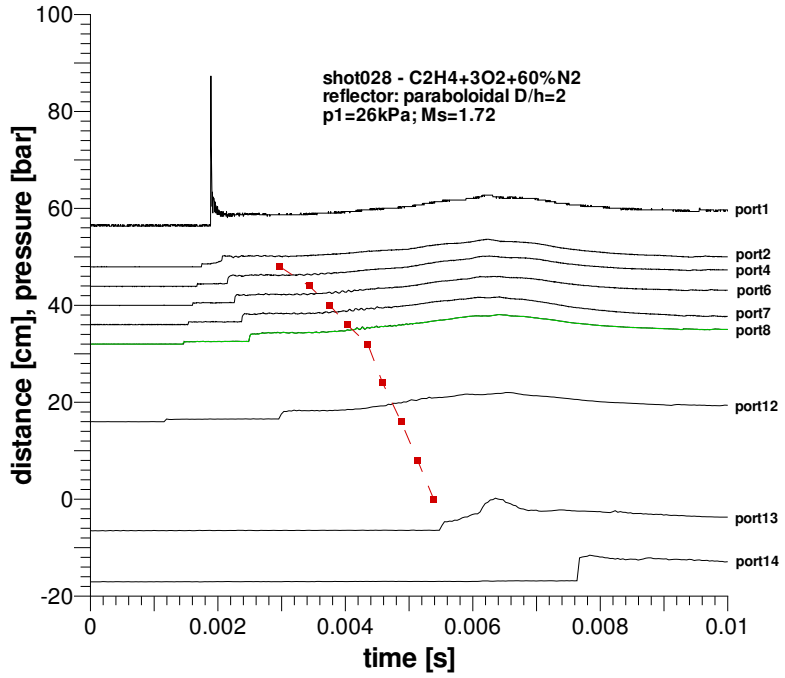

Figure 77: Deflagration outside reflector (shot 028); test mixture: C_2H_4+3O_2+60%N_2; incident shock Mach number: $M_s = 1.69$.

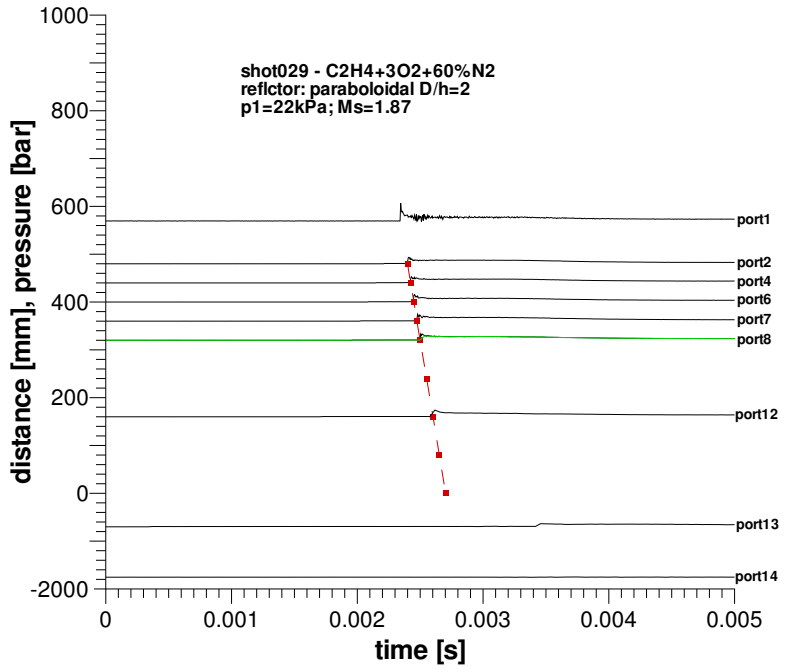

Figure 78: Detonation inside reflector (shot 029); test mixture: C_2H_4+3O_2+60%N_2; incident shock Mach number: $M_s = 1.84$.

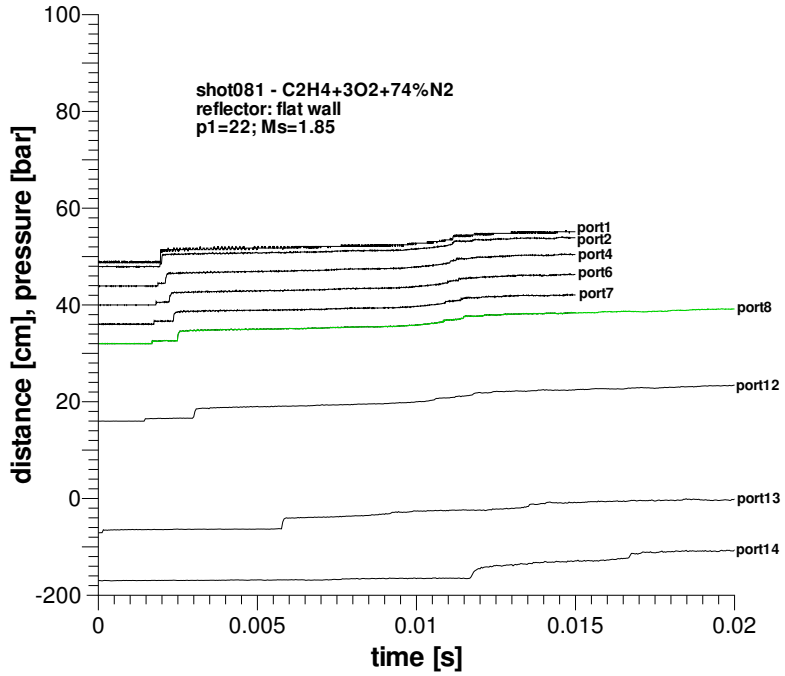

Figure 79: No combustion (shot 081); test mixture: C_2H_4+3O_2+74%N_2; incident shock Mach number: $M_s = 1.85$.

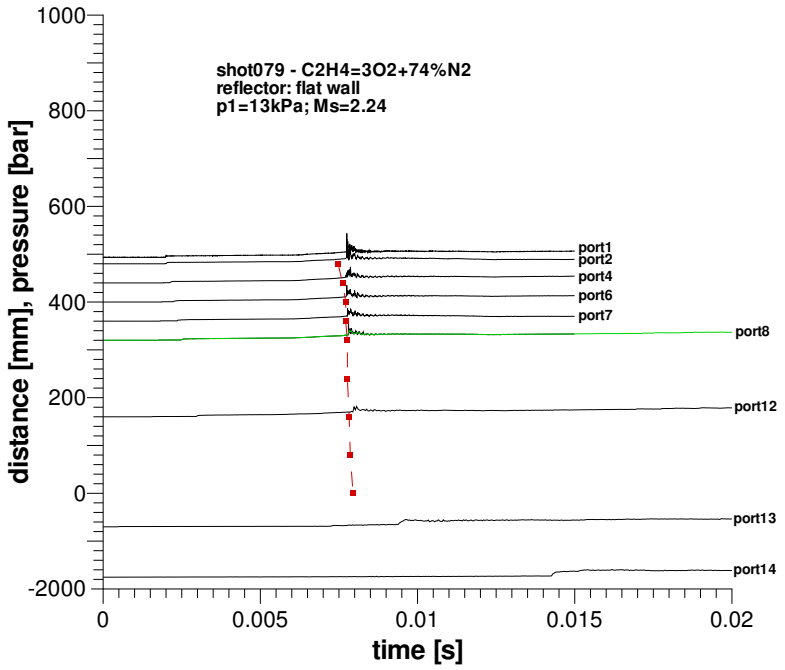

Figure 80: Deflagration-to-detonation transition DDT (shot 079); test mixture: C_2H_4+3O_2+74%N_2; incident shock wave Mach number: $M_s = 2.29$.

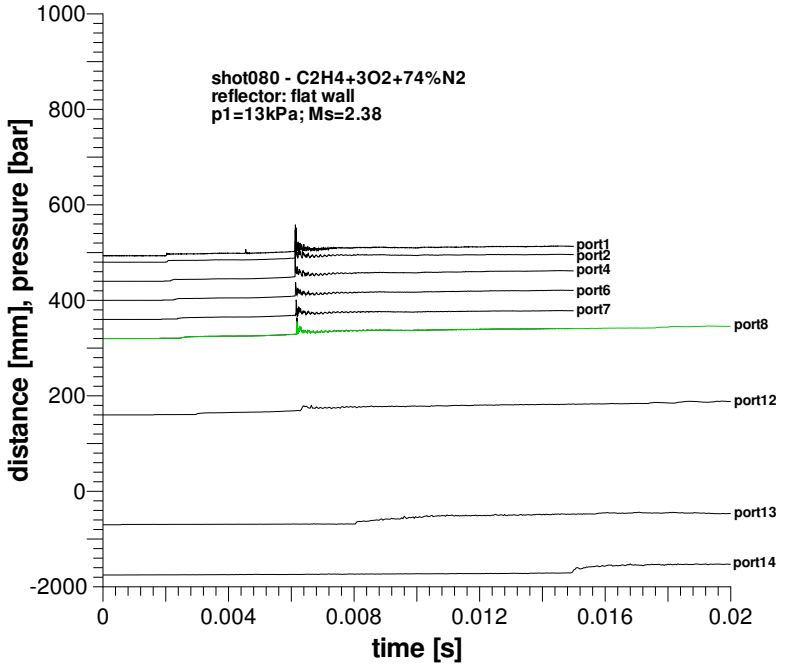

Figure 81: Deflagration-to-detonation transition DDT (shot 080); test mixture: C_2H_4+3O_2+74%N_2; incident shock wave Mach number: $M_s = 2.38$.

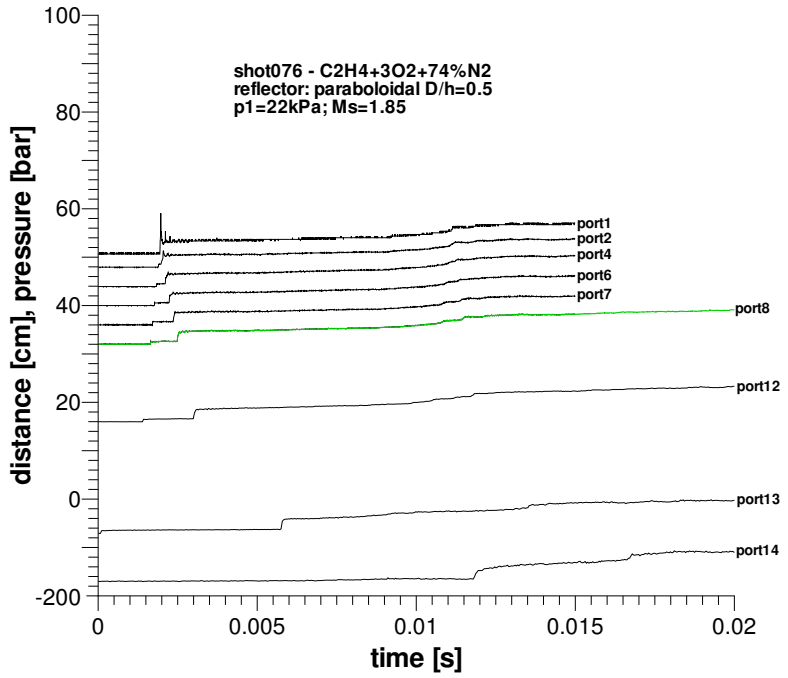

Figure 82: No combustion (shot 076); test mixture: C_2H_4+3O_2+74%N_2; incident shock Mach number: $M_s = 1.85$.

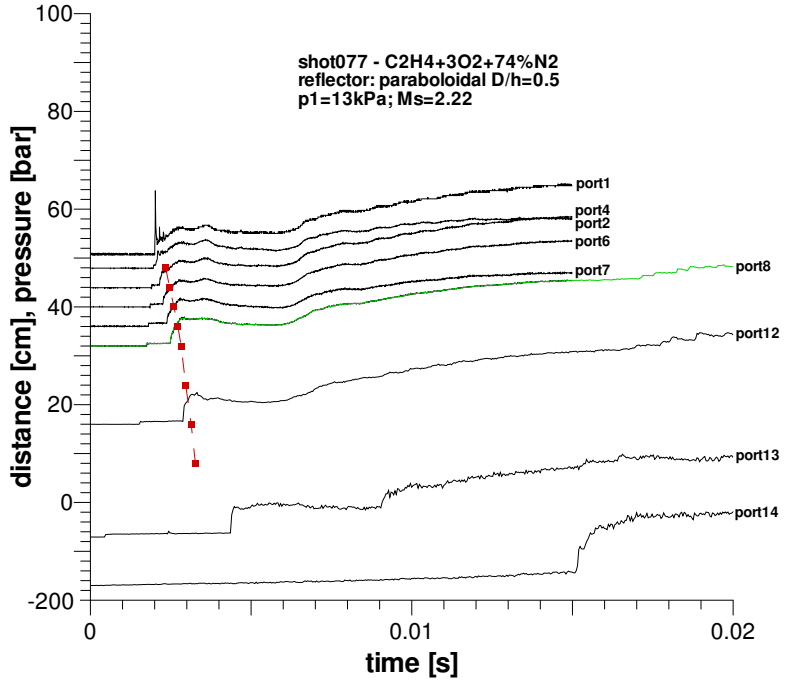

Figure 83: Deflagration outside reflector (shot 077); test mixture: C_2H_4+3O_2+74%N_2; incident shock Mach number: $M_s = 2.22$.

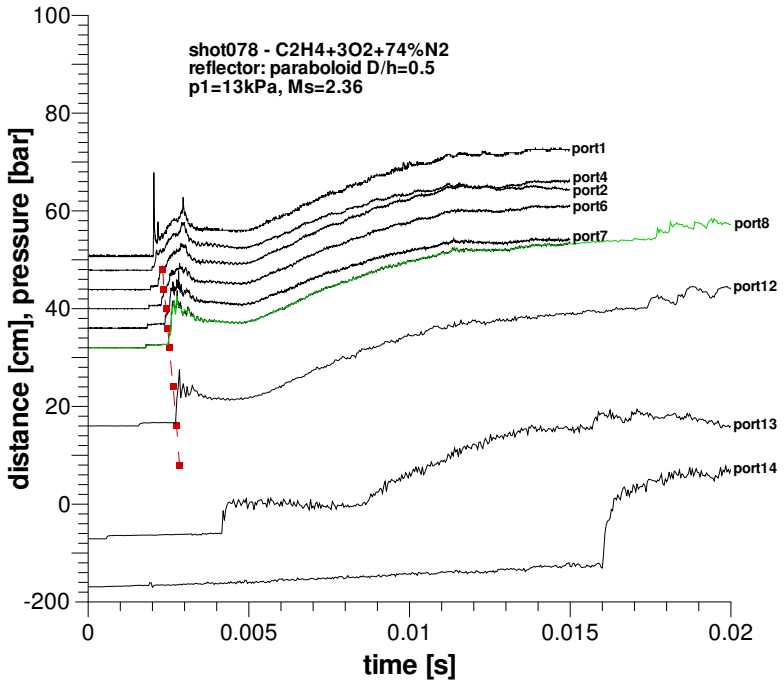

Figure 84: Deflagration-to-detonation transition DDT (shot 078); test mixture: C_2H_4+3O_2+74%N_2; incident shock wave Mach number: $M_s = 2.36$.

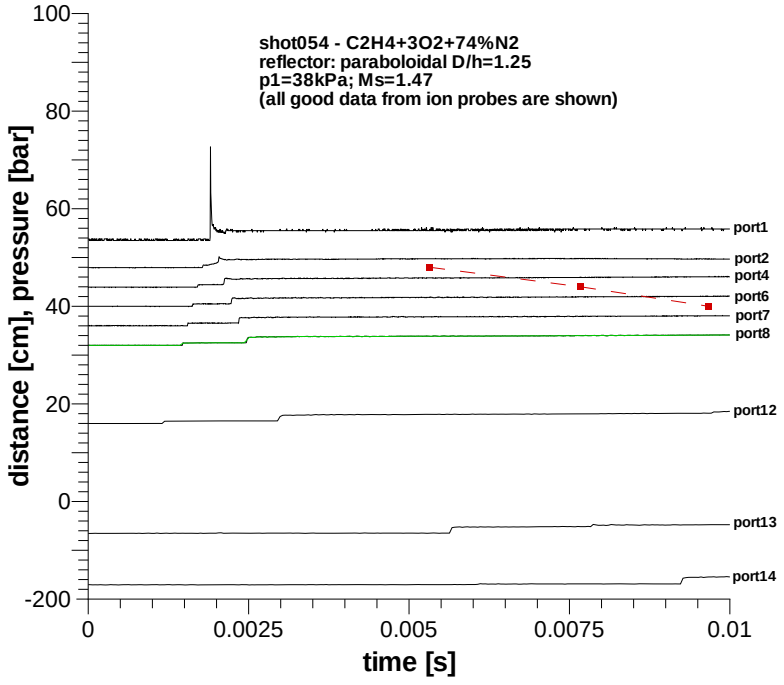

Figure 85: Deflagration outside reflector (shot 054); test mixture: C_2H_4+3O_2+74%N_2; incident shock Mach number: $M_s = 1.47$.

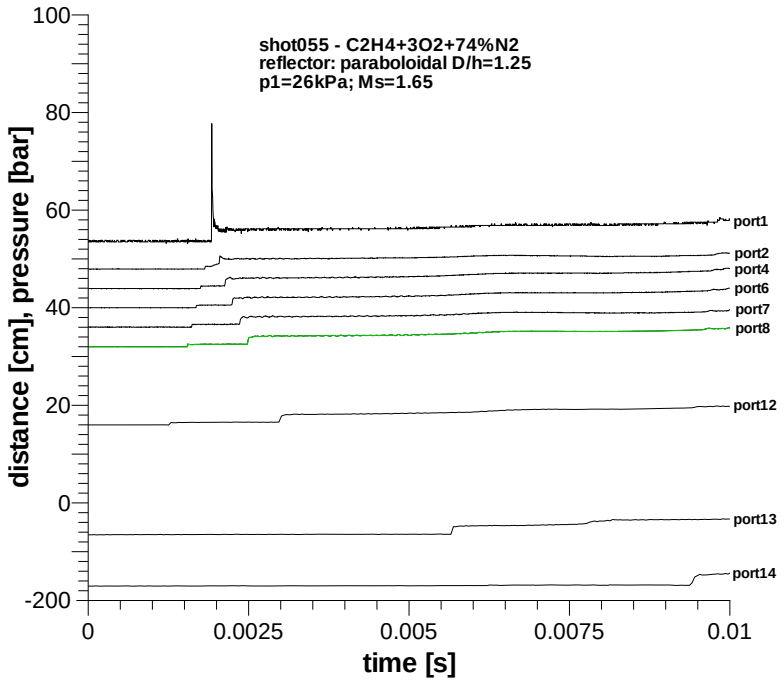

Figure 86: Deflagration outside reflector (shot 055); test mixture: C_2H_4+3O_2+74%N_2; incident shock Mach number: $M_s = 1.65$.

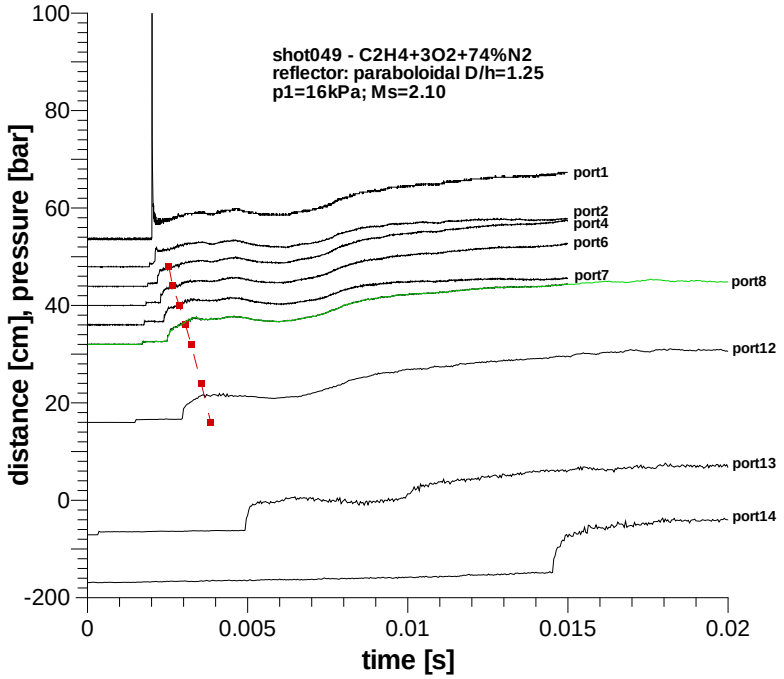

Figure 87: Deflagration outside reflector (shot 049); test mixture: C_2H_4+3O_2+74%N_2; incident shock Mach number: $M_s = 2.10$.

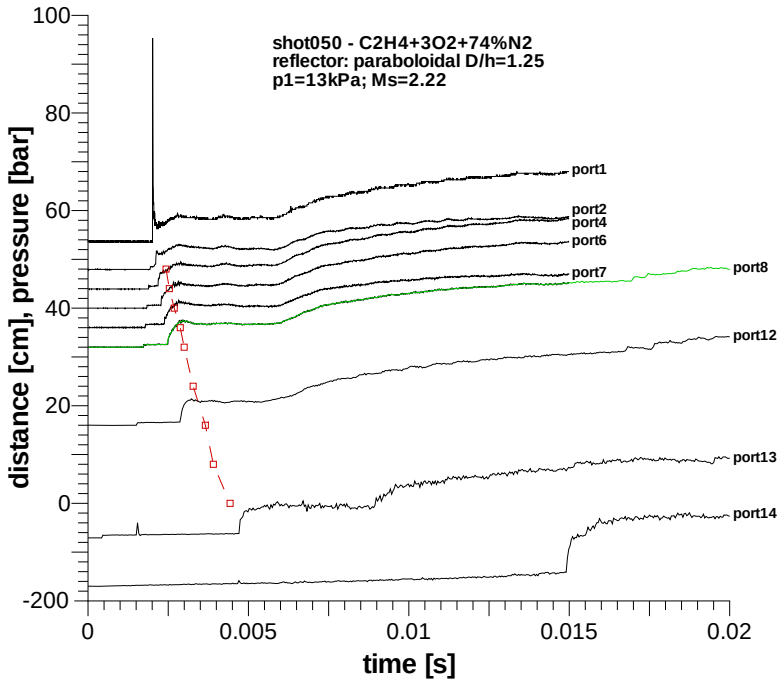

Figure 88: Deflagration outside reflector (shot 050); test mixture: C_2H_4+3O_2+74%N_2; incident shock Mach number: $M_s = 2.22$.

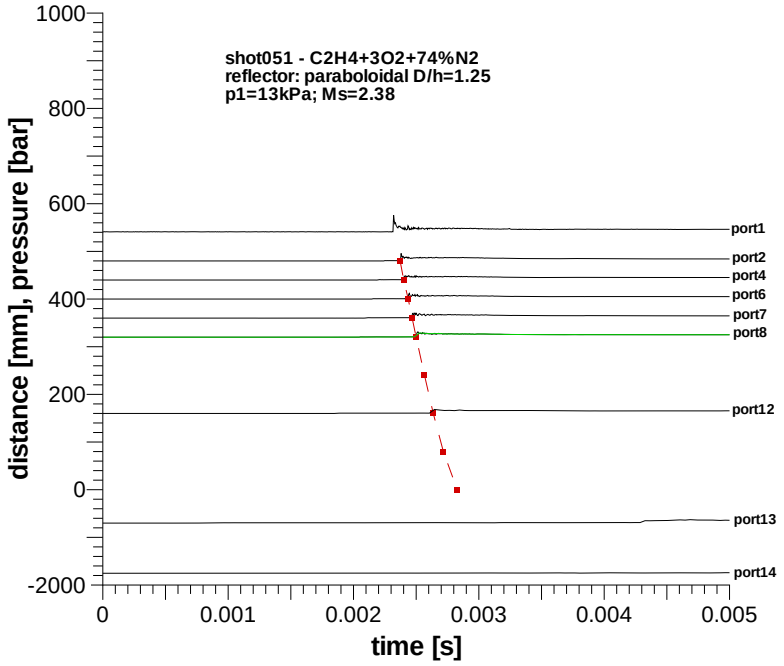

Figure 89: Detonation inside reflector (shot 051); test mixture: C_2H_4+3O_2+74%N_2; incident shock Mach number: $M_s = 2.38$.

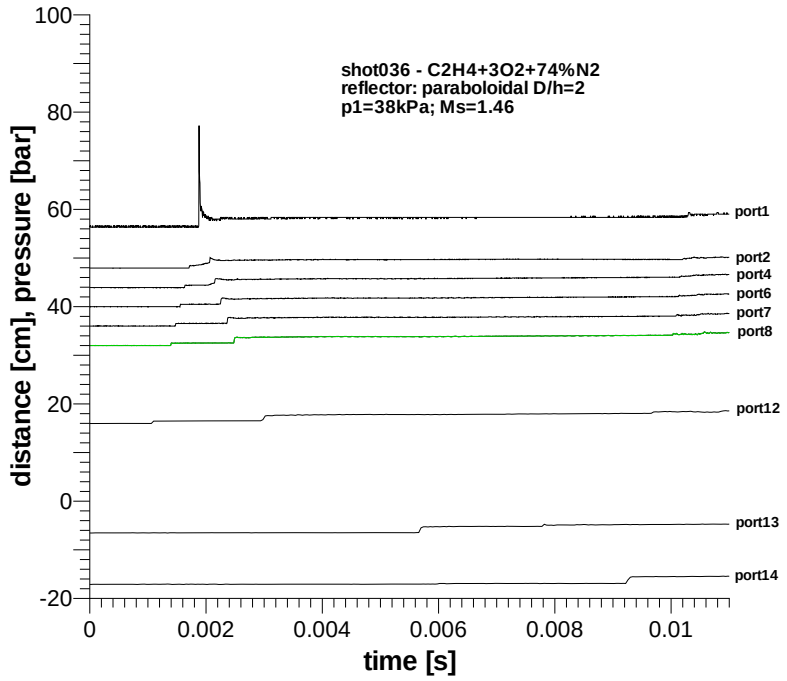

Figure 90: Deflagration outside reflector (shot 036); test mixture: C_2H_4+3O_2+74%N_2; incident shock Mach number: $M_s = 1.46$.

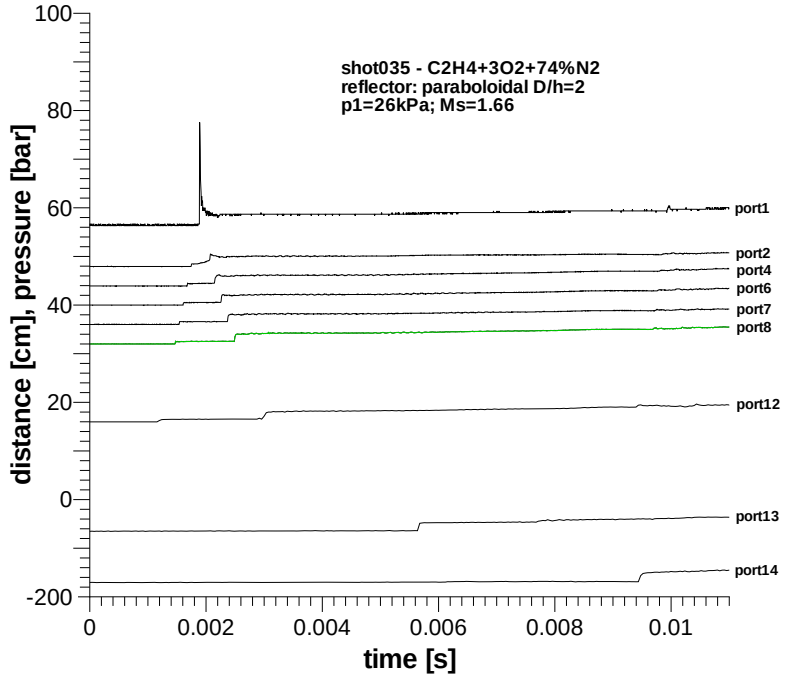

Figure 91: Deflagration outside reflector (shot 035); test mixture: C_2H_4+3O_2+74%N_2; incident shock Mach number: $M_s = 1.66$.

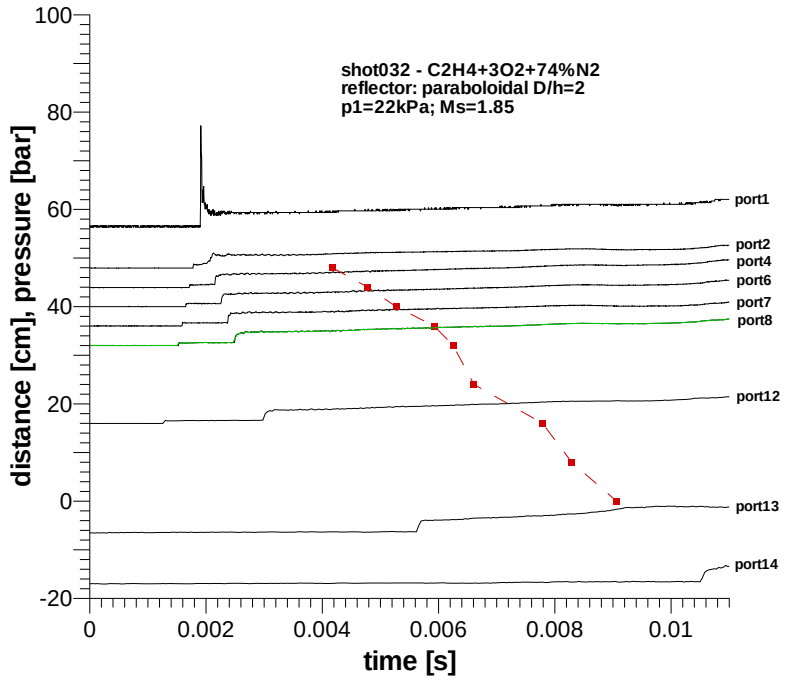

Figure 92: Deflagration outside reflector (shot 032); test mixture: C_2H_4+3O_2+74%N_2; incident shock Mach number: $M_s = 1.85$.

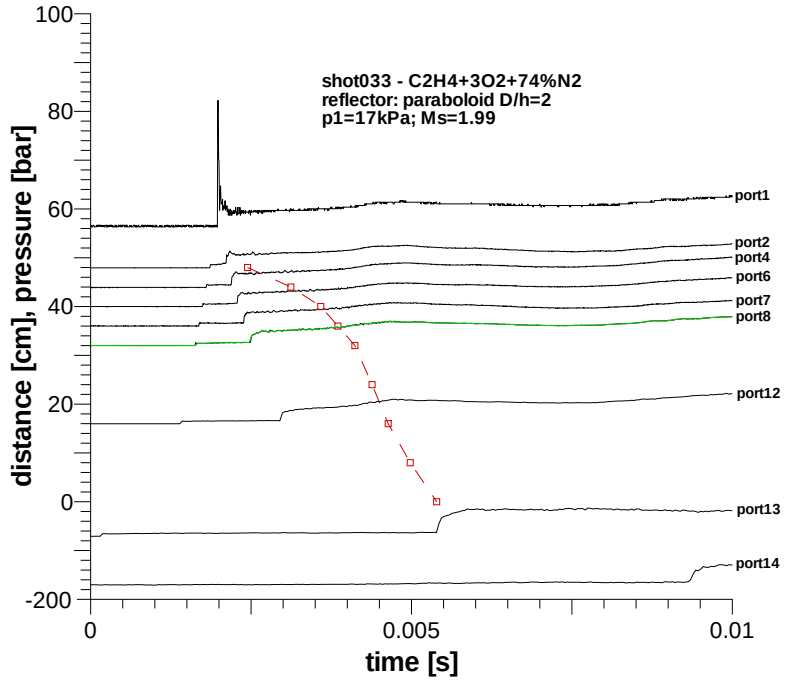

Figure 93: Deflagration outside reflector (shot 033); test mixture: C_2H_4+3O_2+74%N_2; incident shock Mach number: $M_s = 1.99$.

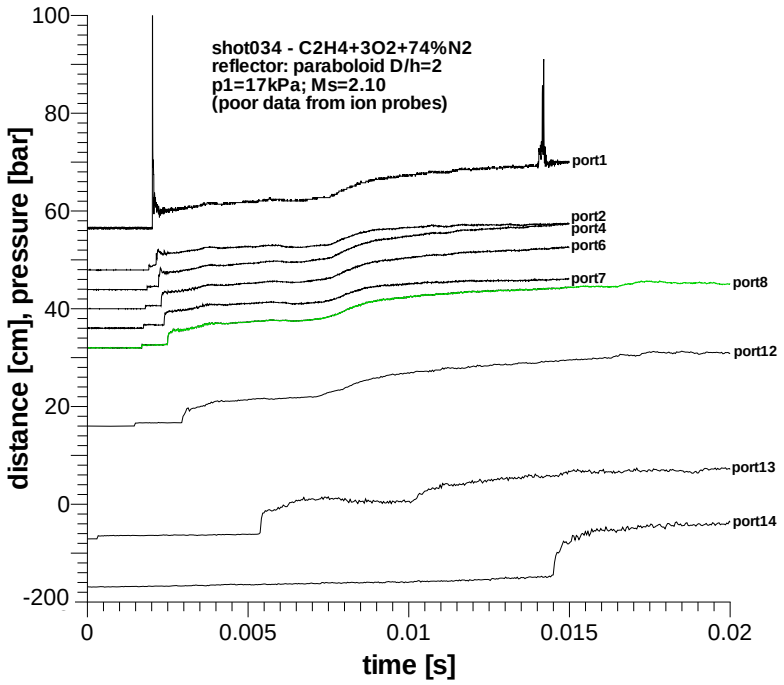

Figure 94: Deflagration outside reflector (shot 034); test mixture: C_2H_4+3O_2+74%N_2; incident shock Mach number: $M_s = 2.10$.

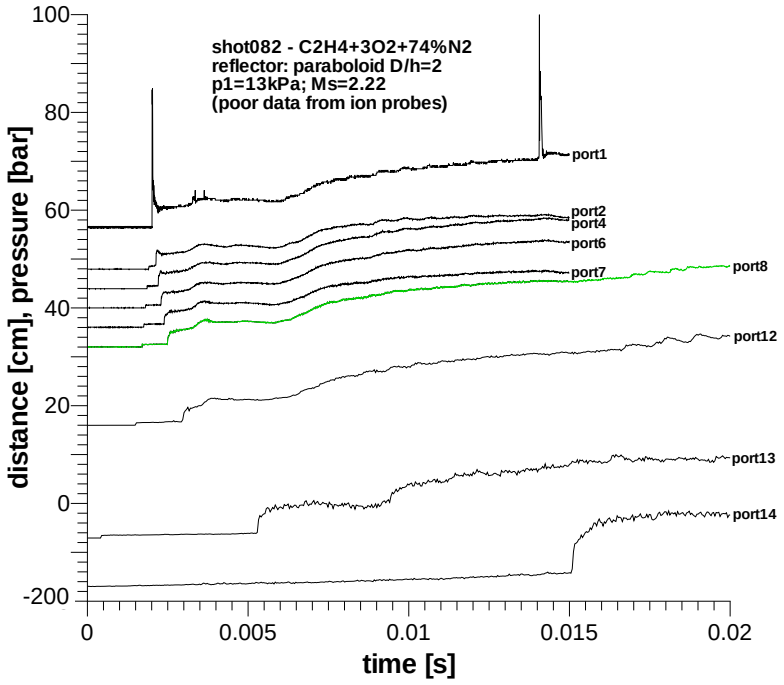

Figure 95: Deflagration outside reflector (shot 082); test mixture: C_2H_4+3O_2+74%N_2; incident shock Mach number: $M_s = 2.22$.

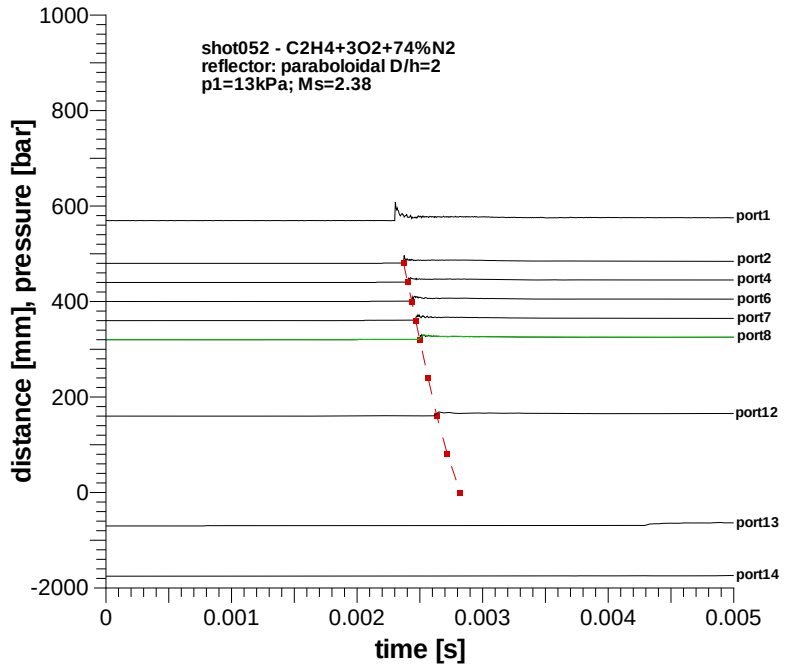

Figure 96: Detonation inside reflector (shot 052); test mixture: C_2H_4+$3O_2$+74%N_2; incident shock Mach number: $M_s = 2.38$.

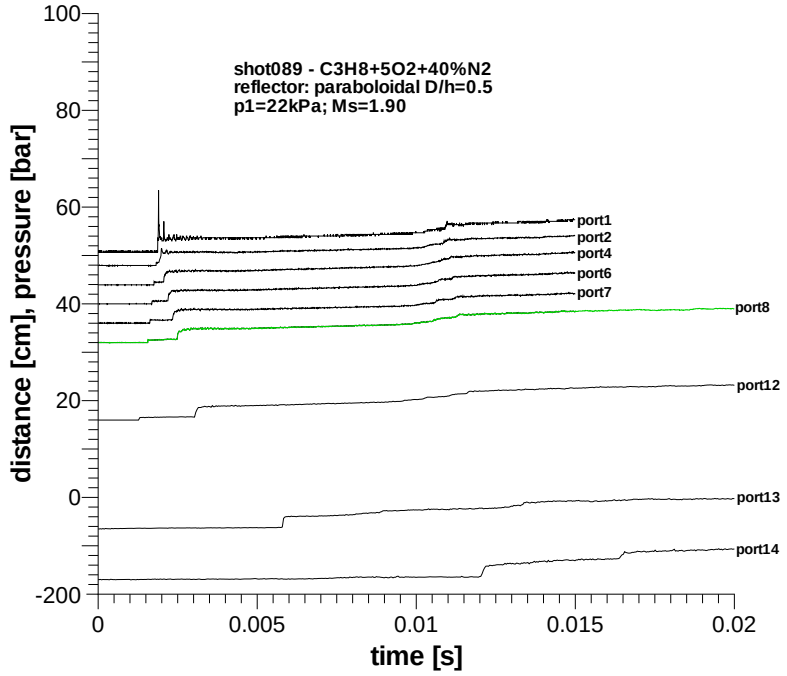

Figure 97: No combustion (shot 089); test mixture: C_3H_8+$5O_2$+40%N_2; incident shock Mach number: $M_s = 1.90$.

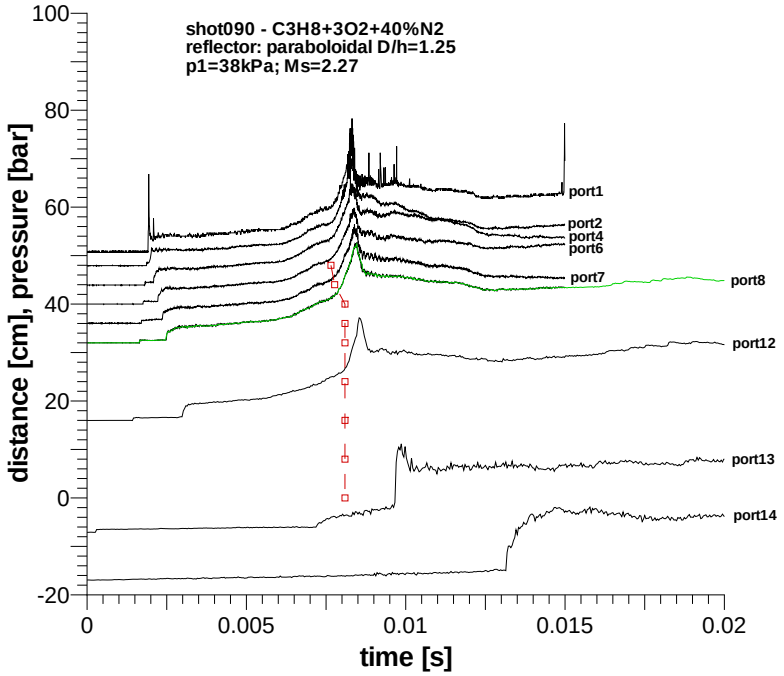

Figure 98: Deflagration outside reflector (shot 090); test mixture: C_3H_8+5O_2+40%N_2; incident shock Mach number: $M_s = 2.27$.

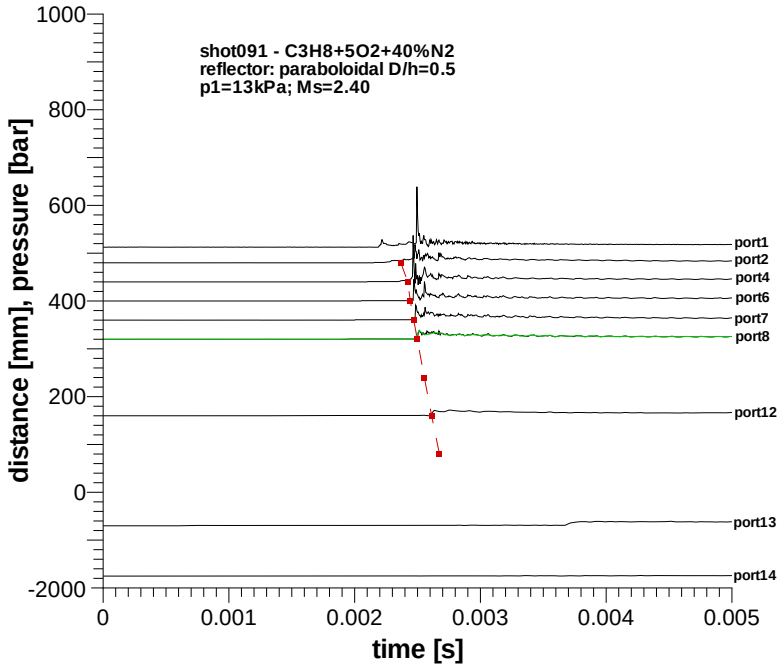

Figure 99: Deflagration outside reflector (shot 091); test mixture: C_3H_8+5O_2+40%N_2; incident shock Mach number: $M_s = 2.40$.

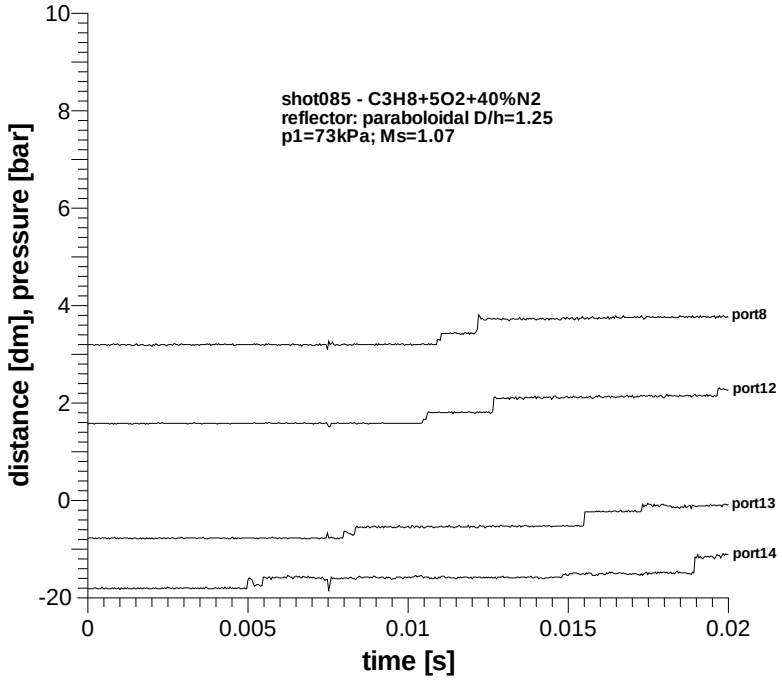

Figure 100: No combustion (shot 085); test mixture: C_3H_8+5O_2+40%N_2; incident shock Mach number: $M_s = 1.07$.

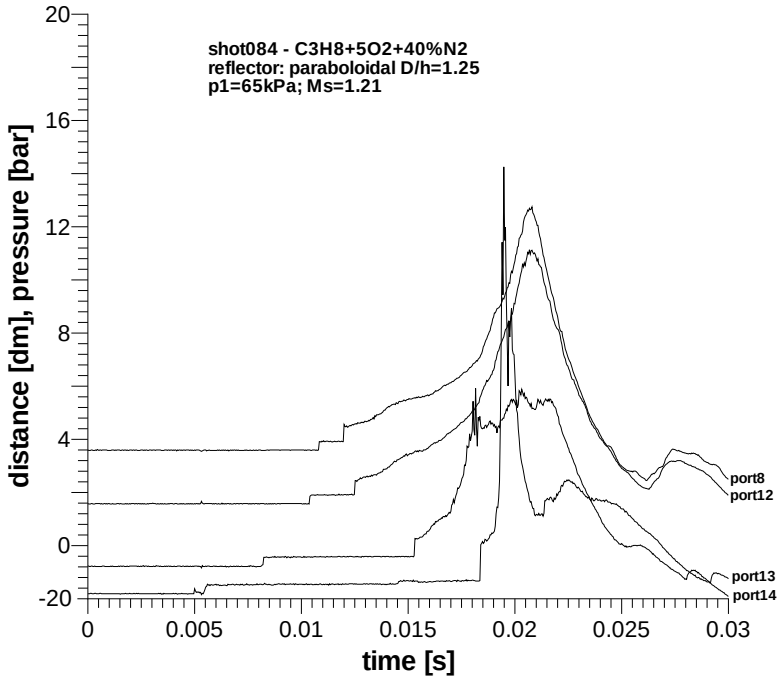

Figure 101: Deflagration outside reflector (shot 084); test mixture: C_3H_8+5O_2+40%N_2; incident shock Mach number: $M_s = 1.21$.

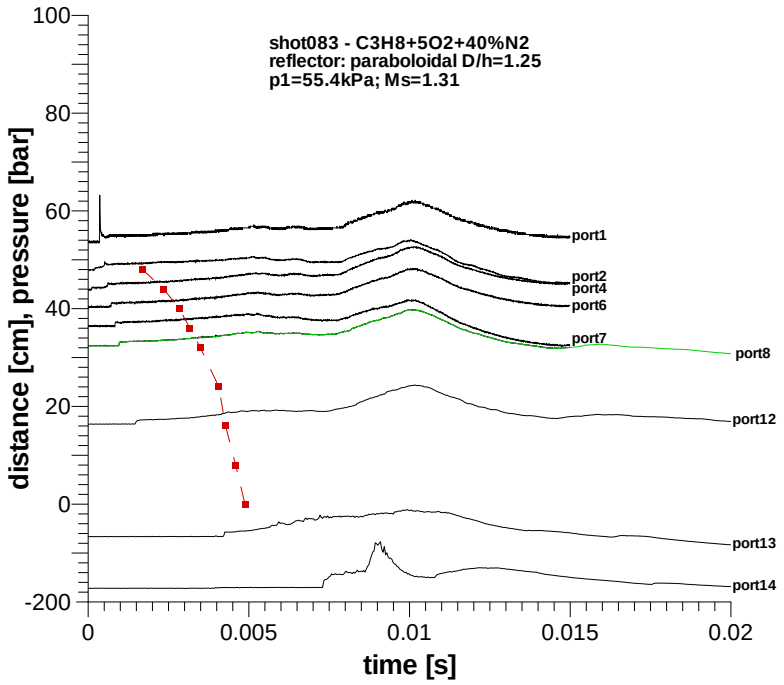

Figure 102: Deflagration outside reflector (shot 083); test mixture: C_3H_8+$5O_2$+40%N_2; incident shock Mach number: $M_s = 1.31$.

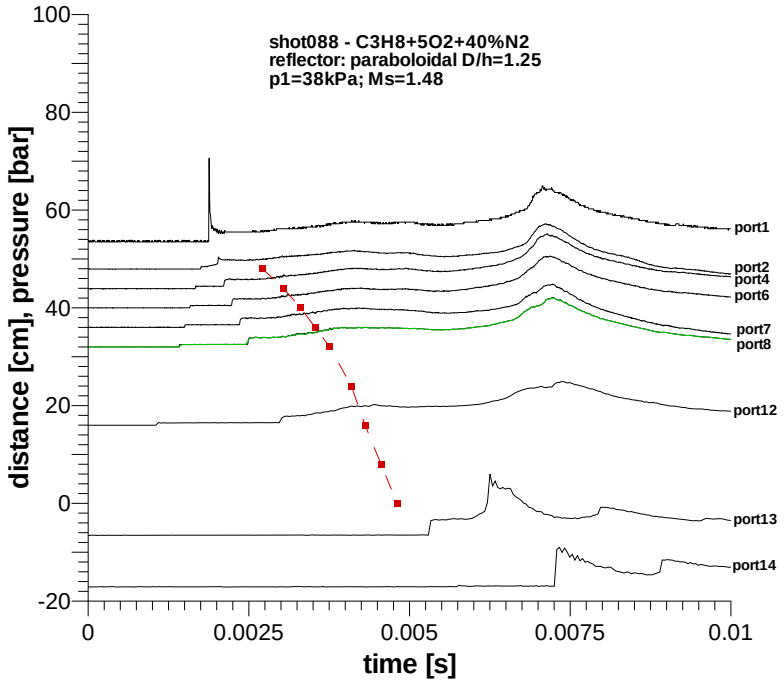

Figure 103: Deflagration outside reflector (shot 088); test mixture: C_3H_8+$5O_2$+40%N_2; incident shock Mach number: $M_s = 1.48$.

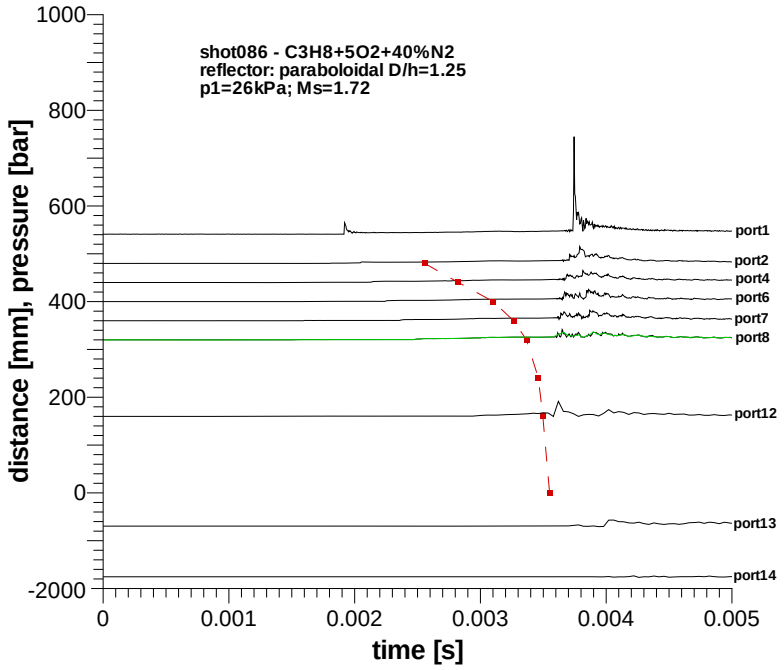

Figure 104: Deflagration-to-detonation transition DDT (shot 086); test mixture: C_3H_8+$5O_2$+$40\%N_2$; incident shock wave Mach number: $M_s = 1.72$.

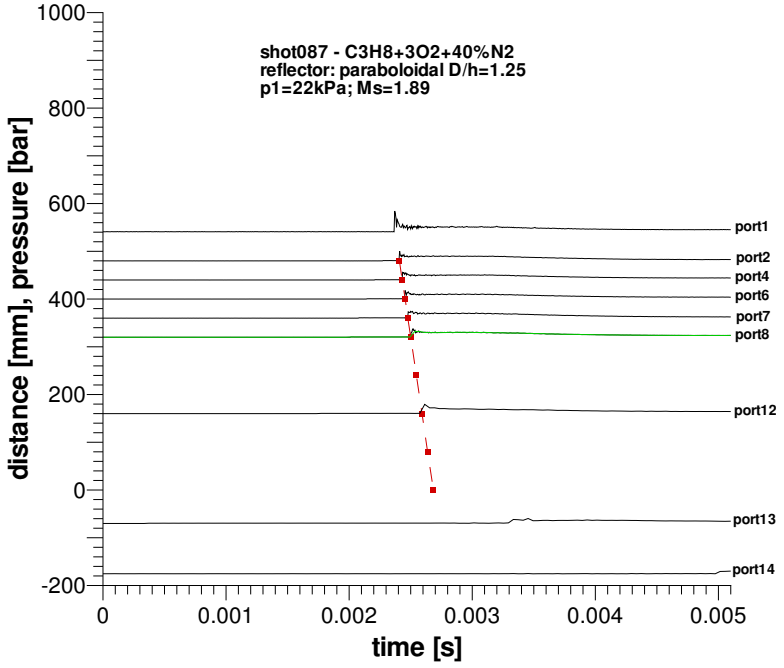

Figure 105: Detonation inside reflector (shot 087); test mixture: C_3H_8+$5O_2$+$40\%N_2$; incident shock Mach number: $M_s = 1.89$.

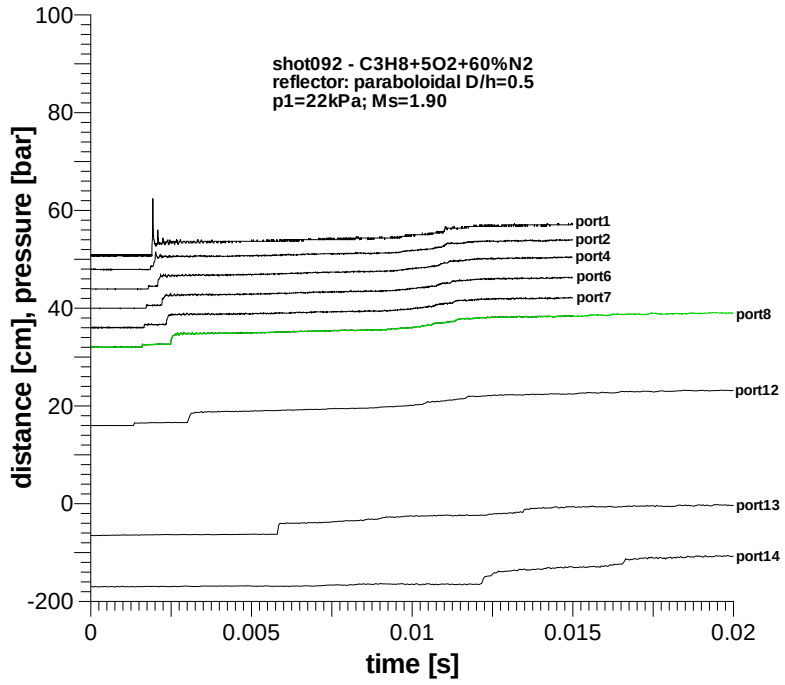

Figure 106: No combustion (shot 092); test mixture: C_3H_8+5O_2+60%N_2; incident shock Mach number: $M_s = 1.90$.

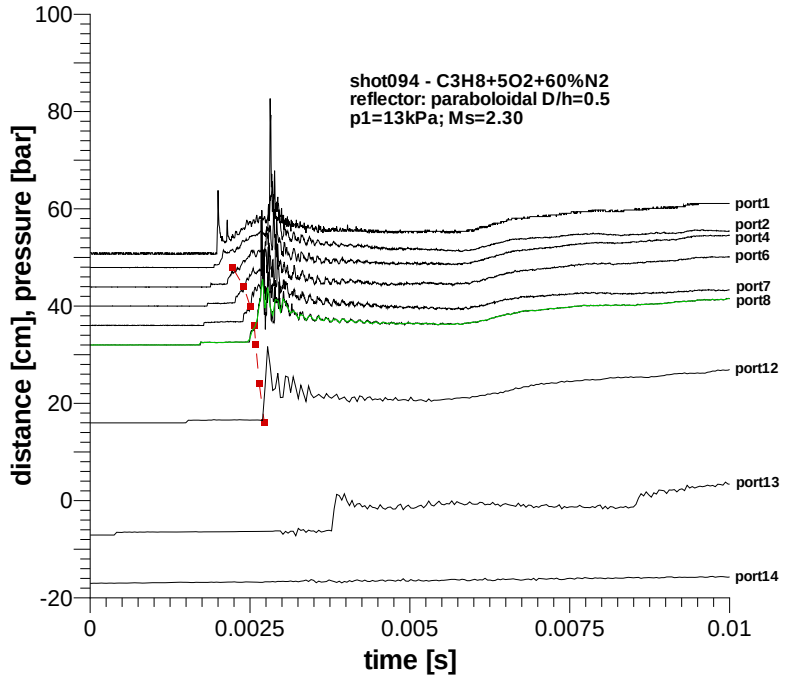

Figure 107: Deflagration outside reflector (shot 094); test mixture: C_3H_8+5O_2+60%N_2; incident shock Mach number: $M_s = 2.30$.

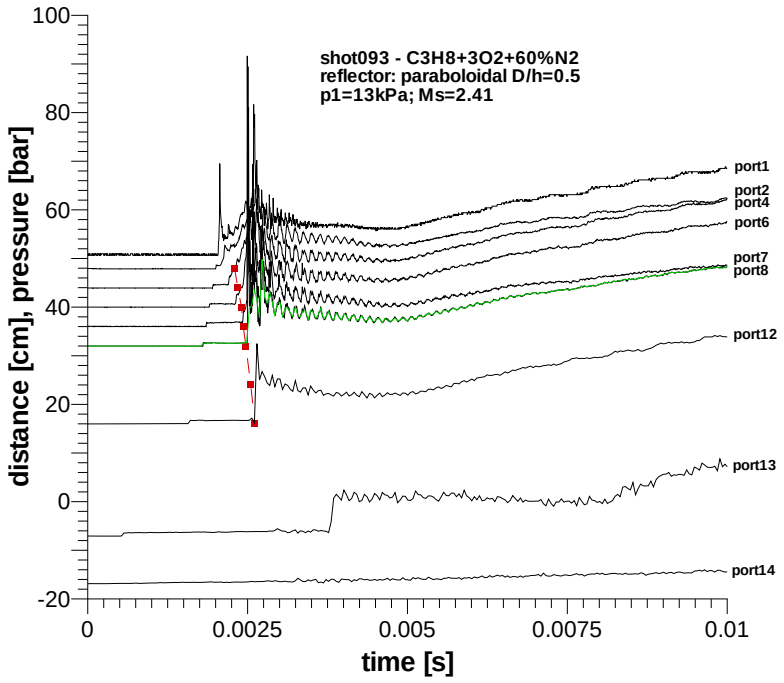

Figure 108: Deflagration outside reflector (shot 093); test mixture: C_3H_8+5O_2+60%N_2; incident shock Mach number: $M_s = 2.41$.

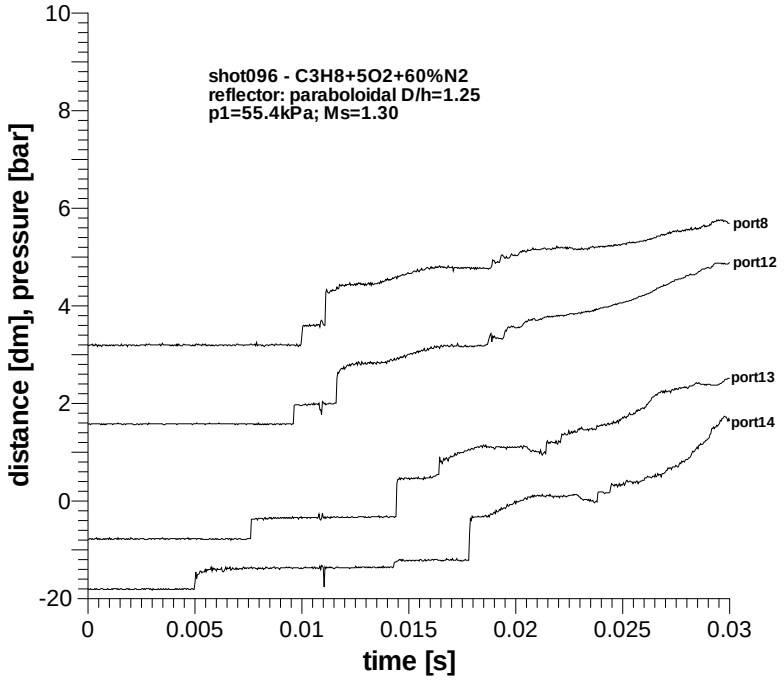

Figure 109: Deflagration outside reflector (shot 096); test mixture: C_3H_8+5O_2+60%N_2; incident shock Mach number: $M_s = 1.30$.

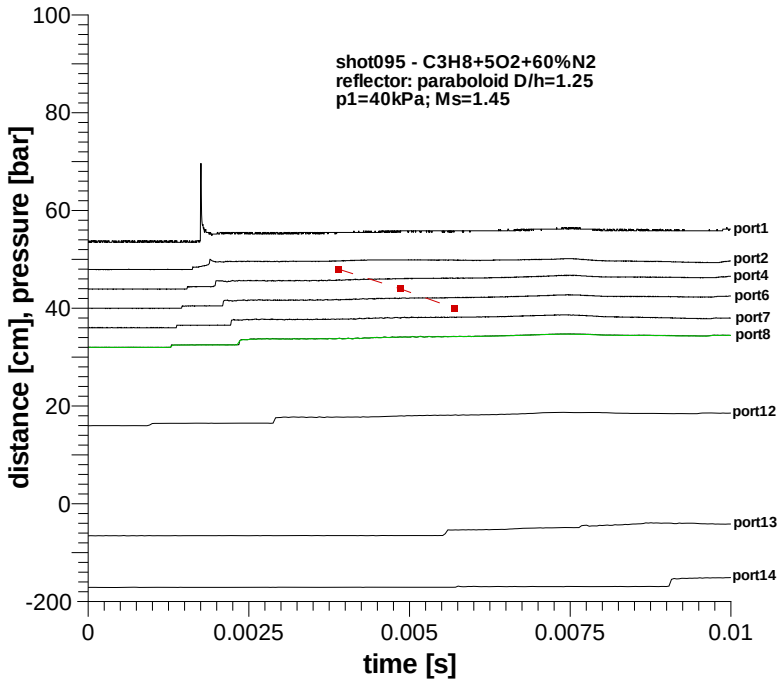

Figure 110: Deflagration outside reflector (shot 095); test mixture: C_3H_8+5O_2+60%N_2; incident shock Mach number: $M_s = 1.45$.

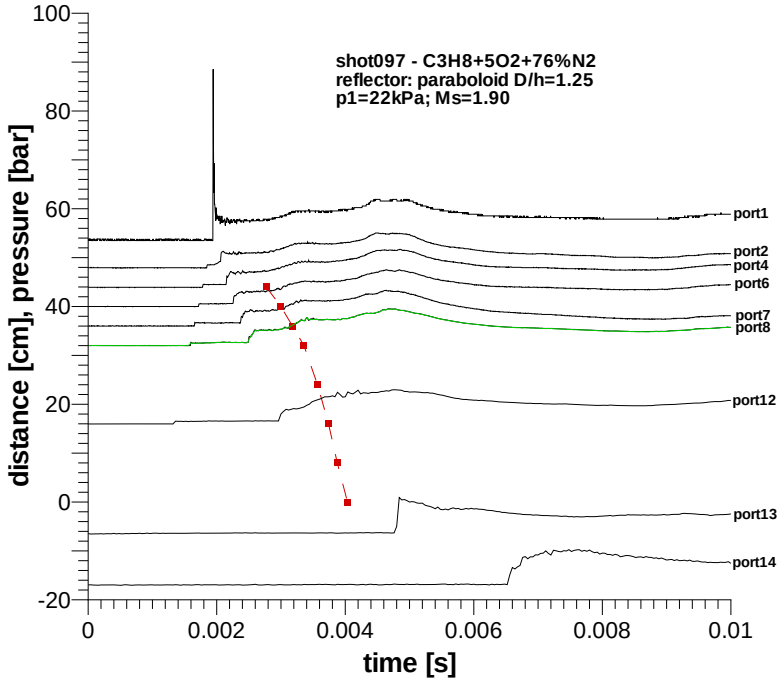

Figure 111: Deflagration outside reflector (shot 097); test mixture: C_3H_8+5O_2+60%N_2; incident shock Mach number: $M_s = 1.90$.

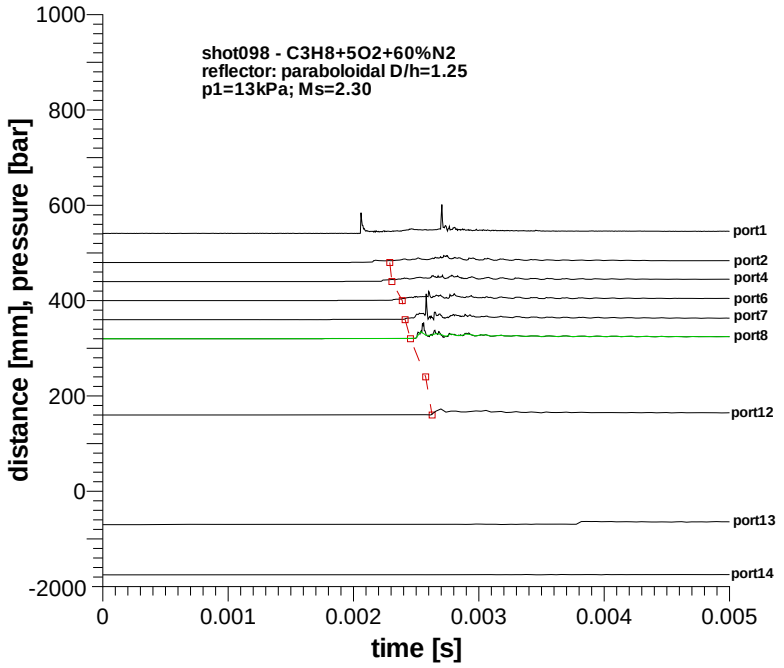

Figure 112: Deflagration-to-detonation transition DDT (shot 098); test mixture: C_3H_8+$5O_2$+40%N_2; incident shock wave Mach number: $M_s = 2.30$.

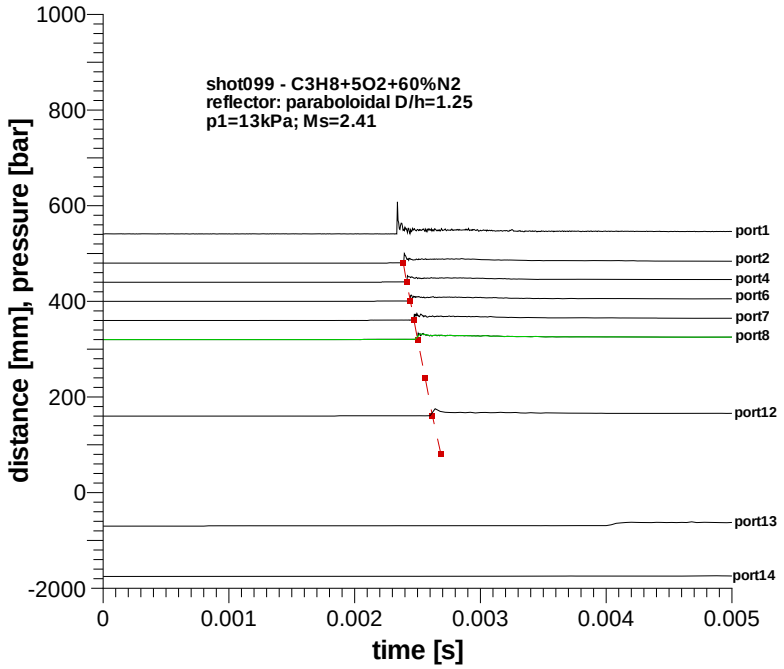

Figure 113: Detonation inside reflector (shot 099); test mixture: C_3H_8+$5O_2$+60%N_2; incident shock Mach number: $M_s = 2.41$.

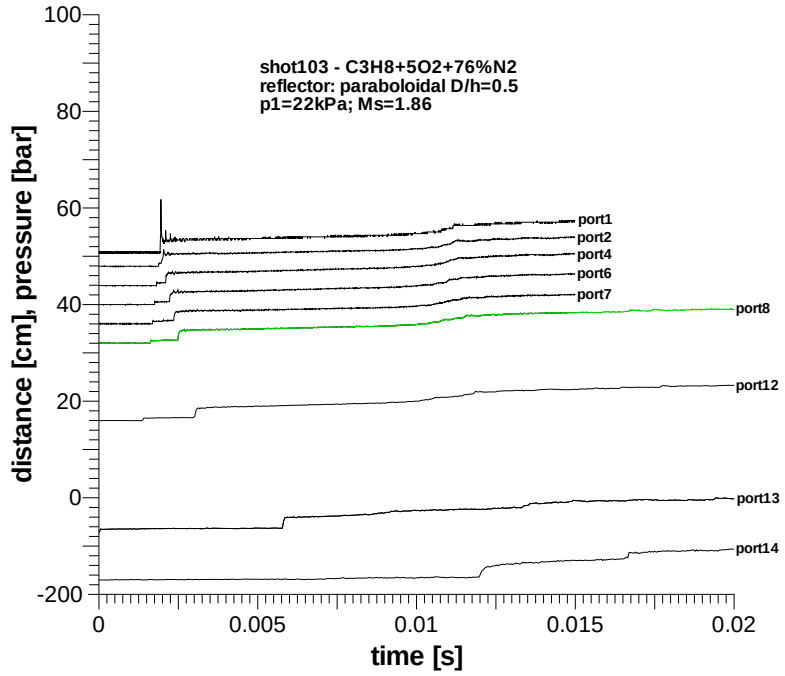

Figure 114: No combustion (shot 103); test mixture: C_3H_8+5O_2+76%N_2; incident shock Mach number: $M_s = 1.86$.

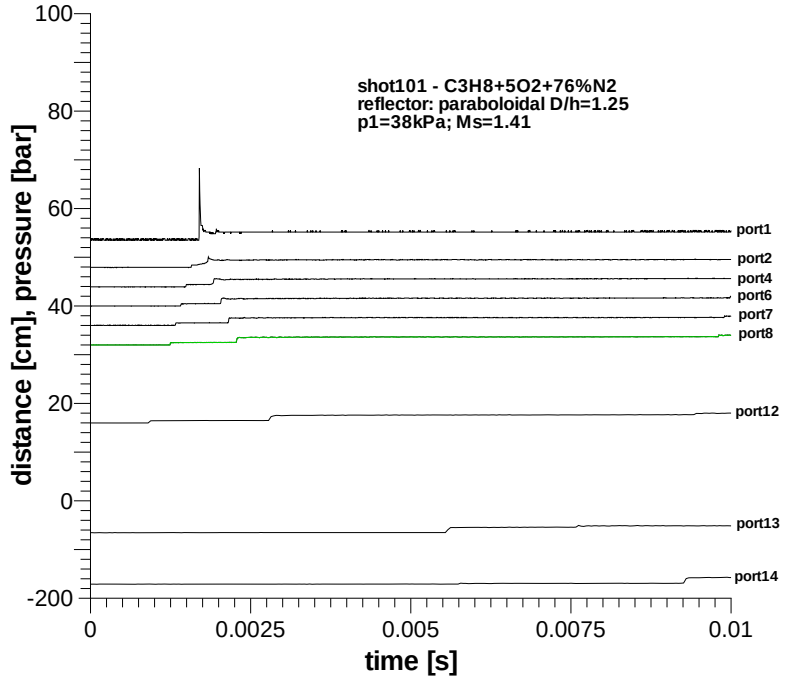

Figure 115: No combustion (shot 101); test mixture: C_3H_8+5O_2+76%N_2; incident shock Mach number: $M_s = 1.41$.

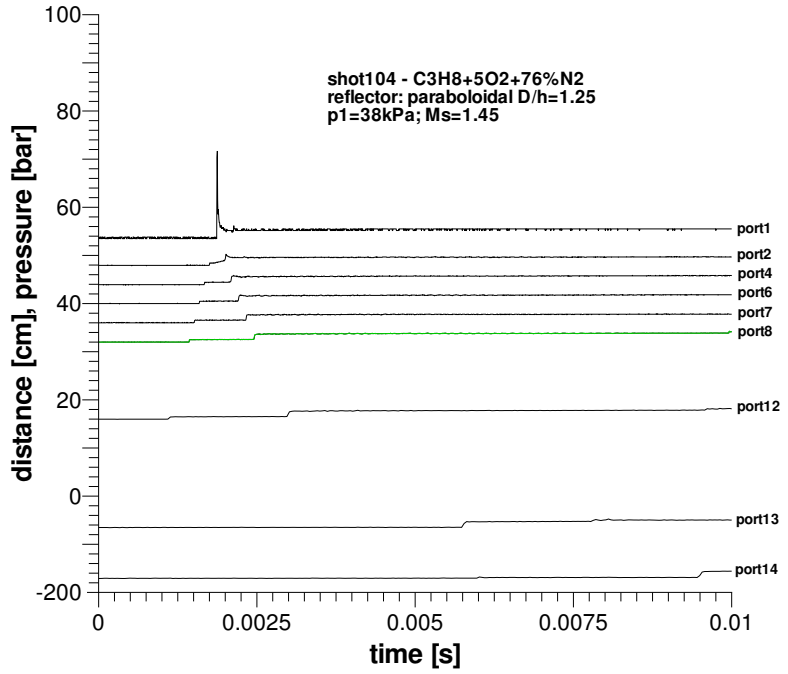

Figure 116: No combustion (shot 104); test mixture: C_3H_8+5O_2+76%N_2; incident shock Mach number: $M_s = 1.45$.

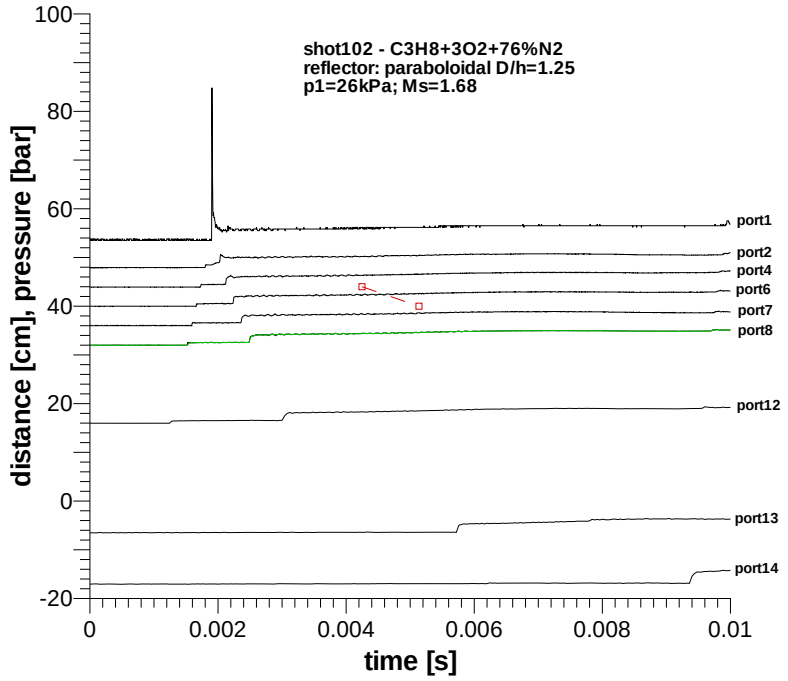

Figure 117: Deflagration outside reflector (shot 102); test mixture: C_3H_8+5O_2+76%N_2; incident shock Mach number: $M_s = 1.68$.

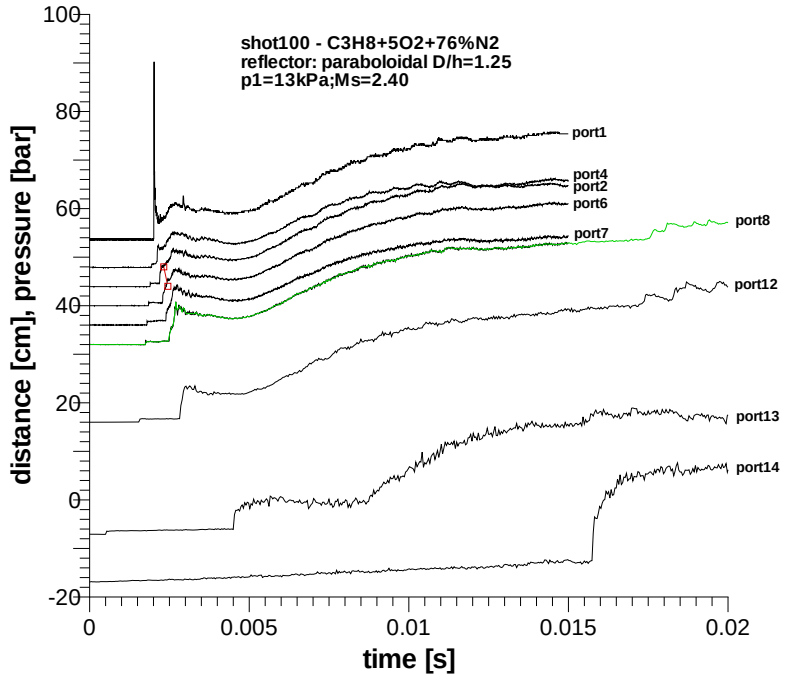

Figure 118: Deflagration outside reflector (shot 100); test mixture: C_3H_8+$5O_2$+$76\%N_2$; incident shock Mach number: $M_s = 2.40$.

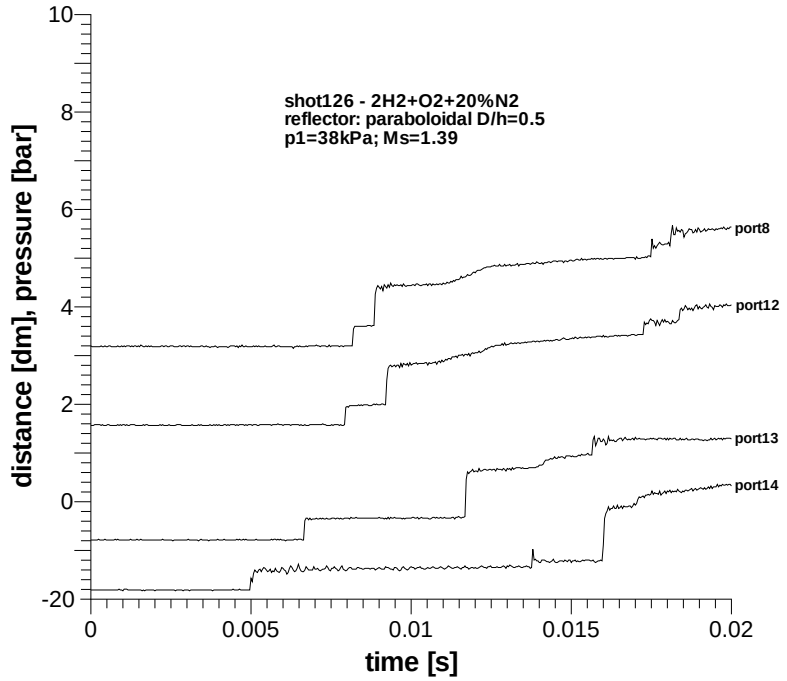

Figure 119: No combustion (shot 126); test mixture: $2H_2$+O_2+$20\%N_2$; incident shock Mach number: $M_s = 1.39$.

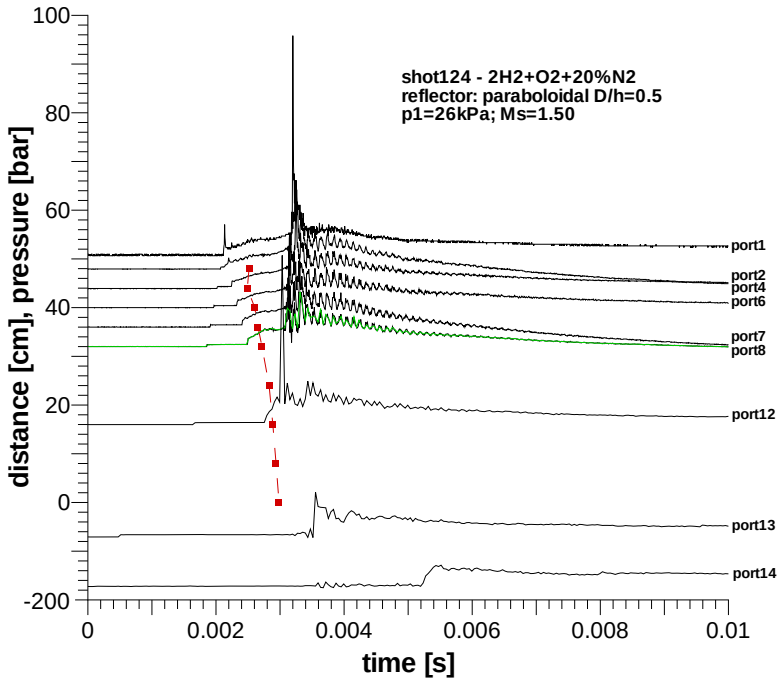

Figure 120: Deflagration outside reflector (shot 124); test mixture: $2H_2$+O_2+20%N_2; incident shock Mach number: $M_s = 1.50$.

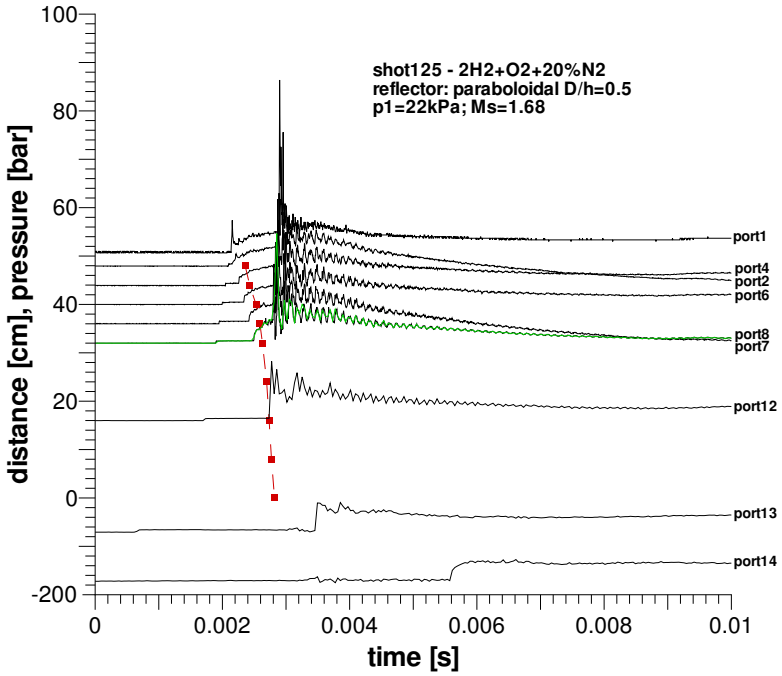

Figure 121: Deflagration-to-detonation transition DDT (shot 125); test mixture: $2H_2$+O_2+20%N_2; incident shock wave Mach number: $M_s = 1.68$.

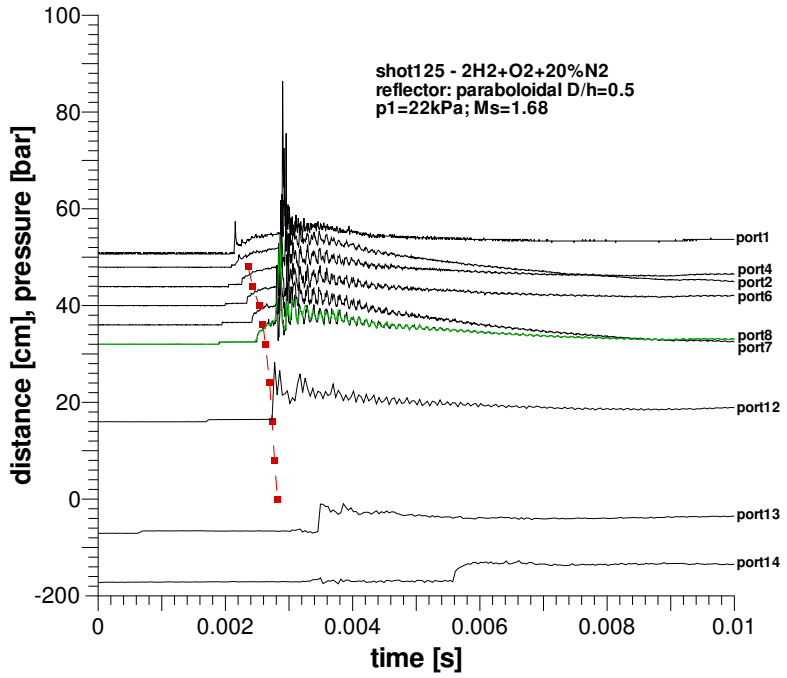

Figure 122: Direct initiation of deflagration (shot 127); test mixture: $2H_2+O_2+20\%N_2$; incident shock Mach number: $M_s = 1.85$.

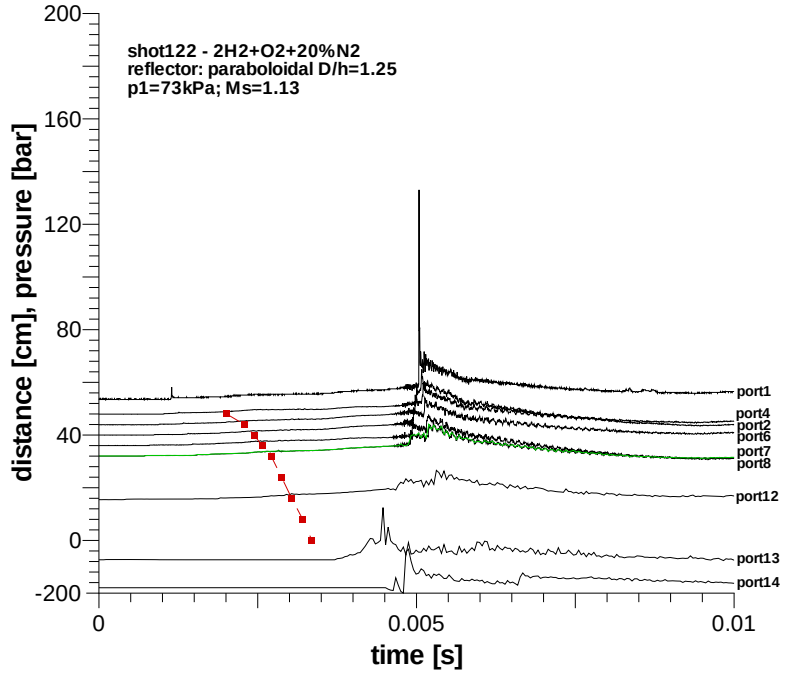

Figure 123: Deflagration outside reflector (shot 122); test mixture: $2H_2+O_2+20\%N_2$; incident shock Mach number: $M_s = 1.13$.

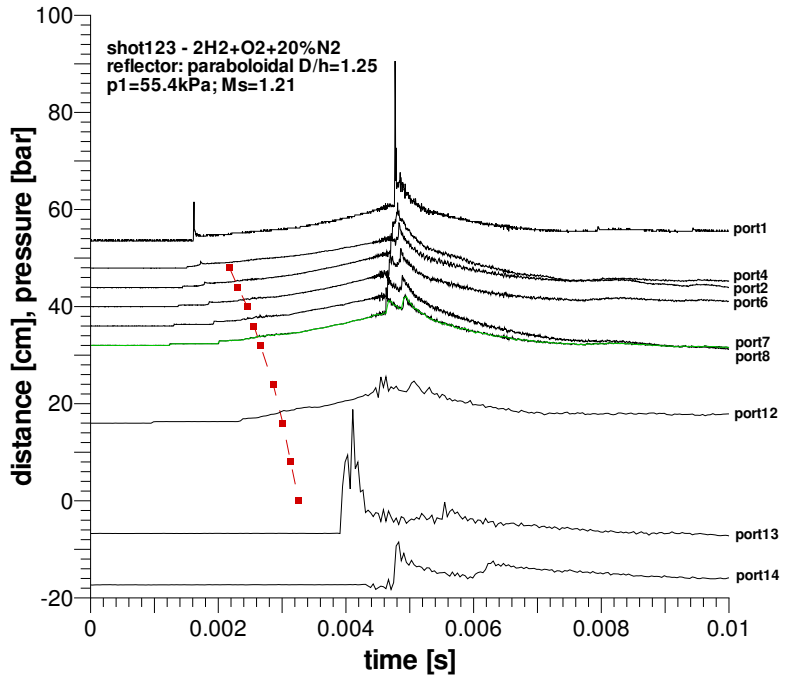

Figure 124: Deflagration outside reflector (shot 123; test mixture: $2H_2+O_2+20\%N_2$; incident shock Mach number: $M_s = 1.21$.

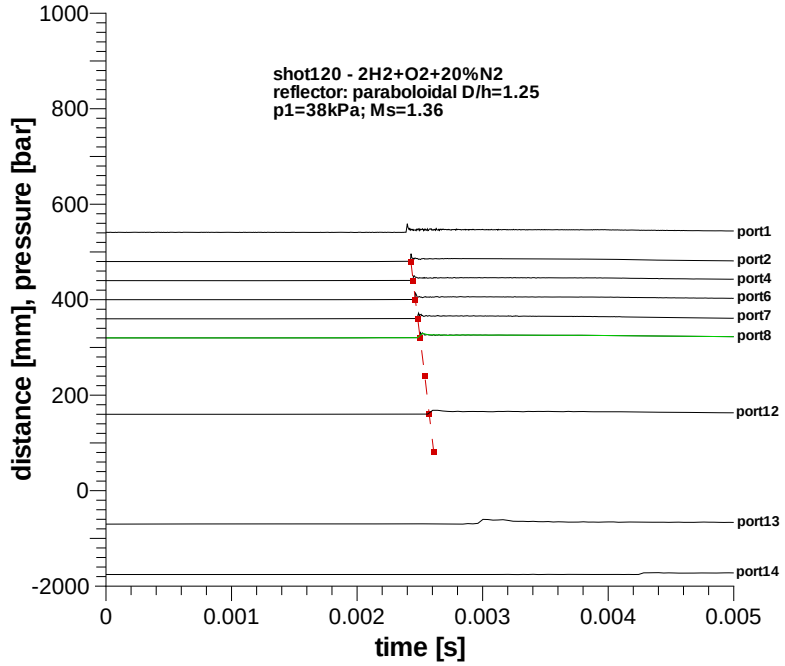

Figure 125: Detonation inside reflector (shot 120); test mixture: $2H_2+O_2+20\%N_2$; incident shock Mach number: $M_s = 1.36$.

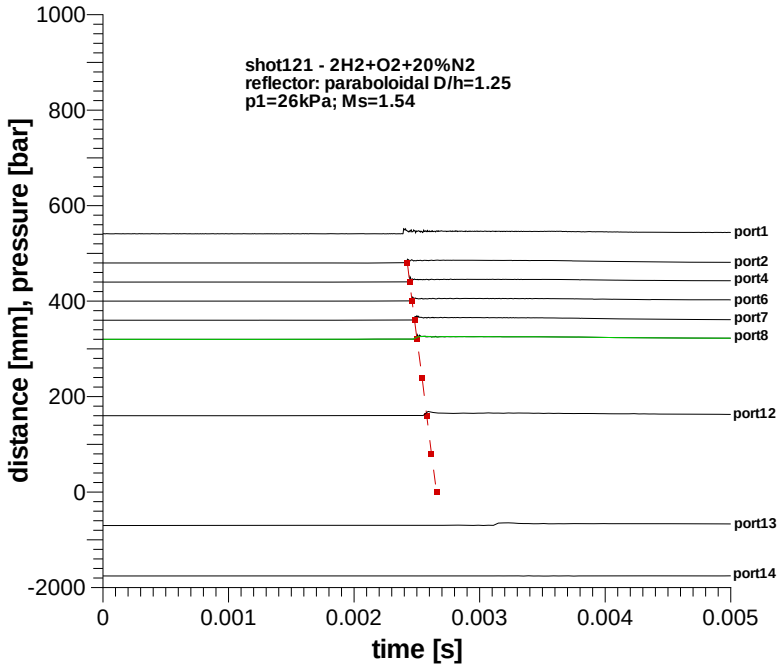

Figure 126: Detonation inside reflector (shot 121); test mixture: $2H_2+O_2+20\%N_2$; incident shock Mach number: $M_s = 1.54$.

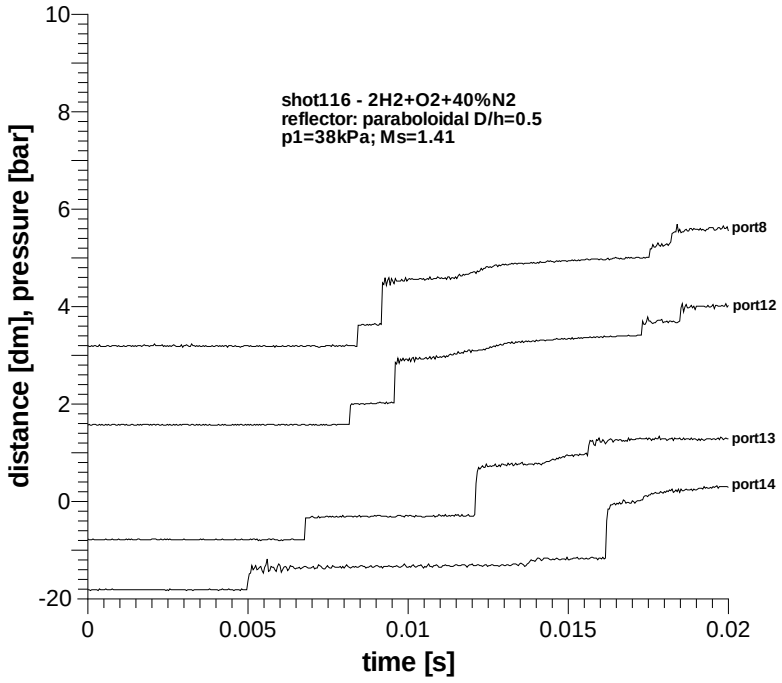

Figure 127: No combustion (shot 116); test mixture: $2H_2+O_2+40\%N_2$; incident shock Mach number: $M_s = 1.41$.

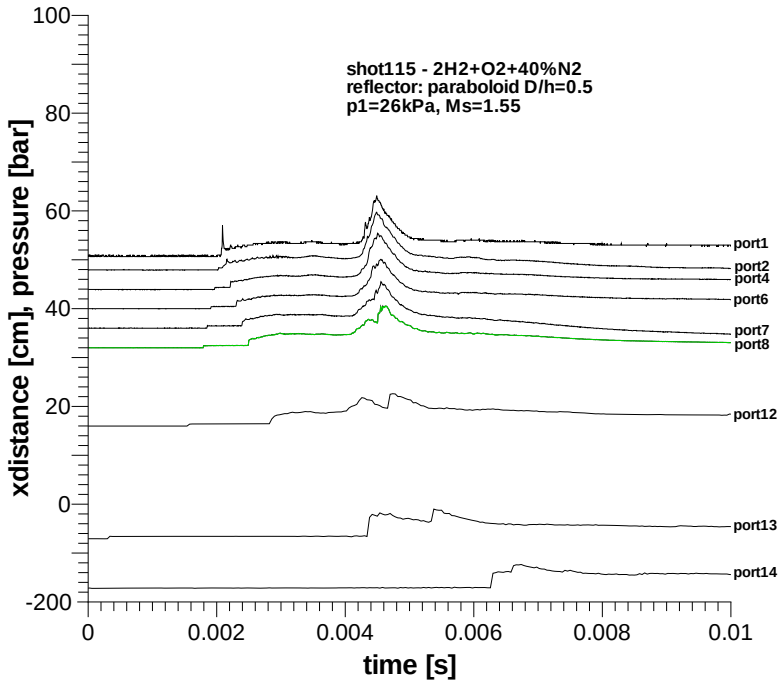

Figure 128: Deflagration outside reflector (shot 115; test mixture: $2H_2+O_2+40\%N_2$; incident shock Mach number: $M_s = 1.55$.

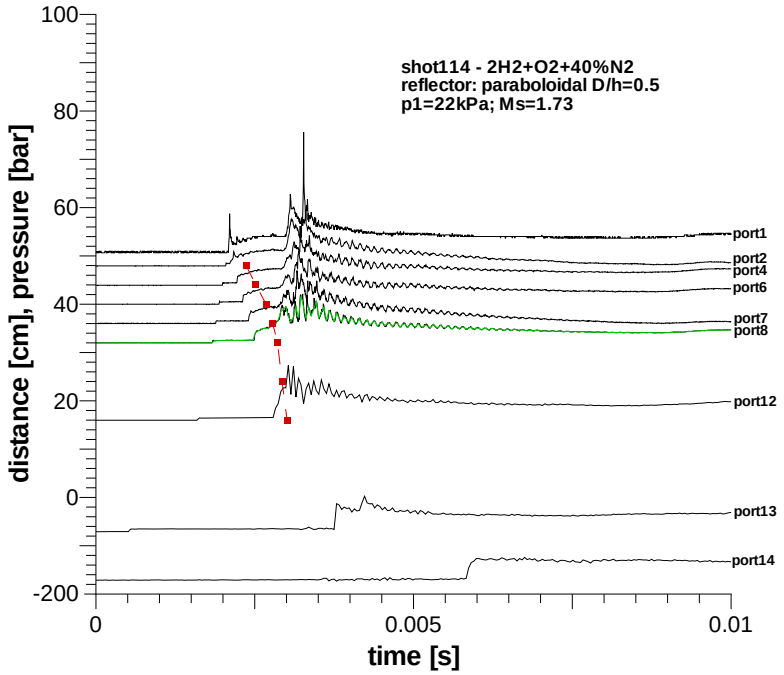

Figure 129: Deflagration outside reflector (shot 114); test mixture: $2H_2+O_2+40\%N_2$; incident shock Mach number: $M_s = 1.73$.

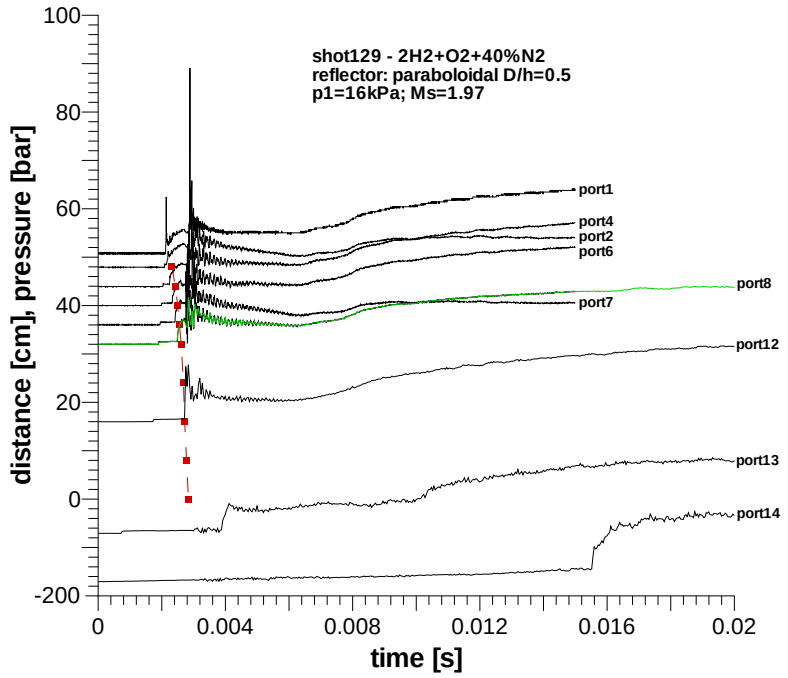

Figure 130: Deflagration-to-detonation transition DDT (shot 129); test mixture: $2H_2$+O_2+40%N_2; incident shock wave Mach number: $M_s = 1.97$.

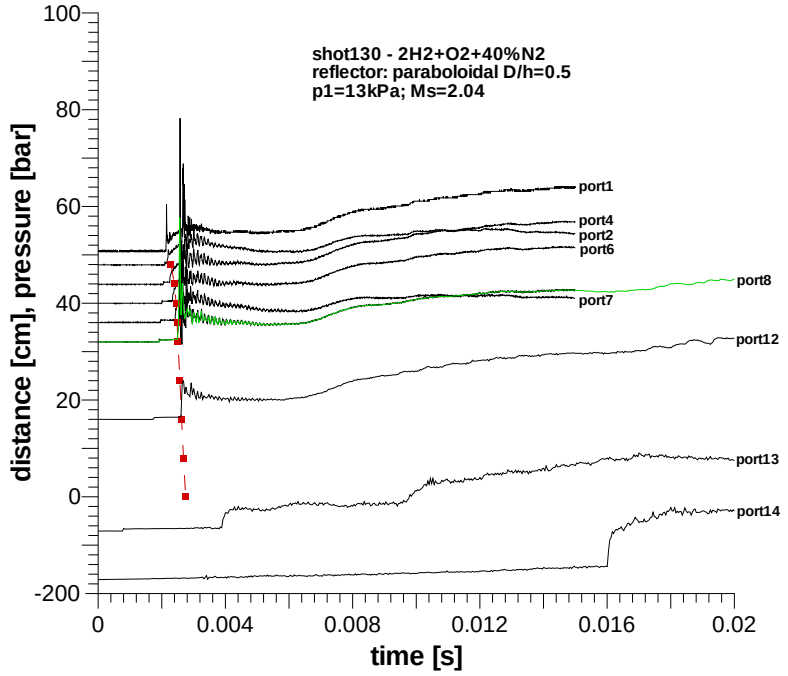

Figure 131: Deflagration-to-detonation transition DDT (shot 130); test mixture: $2H_2$+O_2+40%N_2; incident shock wave Mach number: $M_s = 2.04$.

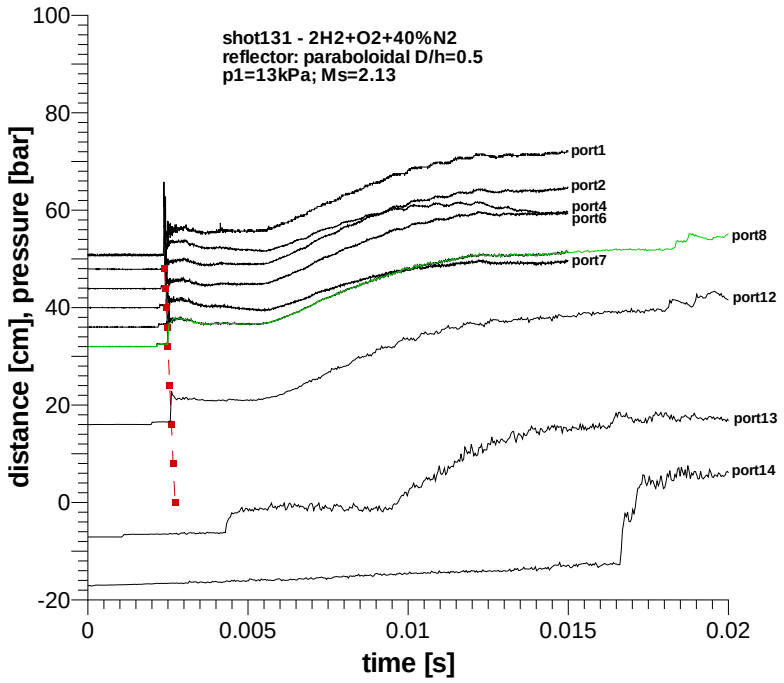

Figure 132: Detonation inside reflector (shot 131); test mixture: $2H_2+O_2+40\%N_2$; incident shock Mach number: $M_s = 2.13$.

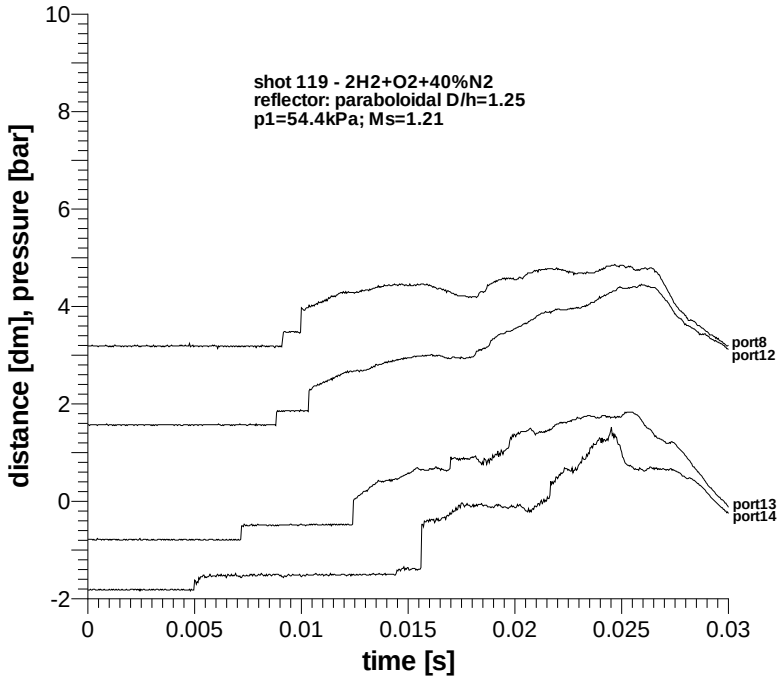

Figure 133: Deflagration outside reflector (shot 119); test mixture: $2H_2+O_2+40\%N_2$; incident shock Mach number: $M_s = 1.21$.

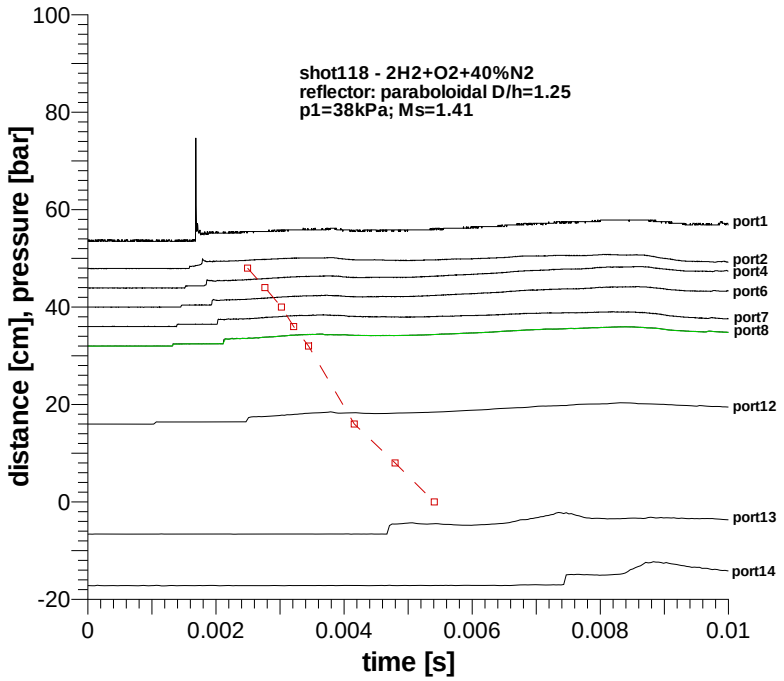

Figure 134: Deflagration outside reflector (shot 118); test mixture: $2H_2+O_2+40\%N_2$; incident shock Mach number: $M_s = 1.41$.

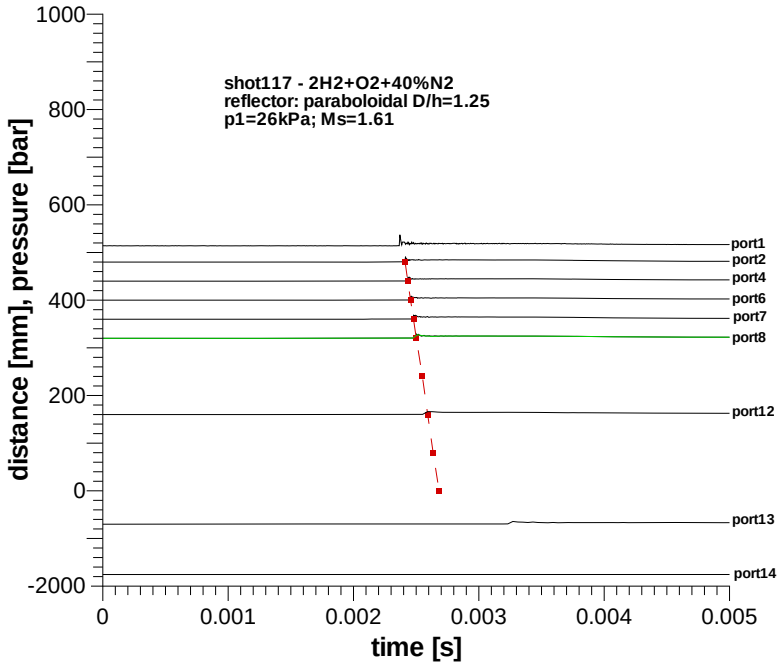

Figure 135: Detonation inside reflector (shot 117); test mixture: $2H_2+O_2+40\%N_2$; incident shock Mach number: $M_s = 2.61$.

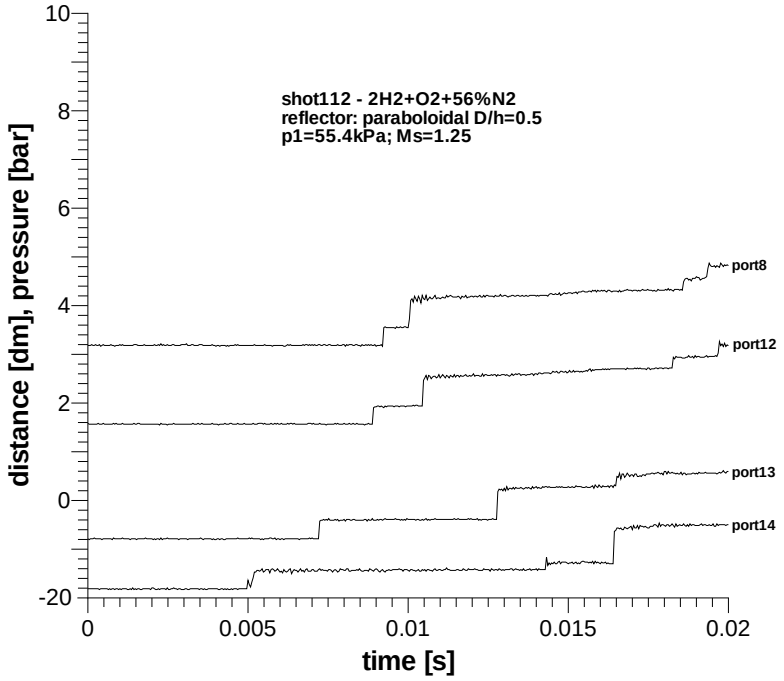

Figure 136: No combustion (shot 112); test mixture: $2H_2+O_2+56\%N_2$; incident shock Mach number: $M_s = 1.25$.

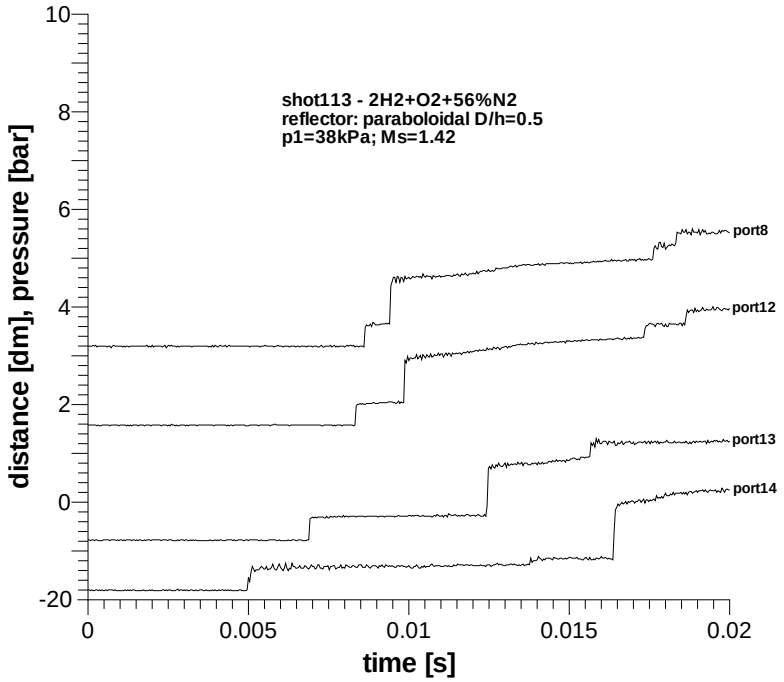

Figure 137: No combustion (shot 113); test mixture: $2H_2+O_2+56\%N_2$; incident shock Mach number: $M_s = 1.42$.

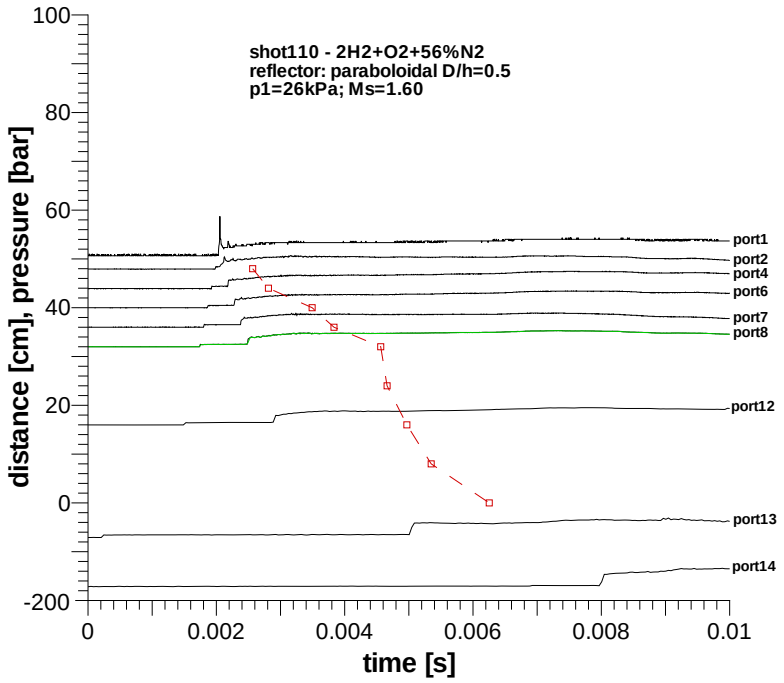

Figure 138: Deflagration outside reflector (shot 110); test mixture: $2H_2$+O_2+56%N_2; incident shock Mach number: $M_s = 1.60$.

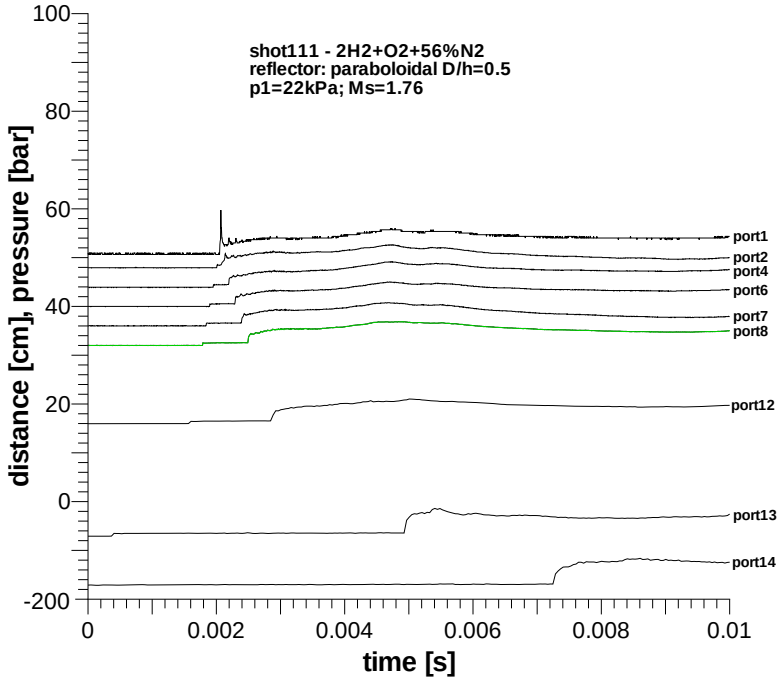

Figure 139: Deflagration outside reflector (shot 111); test mixture: $2H_2$+O_2+56%N_2; incident shock Mach number: $M_s = 1.76$.

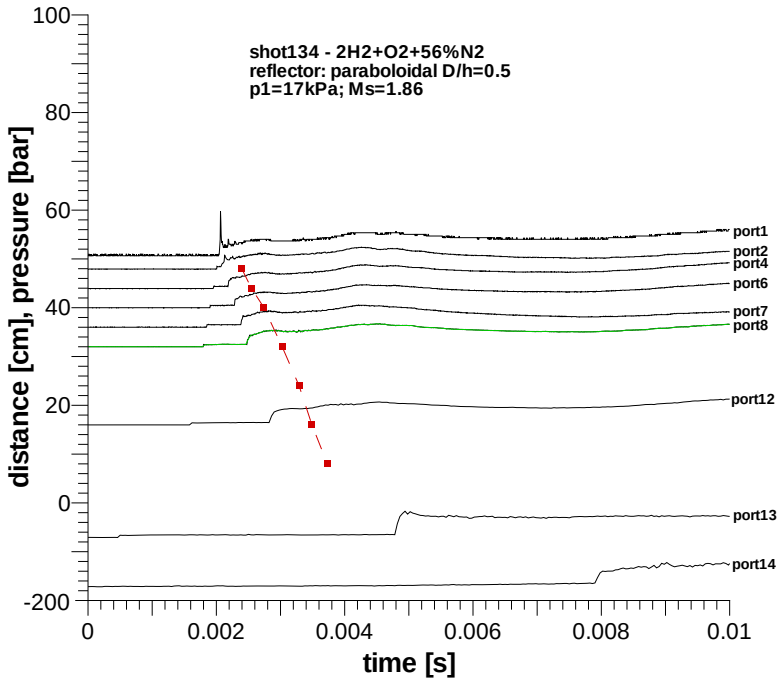

Figure 140: Deflagration outside reflector (shot 134); test mixture: $2H_2$+O_2+56%N_2; incident shock Mach number: $M_s = 1.86$.

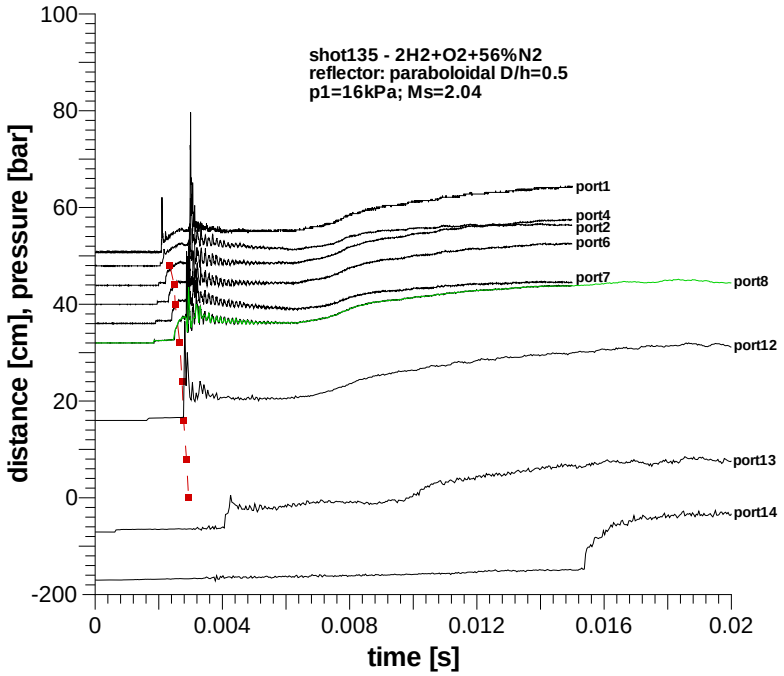

Figure 141: Deflagration-to-detonation transition DDT (shot 135); test mixture: $2H_2$+O_2+56%N_2; incident shock wave Mach number: $M_s = 2.04$.

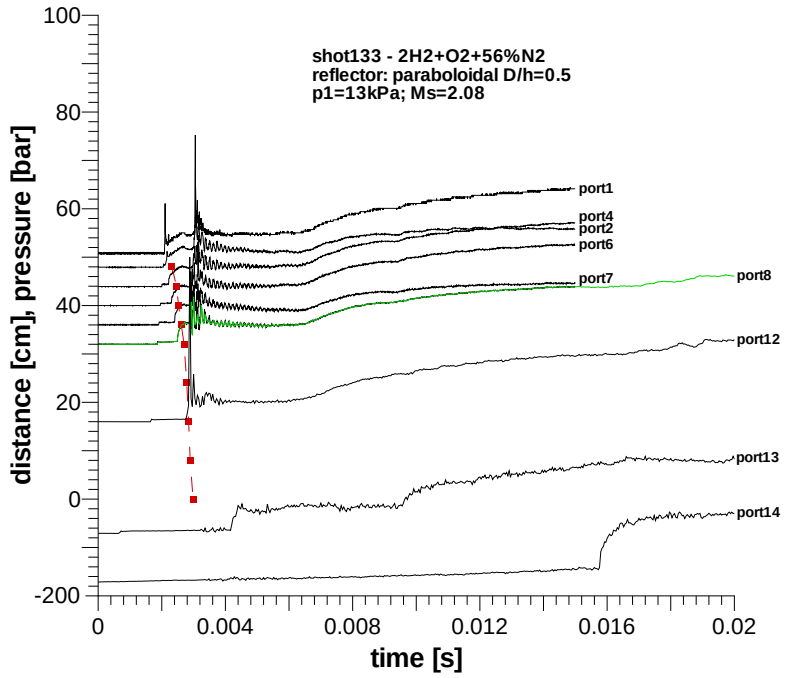

Figure 142: Deflagration-to-detonation transition DDT (shot 133); test mixture: $2H_2$+O_2+56%N_2; incident shock wave Mach number: $M_s = 2.08$.

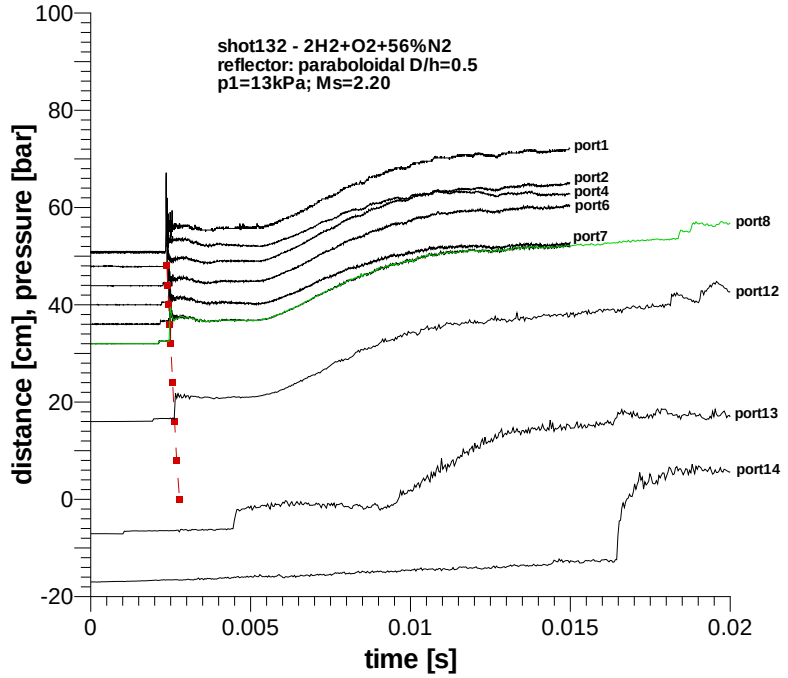

Figure 143: Detonation inside reflector (shot 132); test mixture: $2H_2$+O_2+56%N_2; incident shock Mach number: $M_s = 2.20$.

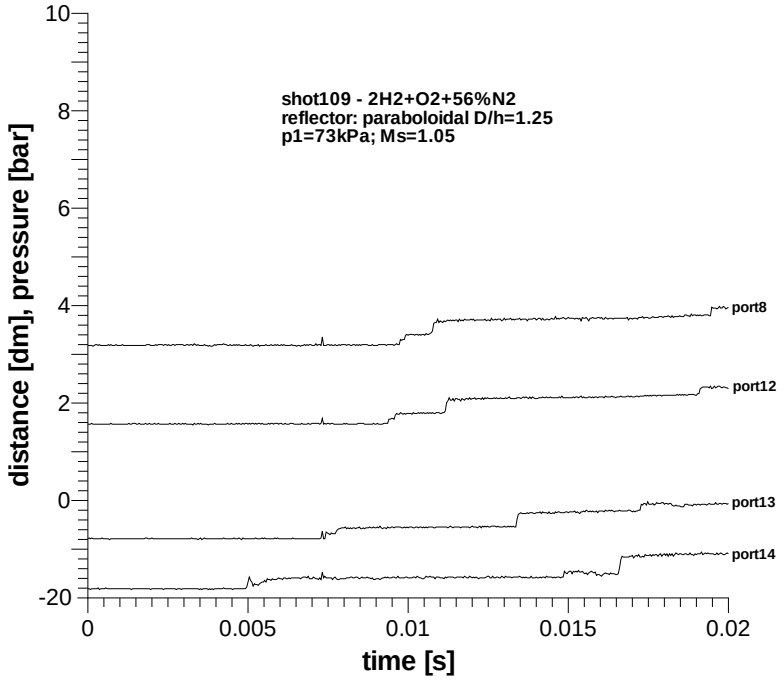

Figure 144: No combustion (shot 109); test mixture: $2H_2+O_2+56\%N_2$; incident shock Mach number: $M_s = 1.05$.

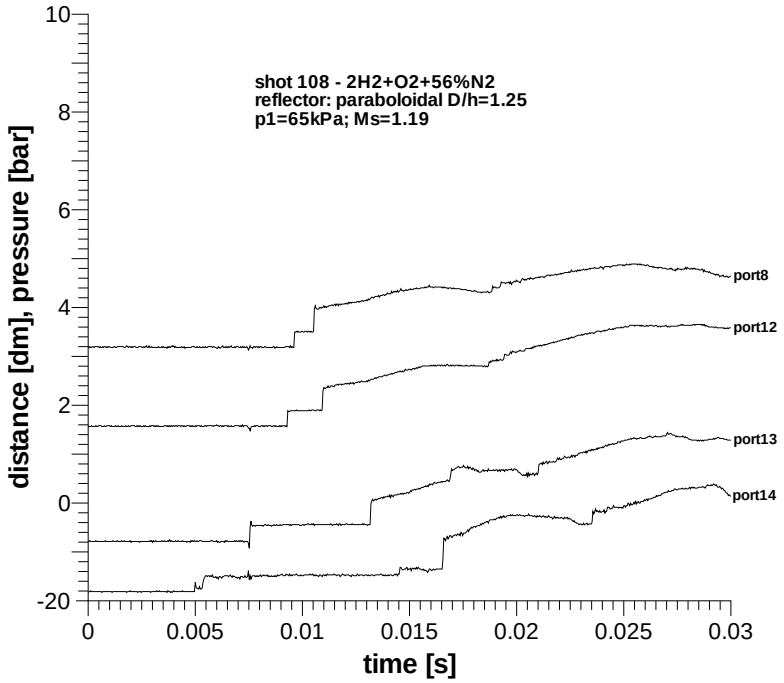

Figure 145: Deflagration outside reflector (shot 108); test mixture: $2H_2+O_2+56\%N_2$; incident shock Mach number: $M_s = 1.19$.

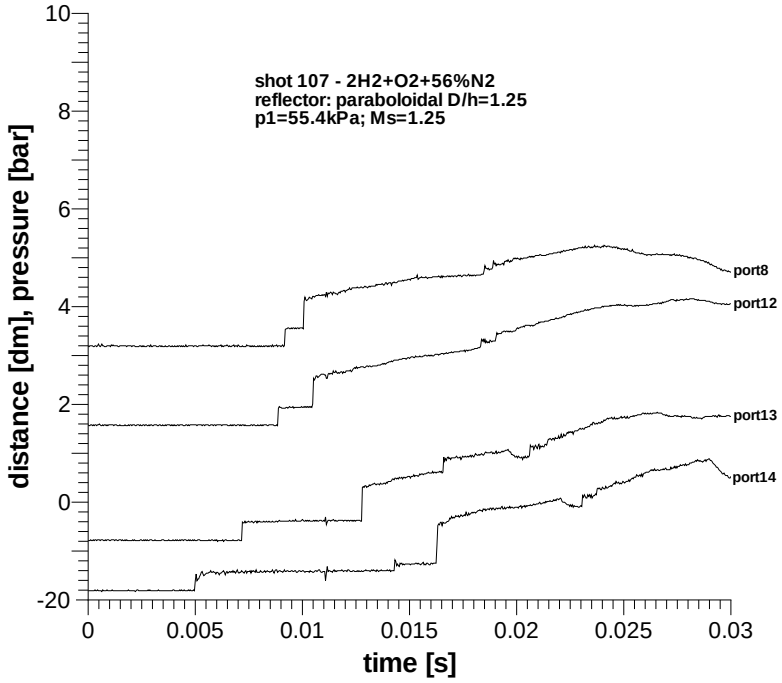

Figure 146: Deflagration outside reflector (shot 107); test mixture: $2H_2$+O_2+56%N_2; incident shock Mach number: $M_s = 1.25$.

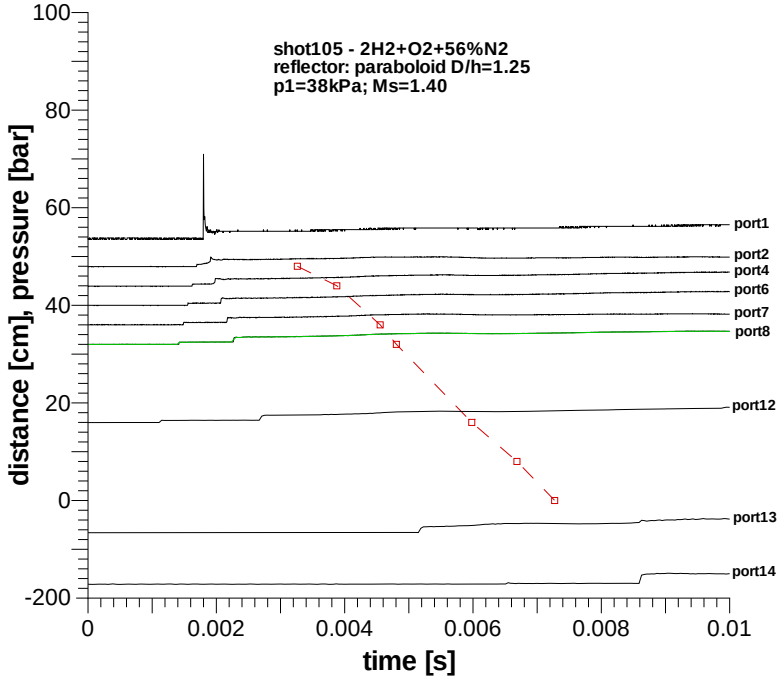

Figure 147: Deflagration outside reflector (shot 105); test mixture: $2H_2$+O_2+56%N_2; incident shock Mach number: $M_s = 1.40$.

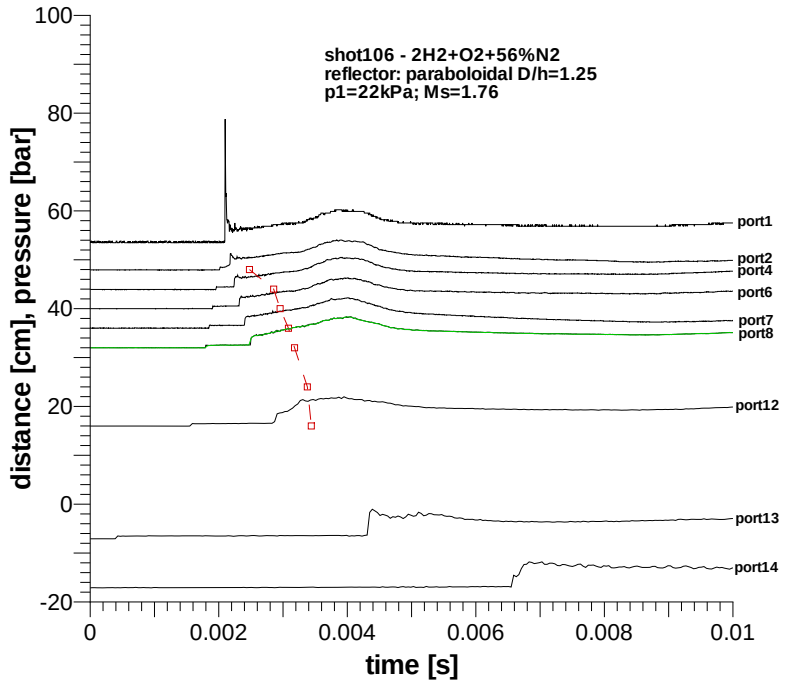

Figure 148: Deflagration outside reflector (shot 106); test mixture: $2H_2+O_2+56\%N_2$; incident shock Mach number: $M_s = 1.76$.

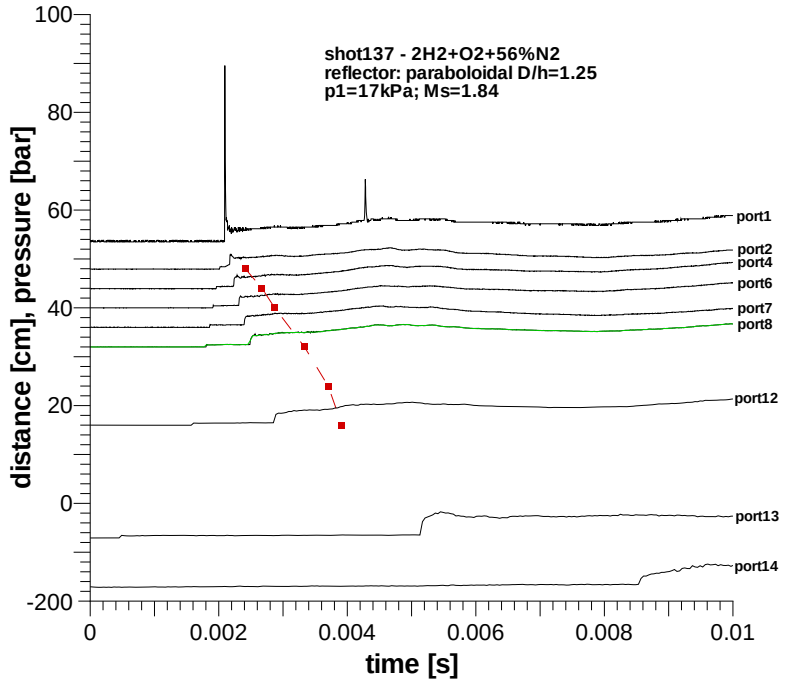

Figure 149: Deflagration outside reflector (shot 137); test mixture: $2H_2+O_2+56\%N_2$; incident shock Mach number: $M_s = 1.84$.

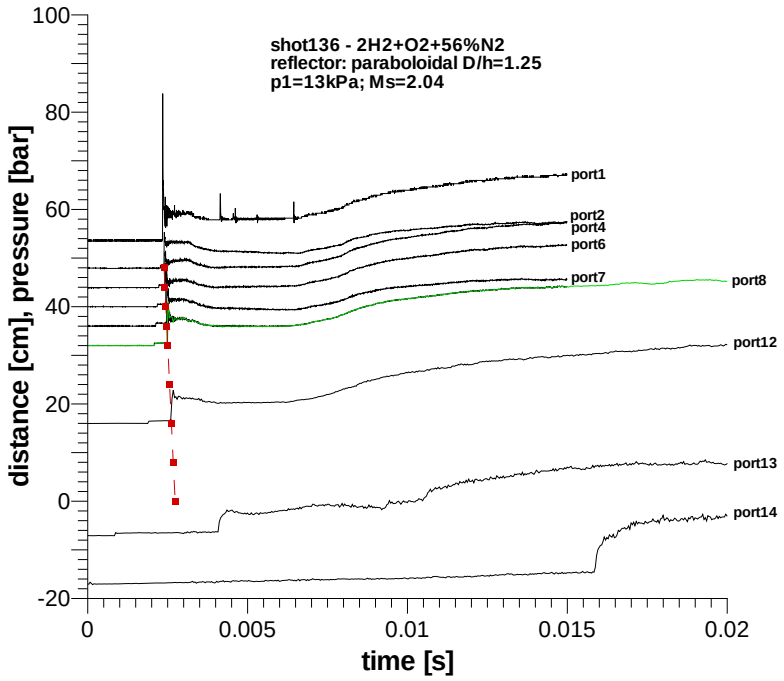

Figure 150: Detonation inside reflector (shot 136); test mixture: $2H_2+O_2+56\%N_2$; incident shock Mach number: $M_s = 2.04$.

E CAD Drawings

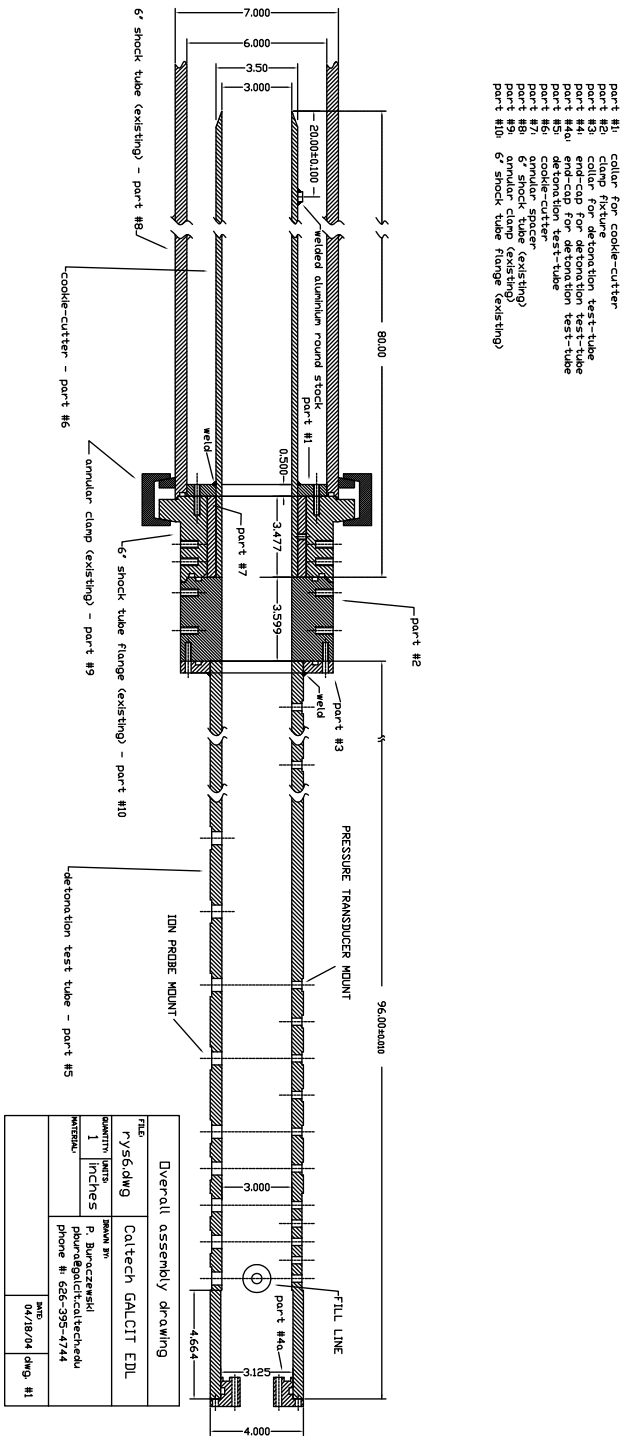

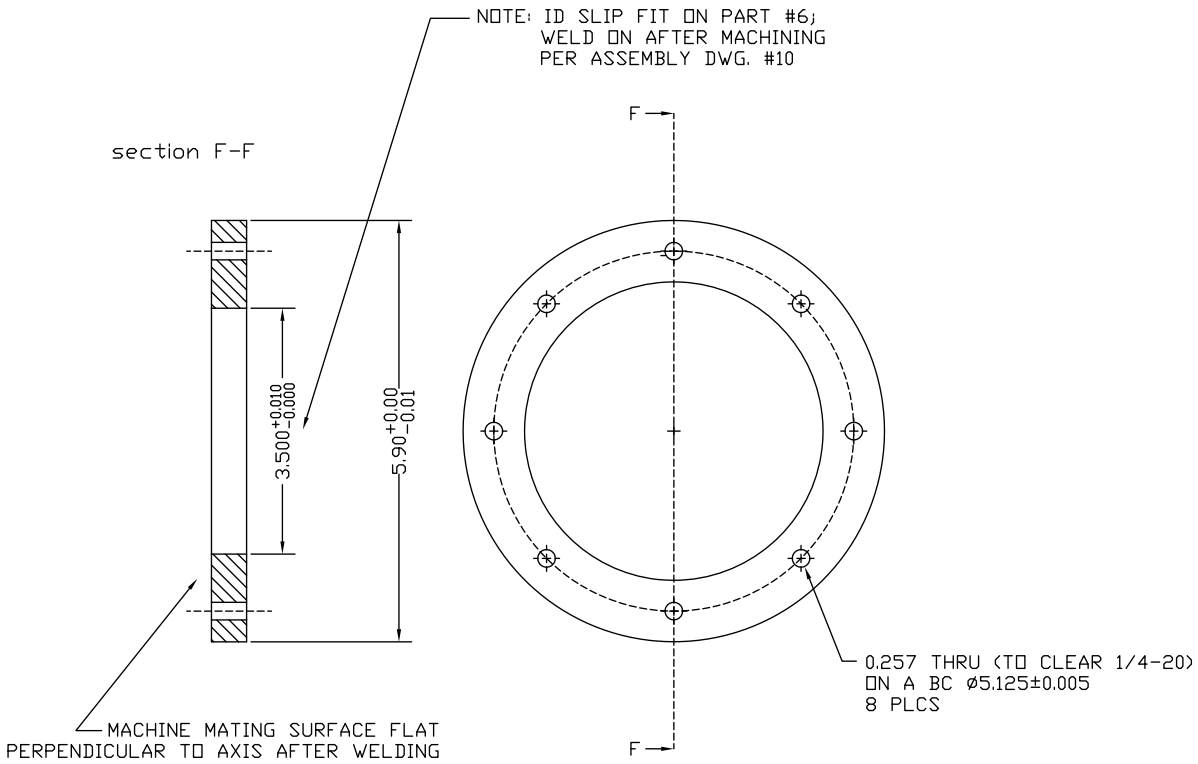

Collar for cookie-cutter - part #1			
FILE: rys6.dwg	Caltech GALCIT EDL		
QUANTITY: 1 / UNITS: inches	DRAWN BY: P. Buraczewski pbura@galcit.caltech.edu phone #: 626-395-4744		
MATERIAL: Al 6061			
NOTE: break sharp corners max. 1/64		DATE: 04/18/04	dwg. #2

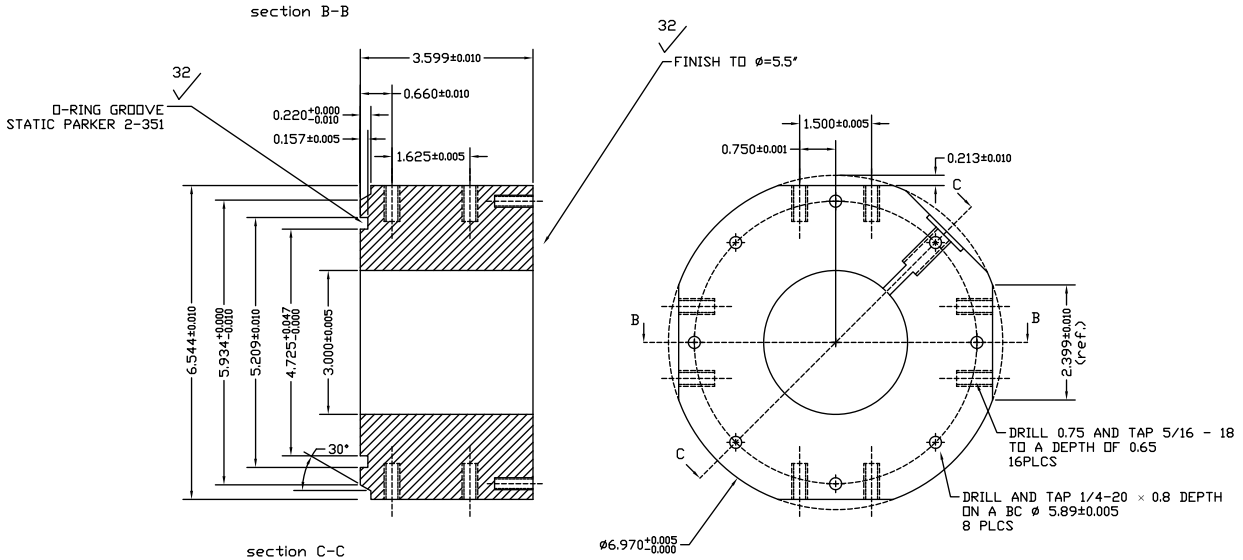

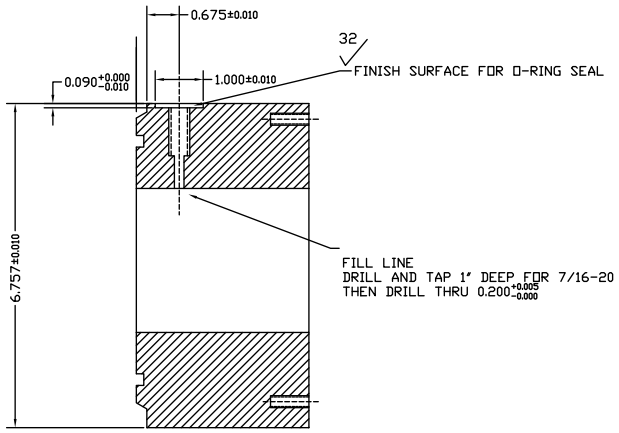

Clamp fixture - part #2		
FILE: rys6.dwg	Caltech GALCIT EDL	
QUANTITY: 1 / UNITS: inches	DRAWN BY: P. Buraczewski pbura@galcit.caltech.edu phone #: 626-395-4744	
MATERIAL: Al 6061		
NOTE: break sharp corners max. 1/64	DATE: 04/18/04	dwg. #3

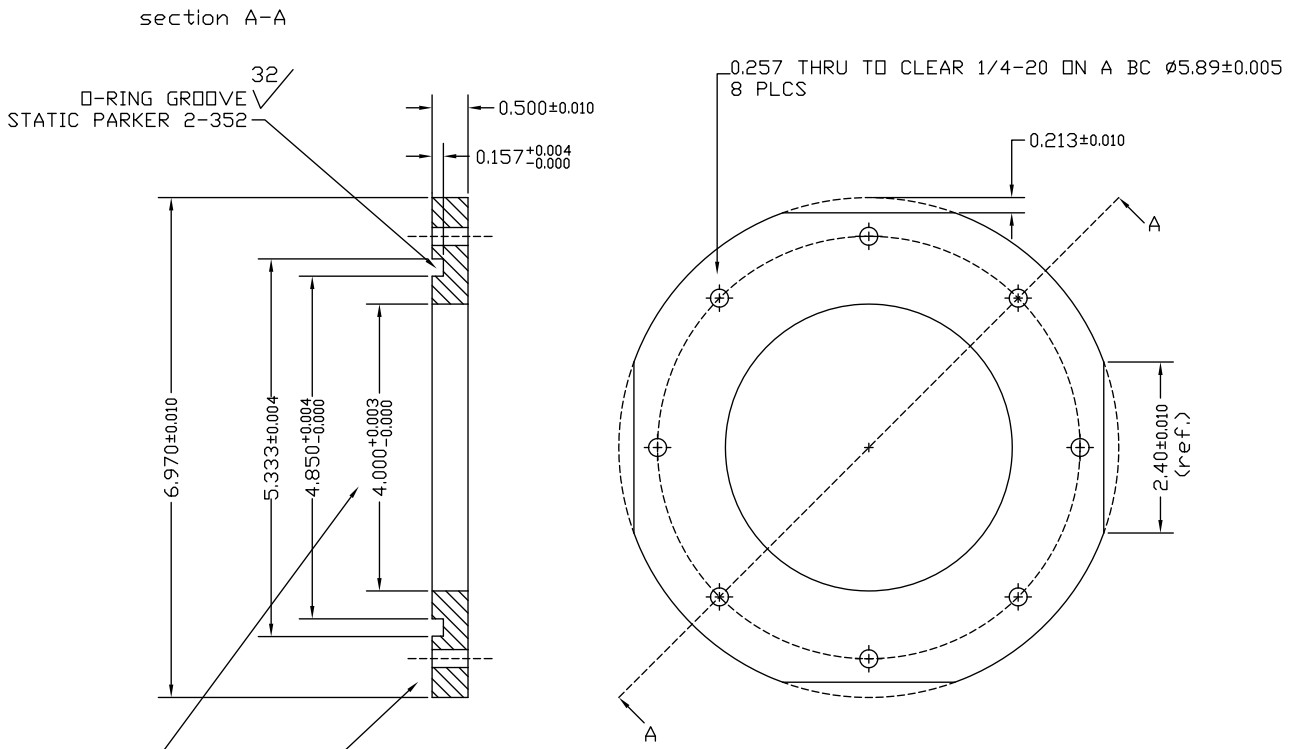

Collar for det. test tube - part #3			
FILE: rys6.dwg	Caltech GALCIT EDL		
QUANTITY: 1	UNITS: inches	DRAWN BY: P. Buraczewski pbura@galcit.caltech.edu phone #: 626-395-4744	
MATERIAL: Al 6061			
NOTE: break sharp corners max. 1/64		DATE: 04/18/04	dwg. #4

section C-C

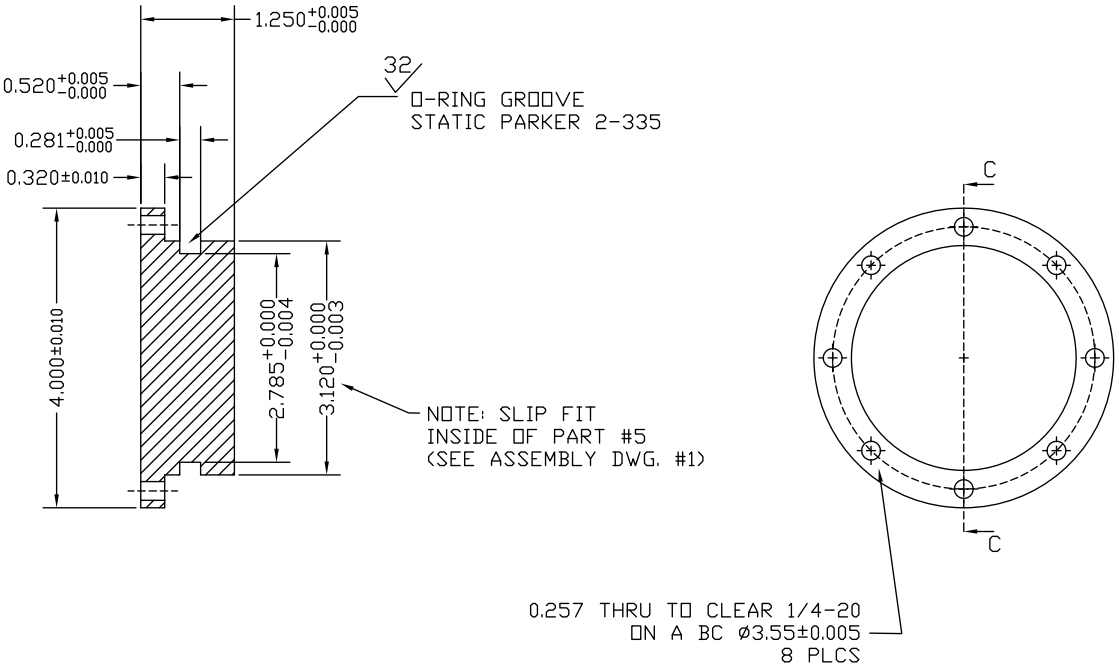

End Cap for det. test tube - part #4			
FILE: rys6.dwg		Caltech GALCIT EDL	
QUANTITY: 1	UNITS: inches	DRAWN BY: P. Buraczewski pbura@galcit.caltech.edu phone #: 626-395-4744	
MATERIAL: Al 6061			
NOTE: break sharp corners max. 1/64		DATE: 04/18/04	dwg. #5

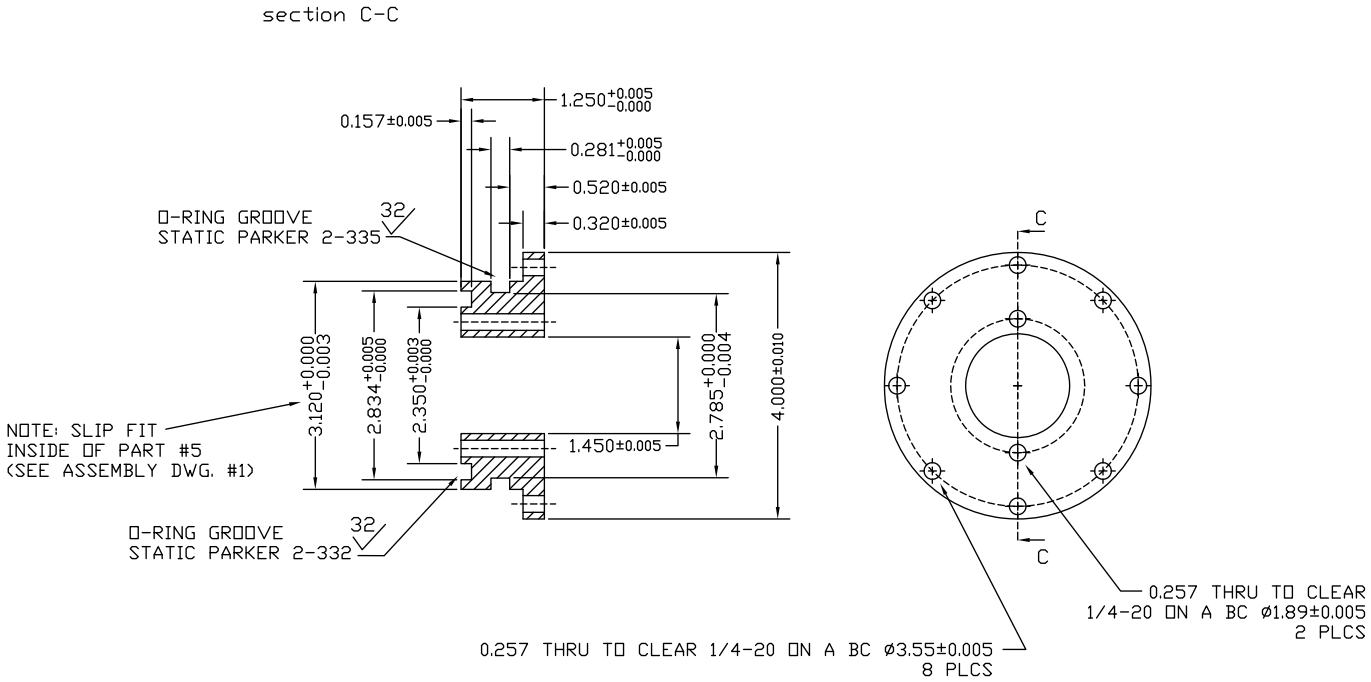

End Cap for det. test tube - part #4a		
FILE: rys6.dwg	Caltech GALCIT EDL	
QUANTITY: 1 / UNITS: inches	DRAWN BY: P. Buraczewski pbura@galcit.caltech.edu phone #: 626-395-4744	
MATERIAL: Al 6061		
NOTE: break sharp corners max. 1/64	DATE: 04/18/04	dwg. #6

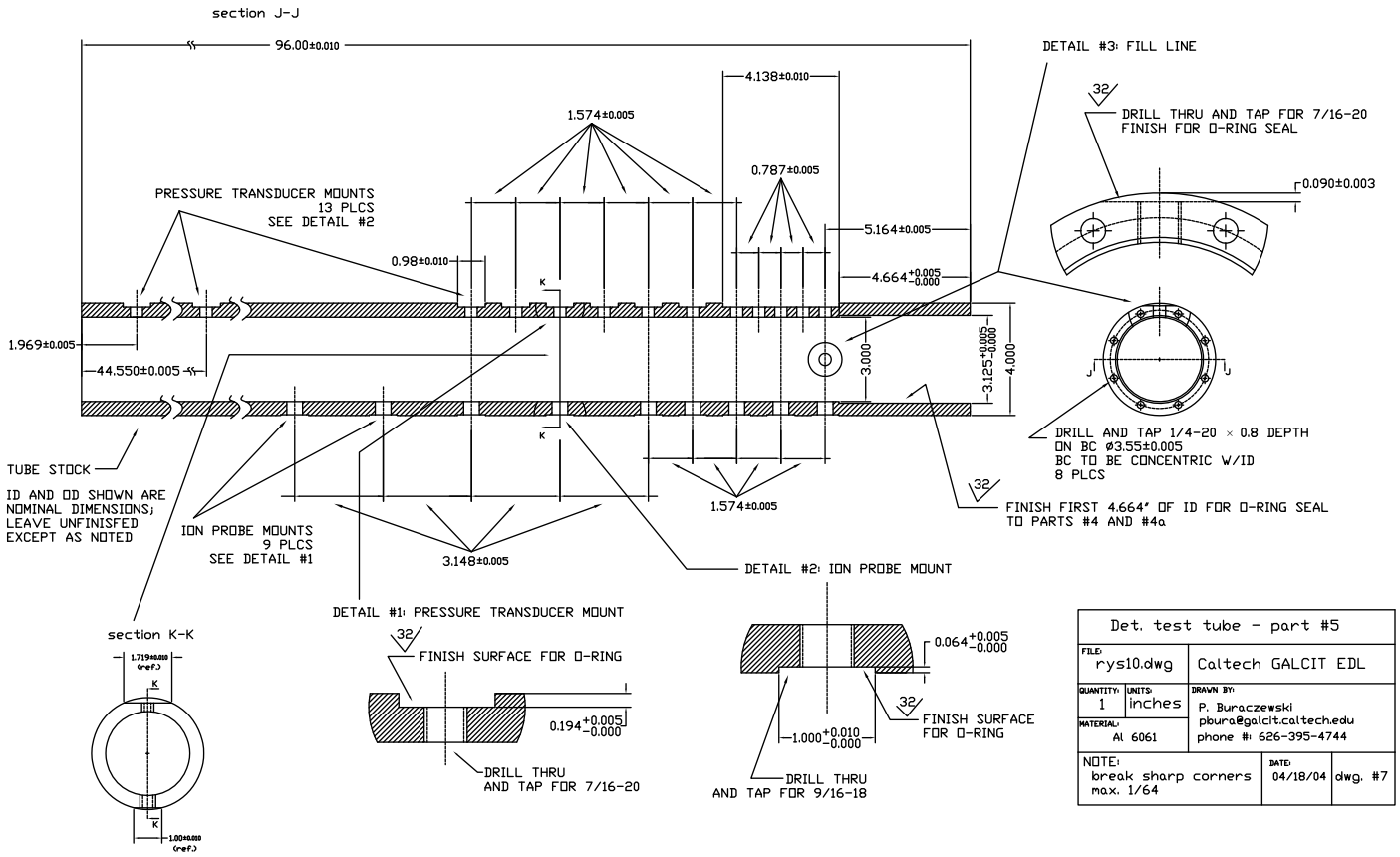

Det. test tube - part #5			
FILE: rys10.dwg	Caltech GALCIT EDL		
QUANTITY: 1	UNITS: inches	DRAWN BY: P. Buraczewski pbura@galcit.caltech.edu phone #: 626-395-4744	
MATERIAL: Al 6061			
NOTE: break sharp corners max. 1/64		DATE: 04/18/04	dwg. #7

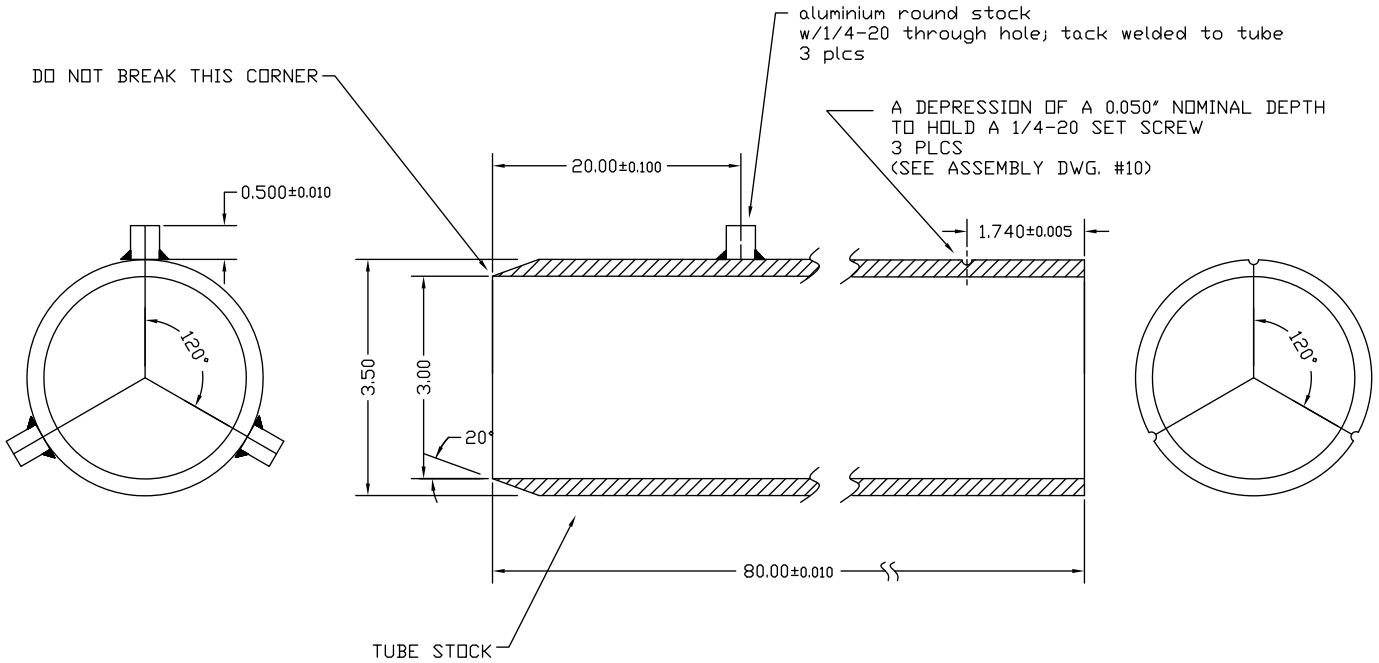

Cookie-cutter - part #6		
FILE: rys6.dwg	Caltech GALCIT EDL	
QUANTITY: 1 / UNITS: inches	DRAWN BY: P. Buraczewski pbura@galcit.caltech.edu ext.: 626-395-4744	
MATERIAL: Al 6061		
NOTE: unless noted, break sharp corners max. 1/64	DATE: 04/18/04	dwg. #8

section H-H

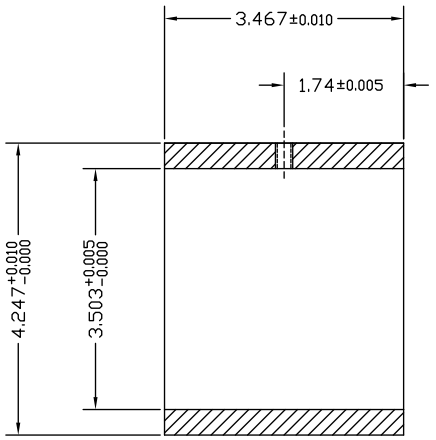

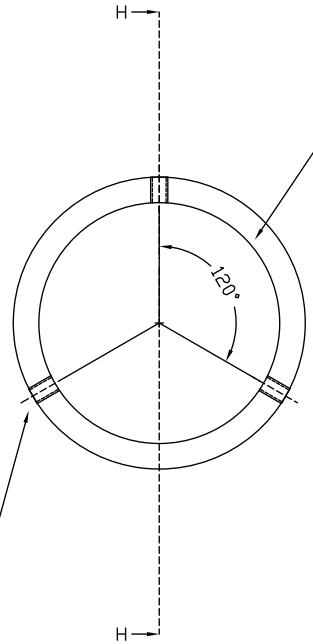

NOTE: SLIP FIT ON PART #6
HELD TO PART #6
BY 1/4-20 SET SCREWS
(SEE ASSEMBLY DWG. #10)

DRILLED THRU AND TAPPED FOR 1/4-20
3 PLCS

Annular spacer - part #7			
FILE: rys6.dwg		Caltech GALCIT EDL	
QUANTITY: 1	UNITS: inches	DRAWN BY: P. Buraczewski pbura@galcit.caltech.edu phone #: 626-395-4744	
MATERIAL: Al 6061			
NOTE: break sharp corners max. 1/64		DATE: 04/18/04	dwg. #9

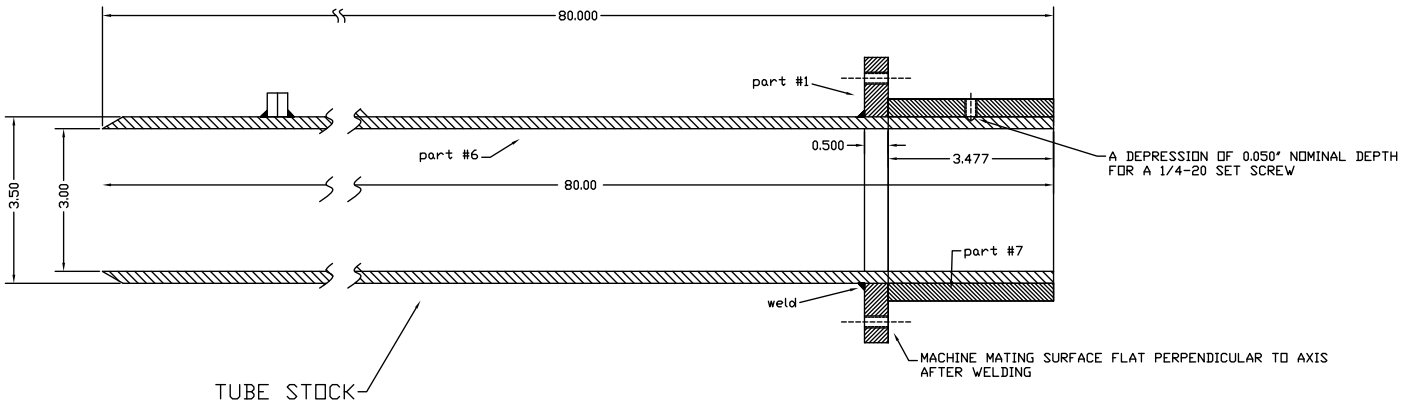

Assembly drawing for cookie-cutter			
FILE: rys6.dwg	Caltech GALCIT EDL		
QUANTITY: 1	UNITS: inches	DRAWN BY: P. Buraczewski pbura@galcit.caltech.edu phone #: 626-395-4744	
MATERIAL:			
NOTE: break sharp corners max. 1/64		DATE: 04/18/04	dwg. #10

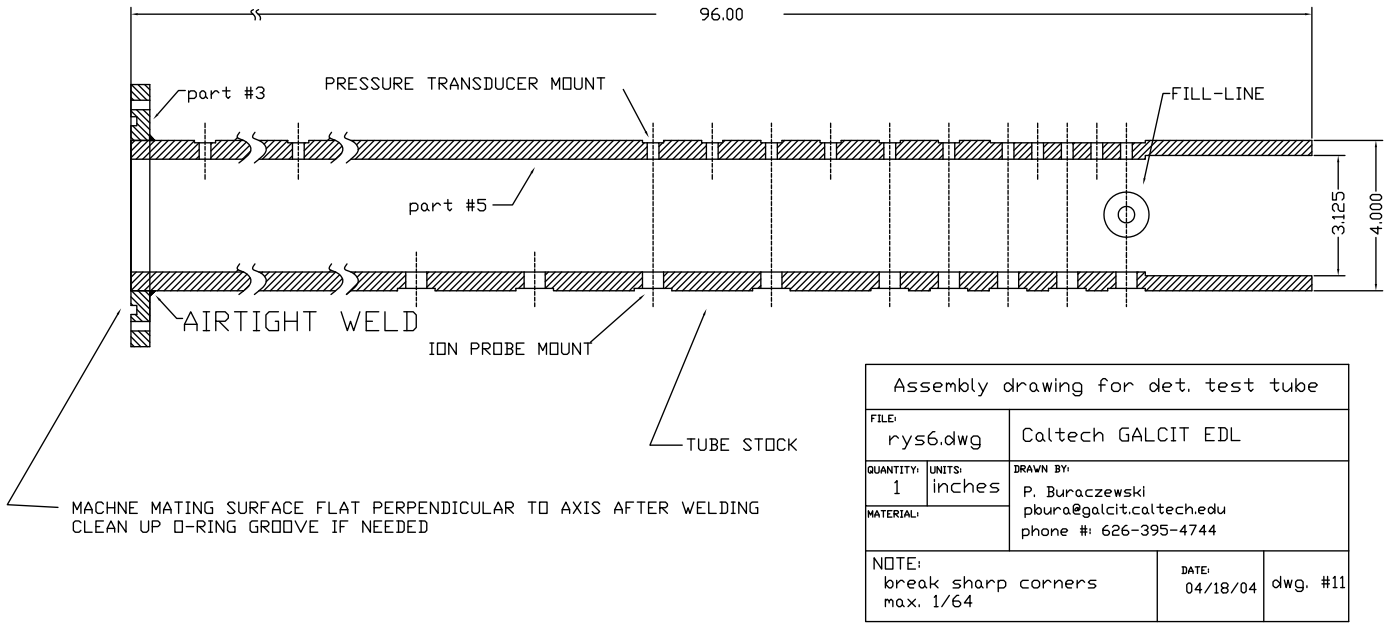

Assembly drawing for det. test tube			
FILE: rys6.dwg		Caltech GALCIT EDL	
QUANTITY: 1	UNITS: inches	DRAWN BY: P. Buraczewski pbura@galcit.caltech.edu phone #: 626-395-4744	
MATERIAL:			
NOTE: break sharp corners max. 1/64		DATE: 04/18/04	dwg. #11

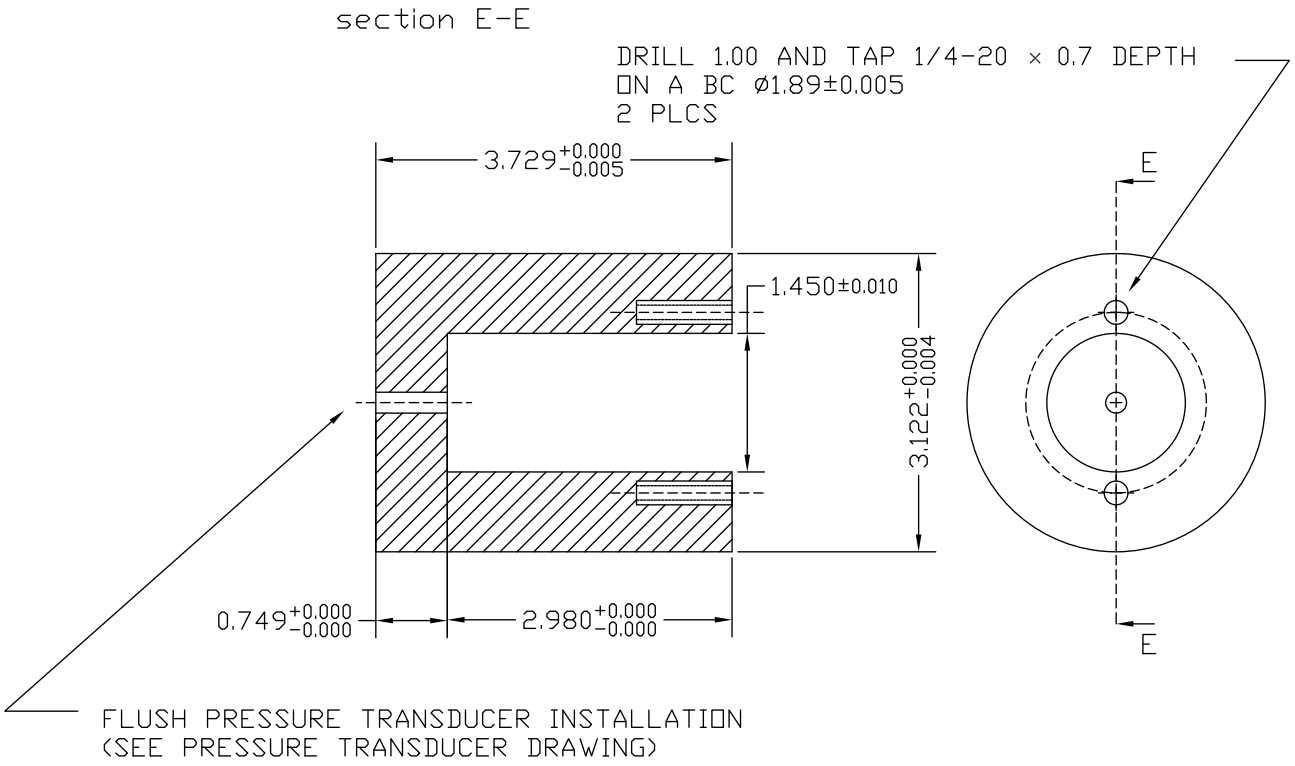

Flat 'Reflector'	
FILE: rys11.dwg	Caltech GALCIT EDL
QUANTITY: 1 / UNITS: inches	DRAWN BY: P. Buraczewski pbura@galcit.caltech.edu ext.: 4744
MATERIAL: Al 6061	
DATE: 8/06/04	

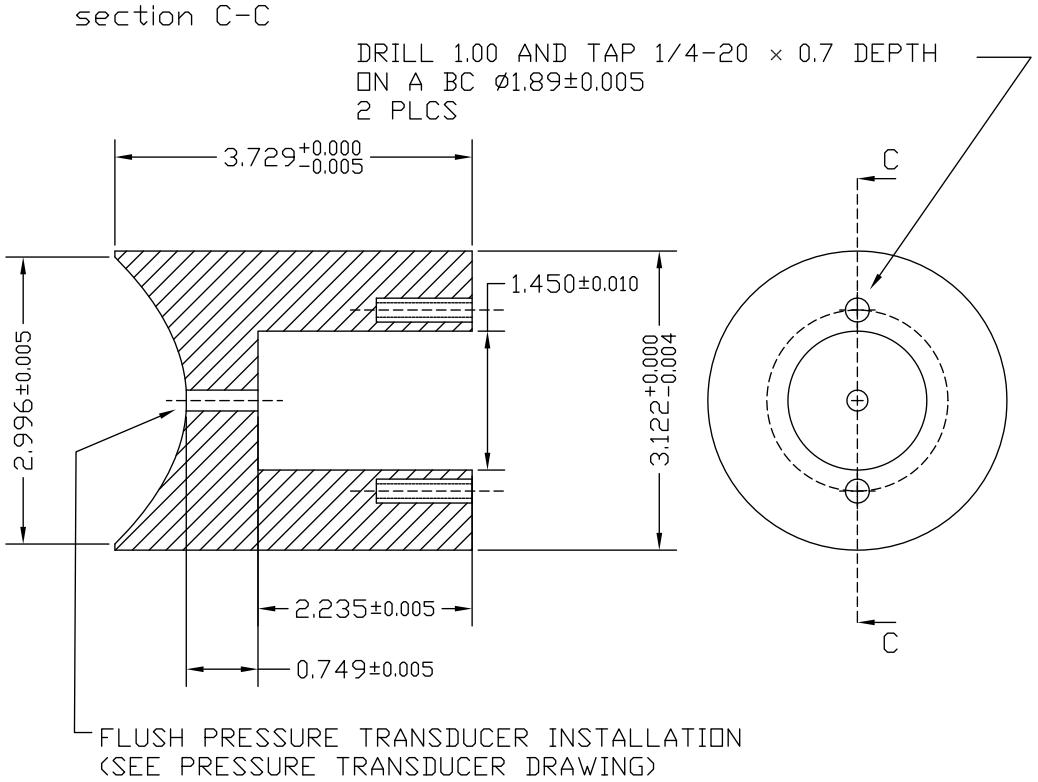

Paraboloid Reflector #3	
FILE: rys11.dwg	Caltech GALCIT EDL
QUANTITY: 1 / UNITS: inches	DRAWN BY: P. Buraczewski pbura@galcit.caltech.edu ext.: 4744
MATERIAL: Al 6061	
DATE: 07/07/04	

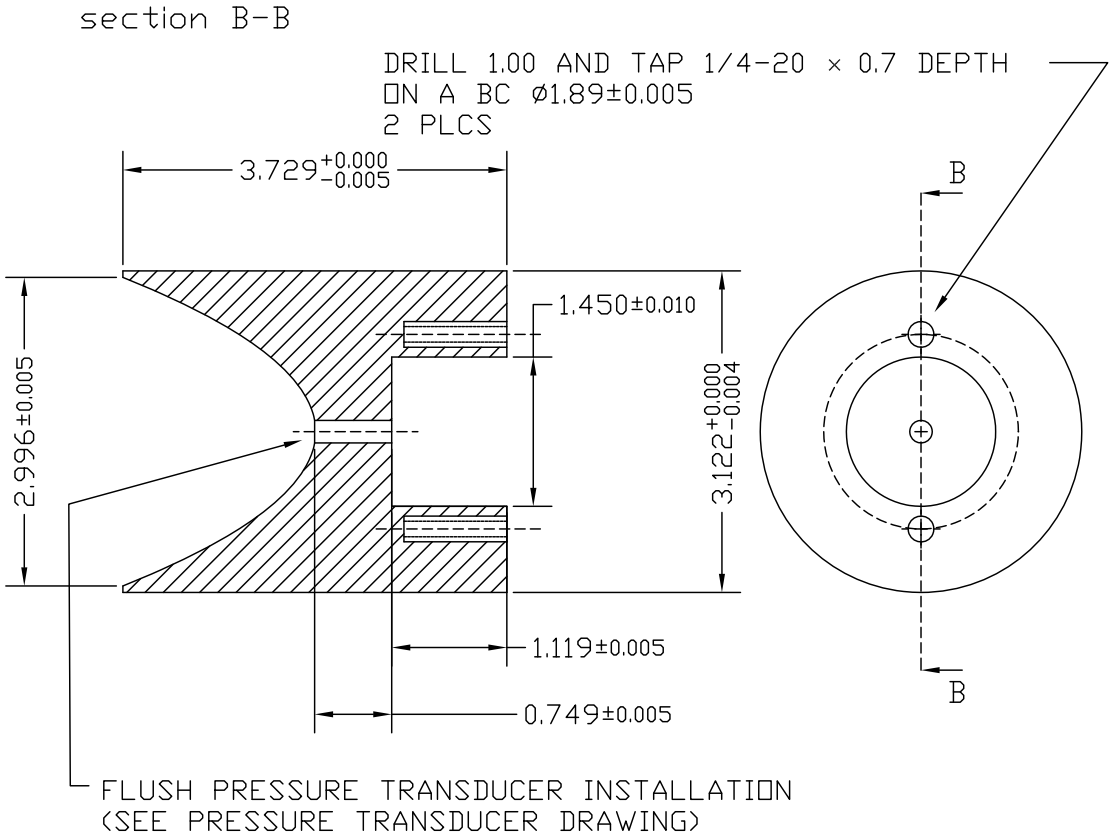

Paraboloid Reflector #2		
FILE: rys11.dwg		Caltech GALCIT EDL
QUANTITY: 1	UNITS: inches	DRAWN BY: P. Buraczewski pbura@galcit.caltech.edu ext.: 4744
MATERIAL: Al 6061		
DATE: 07/07/04		

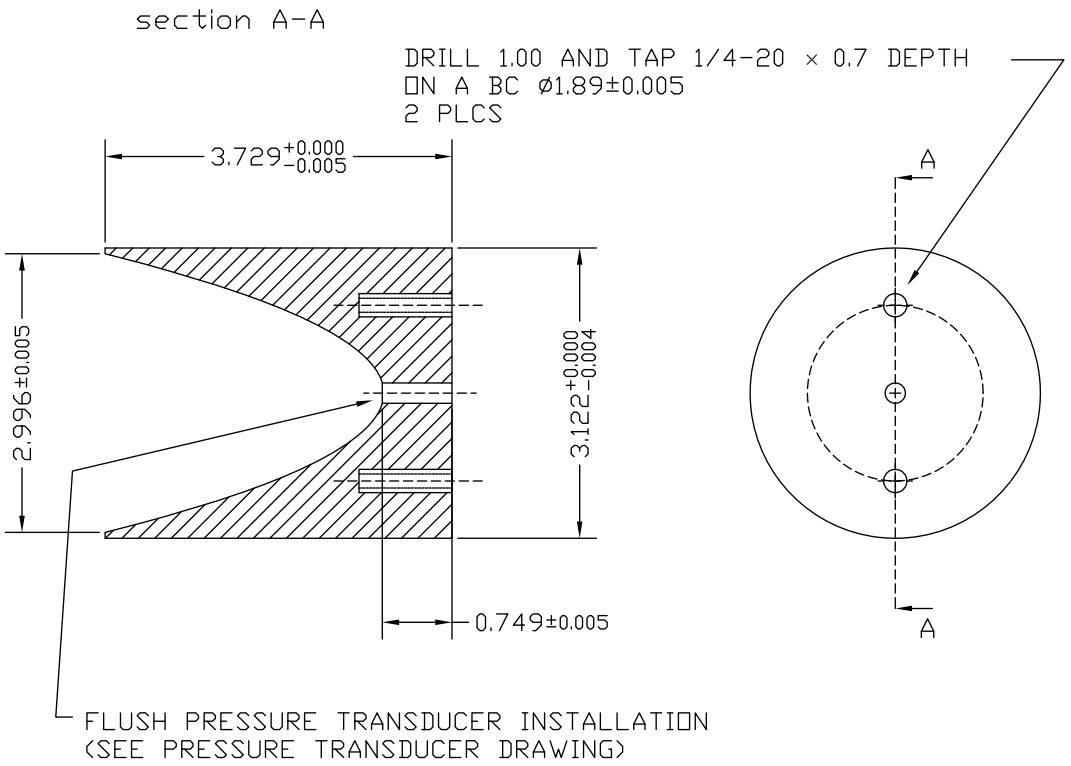

Paraboloid Reflector #1	
FILE: rys11.dwg	Caltech GALCIT EDL
QUANTITY: 1 / UNITS: inches	DRAWN BY: P. Buraczewski pbura@galcit.caltech.edu ext.: 4744
MATERIAL: Al 6061	
DATE: 07/07/04	

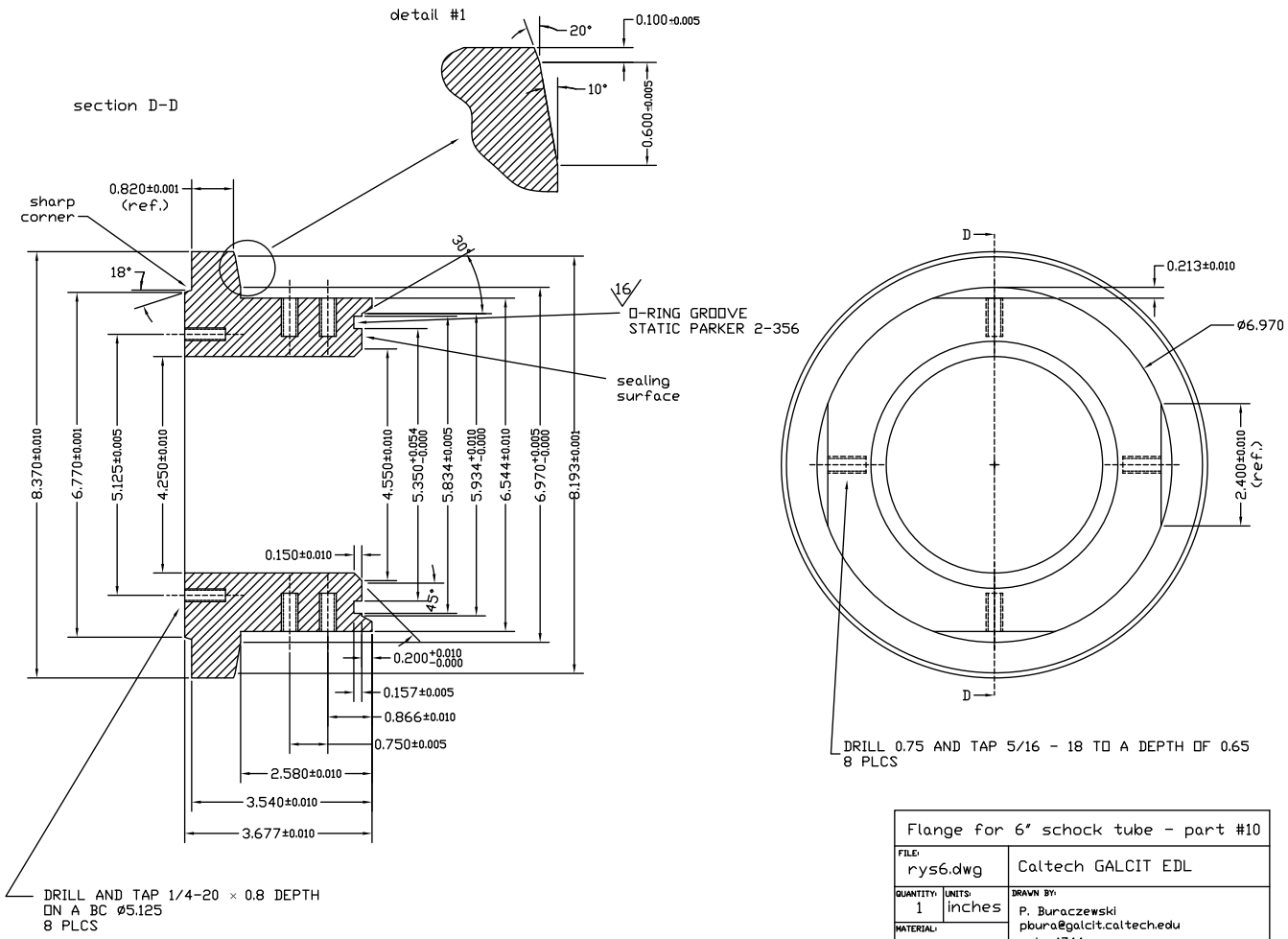

Flange for 6" schock tube - part #10	
FILE: rys6.dwg	Caltech GALCIT EDL
QUANTITY: 1 / UNITS: inches	DRAWN BY: P. Buraczewski pbura@galcit.caltech.edu ext.: 4744
MATERIAL: Al 6061	
DATE: 12/10/03	